# Chapter 7

# Non-reactive Simulations of the ev7is

## 7.1 Burner Description

This section describes the ev7is burner and the underlying concept. This description is also valid for the reactive LES of the next chapter.

### 7.1.1 Swirl Flow

Virtually all combustion devices make sure that the flame is anchored at a specific location. The simplest way of stabilising a flame is behind a sudden expansion like a backward-facing step. The flow is strongly decelerated and forms a corner recirculation zone (CRZ). The recirculating hot gases provide the ignition of the incoming fresh gases.
A much more compact flame stabilisation is obtained by a highly swirling flow which passes through a sudden expansion. It generally forms a central toroidal recirculation zone (CTRZ) which acts as a flame-holder in the centre of the flow. The flow pattern of such a flow is illustrated by Figure (7.1).

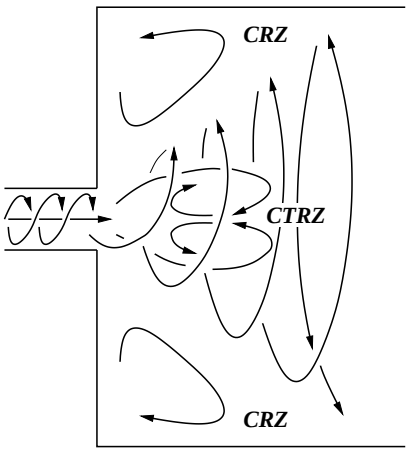


Figure 7.1: Schematic illustration of the flow pattern of a highly swirled flow.

Why such a flow forms a CTRZ is explained by the Euler equations or also a simple balance of the involved forces on an infinitesimal fluid element [34]: the centrifugal force

must be balanced by the pressure force. Therefore the radial pressure gradient is:

$$\frac{\partial p}{\partial r_a} = \frac{\rho u_\varphi^2}{r_a} \tag{7.1}$$

where $r_a$ is the distance from the flow axis and $u_\varphi$ the circumferential velocity component. Knowing the distribution of the circumferential velocity, the pressure field is easily determined from Equation (7.1). Thus, a swirling flow always exhibits lower pressure levels in its centre than far from the axis. Discharging such a swirling flow into a chamber reduces the circumferential velocity (through conservation of momentum) and therefore a negative axial pressure gradient is created. If this axial pressure gradient is strong enough it will cause flow recirculation and the CTRZ is formed. This process is a special case of "Vortex Breakdown" (VB), which is a general term for the auto-destruction of a vortex. It either breaks down completely into turbulence or forms a different vortical structure. Therefore the CTRZ is a source of intense turbulence and/or coherent structures such as the "Precessing Vortex Core" (PVC) [7, 56].
Apart from the formation of a CTRZ used for flame stabilisation, swirling flows are also popular for the intense mixing they cause. This is simply due to the strong velocity gradients encountered in this type of flow.

### 7.1.2 Concept of Lean Partially Premixed Combustion

Modern gas turbines have to meet very strict standards in $NO_X$-emission levels. Lean partially premixed combustion is one of the ways to meet these standards. The burner used for this work was designed to operate in this regime for a wide range of operating conditions.
Lean partially premixed combustion is a compromise between secure flame stabilisation and good mixing:

- A perfectly premixed gas produces the lowest possible $NO_X$-emissions (for the given equivalence ratio) but the flame might propagate upstream (flashback) and thereby destroy the burner.

- Non-premixed combustion is always burning locally at stoichiometry and therefore producing very high $NO_X$-emission levels. However, the flame is not able to propagate upstream of the fuel injection, avoiding flashback problems.

A lean partially premixed burner injects the fuel as close as possible to the combustion region but makes also sure that the fuel does not burn until sufficient mixing is achieved. This is realised by injecting the fuel in a flow with moves too fast

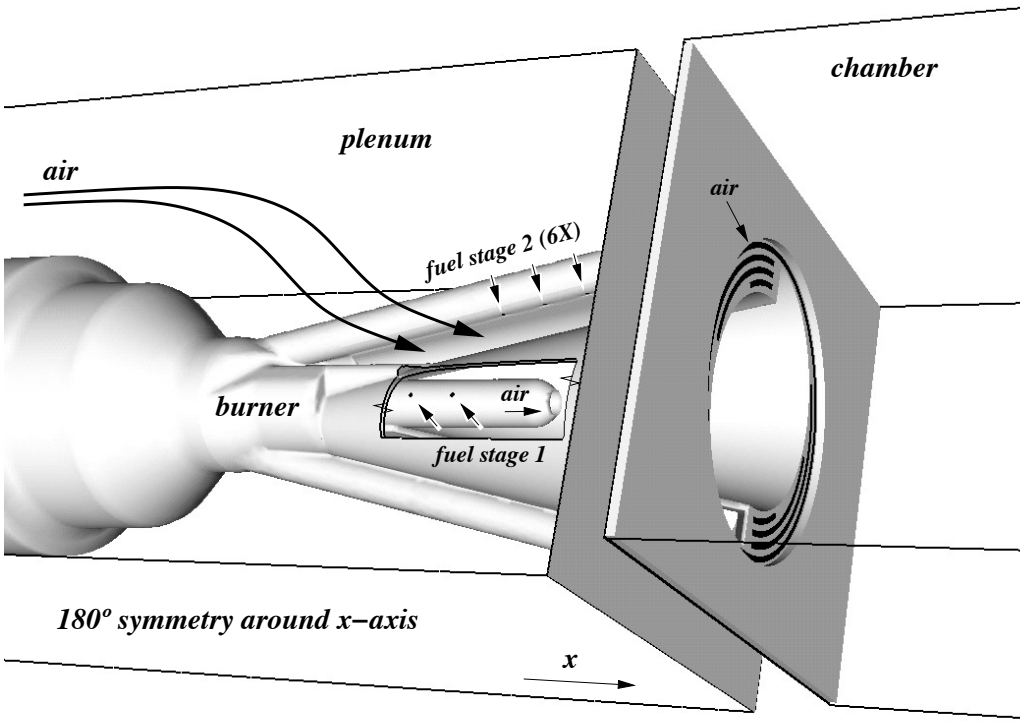


Figure 7.2: Schematic illustration of the ev7is burner.

to allow flame stabilisation in the vicinity of the injections. The strong swirling motion and its VB ensure rapid mixing. Finally, the CTRZ will stabilise the flame near the burner exit.

### 7.1.3 The ev7is Burner

The burner considered in this study is an industrial gas turbine burner. It was designed for the EU-project FuelChief and is based on Alstom's environmental (ev) burner. It was necessary to down-scale the original burner in order to fit it into the medium-pressure test rig of the Institute of Combustion Technology at DLR Stuttgart. Also, this makes the numerical simulations computationally less demanding. Additionally to the combustion experiments at DLR, Alstom Power conducted water-lab experiments in order to evaluate mixing and flow field for the non-reactive cases. These results will be used to validate the non-reactive simulations in this chapter.
An illustration of the burner concept is seen in Figure (7.2). The burner consists of two half-cones that are shifted in respect to each other, which gives the burner

a 180$^o$ symmetry around the $x$-axis. The main part of the air enters the double-cone at the so created slots and exits through the bottom of the double-cone which opens into the combustion chamber (on the right). Fuel is injected at the slots (called stage 2) and at the side of a lance inserted from the left into the cone (called stage 1). Additionally, a small quantity of air flows through the tip of this lance (called the shielding air). The repartition of fuel between stage 1 and 2 can be adjusted. This allows for the modification of the combustion process without changing the global equivalence ratio. Note that in Figure (7.2), only 3 holes of stage 2 are visible. There are six on each side, which makes 12 in total. Stage 1 has two holes on each side (4 in total).
The repartition of the fuel into stage 1 and stage 2 allows for the modification of the spatial distribution of fuel. The staging ratio is defined as:

$$\alpha_{st} = \frac{\dot{m}_{st1}}{\dot{m}_{st1} + \dot{m}_{st2}} \tag{7.2}$$

where $\dot{m}_{st1}$ and $\dot{m}_{st2}$ are the fuel mass fluxes injected through stage 1 and stage 2. The variation of $\alpha_{st}$ has an influence on pollutant emission and thermo-acoustic stability. This is a main design feature of this burner.
In order to protect the burner from hot combustion products, cooling air is entering the chamber at the burner exit. This is represented in Figure (7.2) by the black lines at the burner front which correspond in reality to a multitude of small holes that are connecting the plenum with the chamber.

## 7.2 LES and Experimental Setup

Table (7.1) summarises all available simulations and experiments. Their particularities will be described in the following.

### 7.2.1 LES

The version 5.3 of AVBP (including already several improvements of version 5.4) is used for this calculation. The residual stress model is Smagorinsky's and the numerical scheme Lax-Wendroff.
The simulations are carried out on a tetrahedral mesh extending from a imaginary plenum inlet to an imaginary chamber outlet. Two cuts through the domain are given in Figure (7.3) to illustrate the domain. The chosen cuts go through the planes of the fuel injection in order to get a better idea of the burner. The plenum inlet is beyond the left edge of Figure (7.3), the chamber outlet beyond the right edge. Both in- and outlet are acoustically non-reflecting in the range of the eigen-frequencies of the configuration. The remaining inlets for fuel, shielding air an

| Type | Location | Description | Reynolds | $\phi$ | $\alpha_{st}$ |
|---|---|---|---|---|---|
| LDA | $y = z/\tan(109^o)$ | Water-Channel Experiments using Laser Doppler Anemometry. Data provided by Alstom Power Ltd. | 109000 | no | - |
| PIV | $y = 0$, $z/\tan(109^o)$ | Water-Channel Experiments using Particle Image Velocimetry. Data provided by Alstom Power Ltd. | 109000 | no | - |
| LIF | $x/D = -0.66$, $-0.50$, $-0.33$, $-0.18$, $0.08$ | Water-Channel Experiments using Laser Induced Fluorescence. Data provided by Alstom Power Ltd. | 109000 | 0.49 ($\widehat{=}$2%) | 20%, (40%) |
| LES 0 | any | AVBP simulation on mesh I with 1.5% (of total mass flow) injection through lance. No turbulent inflow. | 68000 | 0.47 | 20% |
| LES I | any | AVBP simulation on mesh I with 1.0% (of total mass flow) injection through lance. **No turbulent inflow**. | 68000 | 0.47 | 20%, (40%) |
| LES II | any | AVBP simulation on mesh II with 1.0% (of total mass flow) injection through lance. **Turbulent inflow**. | 68000 | 0.47 | 20% |

Table 7.1: Overview of the non-reacting cases.

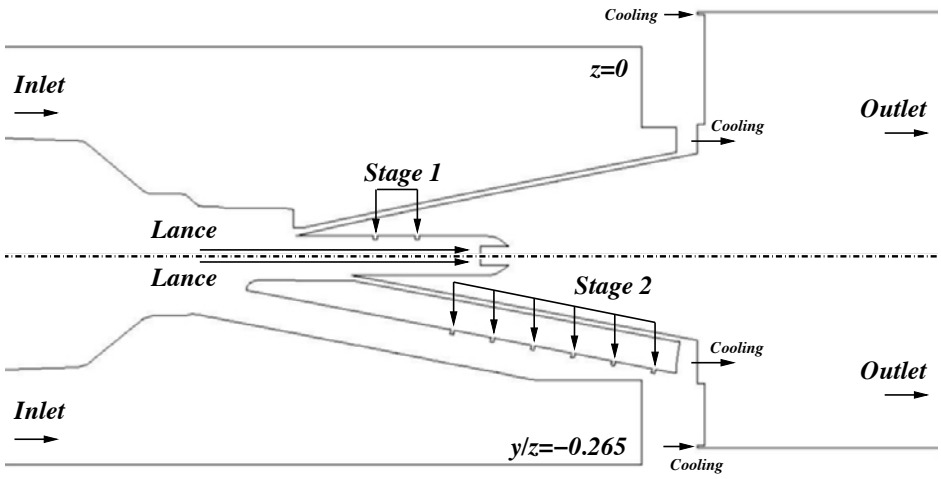


Figure 7.3: Two cuts through the domain showing all computational boundaries.

cooling air, which are also seen in Figure (7.3) are acoustically reflecting. Table (7.2) summarises the thermodynamic and acoustic properties of all boundary conditions. Further details are given below.

### Conditions

The mean pressure of the configuration is set to 506.5 $kPa$. The temperature of the inflowing air is 673 $K$ ($X_{O_2} = 0.21$, $X_{N_2} = 0.79$). The fuel is methane and injected at 293 $K$ ($X_{CH_4} = 1.00$). The Reynolds number based on the burner exit diameter $D = 0.07$ $m$, the mean velocity at the burner exit $u_{ref} = 30$ $m/s$ and the viscosity of air at 673 $K$ is 68'000.

### Plenum

The plenum used for experiments was found to have a very low reflection coefficient, so it was decided to include a simpler plenum with a non-reflecting inlet in the simulation. It is 0.3 $m$ long and has a square cross section with an edge length of 0.12 $m$. It includes a cylindrical structure holding the burner. the cylinder is aligned with the plenum axis at has a radius of 0.0416 $m$ at the plenum inlet.
Two different grids are used for the plenum. They are summarised in terms of nodes in the respective regions in Table (7.3). Mesh I neglects turbulent inflow into the plenum and is consequently very coarse in the plenum. Mesh II has a sufficient resolution to convect turbulence (20% of the mean flow) coming from

| Boundary | Mass flux | Pressure | Temperature | Species | Relax |
|---|---|---|---|---|---|
| Inlet plenum | 0.2634 $kg/s$ | - | 673 $K$ | air | 500 |
| Inlet lance | 0.0029 $kg/s$ | - | 673 $K$ | air | $10^4$ |
| Stage 1 | 0.0016 $kg/s$ | - | 293 $K$ | $CH_4$ | $10^4$ |
| Stage 2 | 0.0064 $kg/s$ | - | 293 $K$ | $CH_4$ | $10^4$ |
| Cooling front | 0.0164 $kg/s$ | - | 673 $K$ | air | $10^7$ |
| Cooling film | 0.0090 $kg/s$ | - | 453 $K$ | air | $10^7$ |
| Outlet | - | 506.5 $kPa$ | - | - | 150 |
| Walls plenum | No-slip isothermal at 673 $K$ | | | | |
| Other walls | Wall-function isothermal at 673 $K$ | | | | |

Table 7.2: Boundary conditions for the LES with $\alpha_{st} = 20\%$ and $\phi = 0.47$.

the plenum inlet. The turbulence specified at the inlet is close to homogeneous, isotropic turbulence [93]. The plenum walls are no-slip, isothermal ($T = 673\ K$).

**Burner**

The ev7is contains nearly half of the grid nodes used for the whole configuration. The fuel injections are modelled by short holes with acoustically reflecting inlets (see Figure (7.3) and Table (7.2)). Their diameter was meshed with approximately 6 grid nodes. All walls are isothermal wall-function walls (see Section (2.3)) imposing the temperature of the air ($T = 673\ K$). The shielding air is 1.0% of the total air mass flow. The CTRZ is very sensitive to the shielding air. A simulation with 1.5% of shielding air already shows a considerable modification of the CTRZ position. The amount of fuel injected is fixed to obtain an equivalence ratio of $\phi = 0.47$ in the chamber. 20% of the fuel comes through stage 1, 80% through stage 2.
The two slots, where the main air flow enters the burner lie in the $x-z$ plane.

| | plenum | burner | chamber | total |
|---|---|---|---|---|
| mesh I (steady inflow) | 40'000 | 230'000 | 230'000 | 500'000 |
| mesh II (turbulent inflow) | 190'000 | 230'000 | 80'000 | 500'000 |

Table 7.3: Resolution (number of nodes) of the two computational grids used for the non-reactive simulations.

### Chamber

The combustion chamber has the same transverse dimensions as the experimental chambers ($l_y = 0.14\ m$, $l_z = 0.11\ m$) but an arbitrarily fixed length of $l_x = 0.5\ m$. This is long enough to exclude any influence on the CTRZ. As the outlet is acoustically non-reflecting, the length is not important.
The chamber walls are adiabatic wall-function walls. The air cooling at the burner exit (also called front) is included through long rectangular inlets with a velocity distribution that is mimicking the little holes. These inlets have a span wise resolution of only 3 points which makes them nearly equivalent to simple source terms. The cooling air is identical with the air entering the plenum.
The chamber also includes film cooling for the chamber walls. The experimental chamber has quartz-glass windows to allow optical access, which must be cooled. In the LES, this is modelled by a continuous, low-speed inlet at the outer rim of the front plate. As the film cooling air passes through the water-cooled front plate, its temperature in considerably lower than the principle air flow (see Table (7.2)).
For mesh I, the grid of the chamber consists as of many nodes as the burner grid. This high resolution of the chamber is essentially for the reactive application afterwards. Mesh II, which will only be used for non-reactive simulations has therefore a reduced resolution in the chamber (see Table (7.3)).

### Time-Scales

The time-scales defined in Section (1.5.1) can be evaluated on the basis of the described configuration. The domain length is $l_c \approx 0.9\ m$, the speed of sound $c$ in the chamber approximately 450 $m/s$. The acoustic time is then:

$$\tau_{ac} \approx 2\ ms$$

Experience tells that high frequency phenomena above $f_{max} = 10\ khz$ are not of interest, so the acoustic recoding time should be:

$$\tau_{ar} \approx 0.05\ ms$$

The inlet has a surface of $A_{in} = 9 \cdot 10^{-3}\ m^2$ and the whole domain a volume of $V = 11.2 \cdot 10^{-3}\ m^3$. With an inlet velocity of approximately $V = 13\ m/s$, the convective time is

$$\tau_{cv} \approx 95\ ms$$

Approximating the integral turbulence length scale with approximately a third the burner exit diameter or a sixth of the chamber transverse dimension ($l_t = 0.02\ m$), and the associated fluctuations with a third the mean velocity at the burner exit ($u_t' = 10\ m/s$), the integral turbulence time scale is:

$$\tau_{ti} \approx 2\ ms$$

These parameters were already used for the evaluation of the Damköhler number in Section (5.1) and are based on the observed flow in the ev7is burner.
According to Section (1.5.1), the following times should be used for the acquisition of statistics:

$$T_{av} = \max(\tau_{ac}, \tau_{ti}) \cdot 10 = 20\ ms \qquad \text{total recording time} \tag{7.3}$$

$$\Delta t_r = \min(\tau_{ar}, \tau_{ti}/40) = 0.05\ ms \qquad \text{time between two samples} \tag{7.4}$$

Assuming that the hole diameter (1 $mm$) is the smallest geometric feature to be resolved (in that case with 6 nodes), $\Delta x$ from Equation (1.51) will be 0.2 $mm$. With a sound speed of 500 $m/s$ and a convective velocity at the holes of 300 $m/s$, Equation (1.51) gives approximately 0.25 $\mu s$ for the time step. The time step of the actual LES is $\Delta t = 0.1\ \mu s$. This discrepancy must be be associated with even smaller cells needed for the unstructured mesh at some locations near the holes.
In summary, every $\Delta t_r/\Delta t = 500$ iterations, a solution should be added to the statistics and all quantities at a few specific locations should be recorded. This should be done, once the LES is one convective time old ($\tau_{cv}/\Delta t = 950'000$ iterations) for the duration of $T_{av}/\Delta t = 200'000$ iterations.

### 7.2.2 Experimental Setup

The results of the experiments presented in the following were obtained by Alstom Power Ltd. (CH). They represent measurements carried out in a water channel and are therefore incompressible. It is assumed that compressibility only plays a minor role in the non-reacting flow. It might influence slightly the trajectory of the high Mach number fuel jets, but this is unclear.
A photograph of the partially transparent configuration is shown in Figure (7.4). Plenum, chamber and one half-cone of the burner are transparent to allow optical access. The water flows from bottom to top (which is left to right in the picture). The Reynolds number of the investigated flow (based on burner diameter, flow velocity at the burner exit and the viscosity of water at ambient temperature) was $109'000$. Only the air cooling at the burner front is present, not the film colling at the edges of the front plate. All used measurement techniques described in the following provide mean values and standard deviations (rms) based on measurement times much longer than any characteristic time scale present in the flow.

#### Laser Doppler Anemometry (LDA)

Laser Doppler Anemometry is a single point optical measuring technique which enables the velocity of the seeded particles conveyed by a fluid flow to be measured in a non-intrusive manner. The seeded particles are big enough to scatter

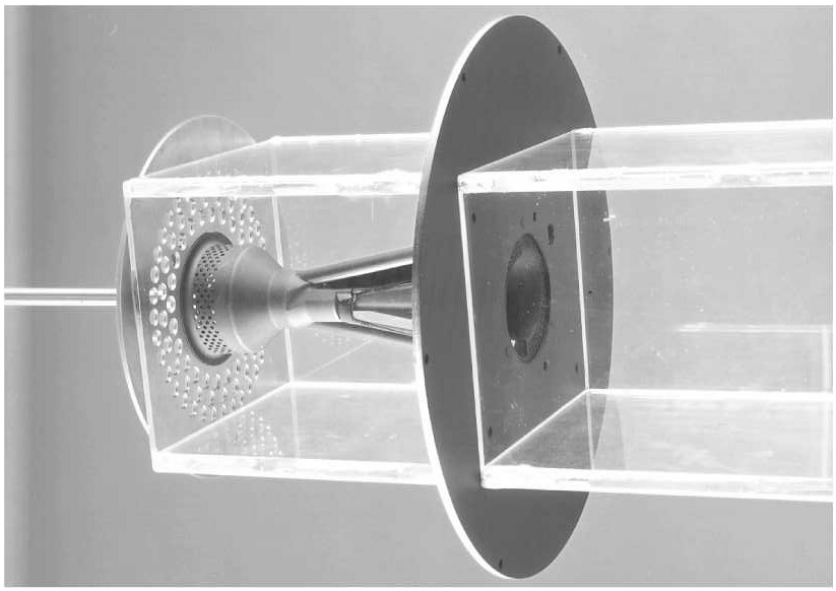

Figure 7.4: The transparent plenum, burner and chamber used for the water channel experiments. Picture provided by Alstom Power (CH).

sufficient light for signal detection but small enough to follow the flow faithfully. The area of interest within the flow field is sampled by a crossed-beam in a point by point manner. By analysing the Doppler-equivalent frequency of the laser light scattered by the seeded particles within the flow, the local velocity of the fluid can be determined.
More information on this technique is found in the book by Durst et al. [25].

**Particle Image Velocimetry (PIV)**

Particle Image Velocimetry is an optical measurement technique which provides a means of measuring the velocity of seeded particles in the flow of interest over a plane using a CCD camera. The measurement area within the flow field is defined by the position and physical dimension of a laser light sheet. With the illumination of two short duration laser flashes in the measurement area, a double-exposure of the flow field is captured. Once the spatially displaced images are stored in two separate frames, each velocity vector is extracted by performing mathematical correlation analysis on a cluster of particles within each interrogation region between the two frames.
More information on this technique is found in the review by Adrian [1].

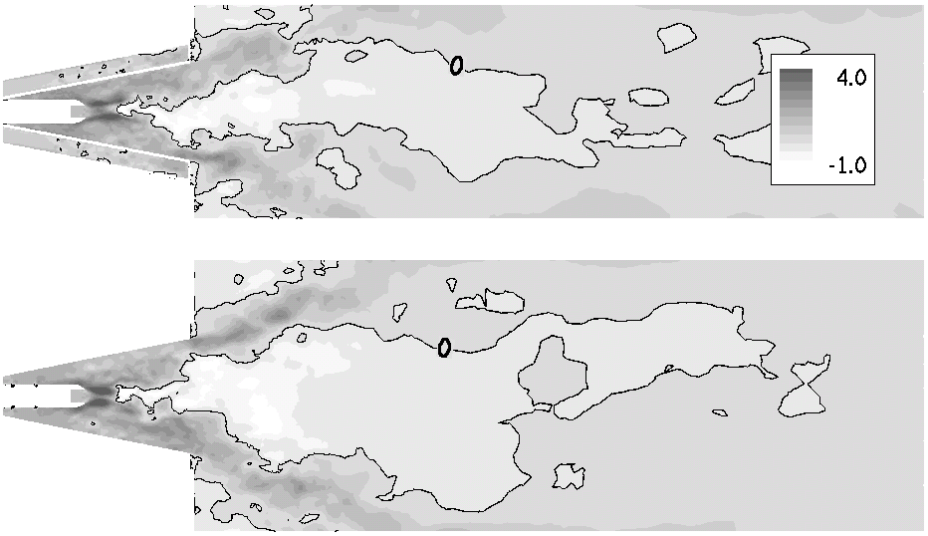


Figure 7.5: Instantaneous axial velocity (normalised by $u_{ref}$) of LES I. Top: $x-z$ plane; bottom: $x-y$ plane.

**Laser Induced Fluorescence (LIF)**

Laser Induced Fluorescence is an optical measurement technique which provides a means of measuring the concentration of a fluorescent substance (replacing the fuel) in the flow of interest over a plane using a CCD camera. The measurement area within the flow field is defined by the position and physical dimension of a laser light sheet. The fluorescent substance emits at a frequency different from the frequency of the exciting laser. This makes the measurement of the emission of the fluorescent substance possible.
More information on this technique is found for example in the paper by Bellerose et al. [6].

## 7.3 Qualitative Analysis of Unsteady Flow

Before collecting statistics of an LES, it is necessary to make sure that the instantaneous solutions make sense. This also helps for the understanding of the average solution.

### 7.3.1 CTRZ

Figure (7.5) shows two cuts through fields of instantaneous axial velocity. The presented solution (LES I) is without turbulent flow in the plenum but apparently the swirl flow creates considerable amounts of turbulence. The iso-contour $u = 0$, which indicates flow reversal corresponds approximately to the CTRZ. The exit of the chamber is not seen in the plots, but it is evident that the CTRZ does not extend to the outlet. However, it extends well into the burner and looks very asymmetric. Where this asymmetry comes from will be detailed in the following section.

### 7.3.2 Coherent Structures

As expected, this flow exhibits a large coherent structure due to the vortex breakdown of the swirl flow. It is a precessing vortex core, which explains the strong asymmetry in the instantaneous velocity fields. Figure (7.6) shows on the left a view from the combustion chamber on this PVC. It is visualised by an iso-surface of pressure. It has the form of a corkscrew, turning in the same direction as the swirling motion. The vortex core turns also in that direction.
The grid used for LES II is finer upstream of the burner and turbulence is injected through the inlet (see Table (7.3)). For this simulation, the PVC is less evident (seen on the right of Figure (7.6)). The incoming turbulence structures perturb the PVC, but it is still clearly identifiable with the pressure iso-surface. The impact of this coherent structure on the flow becomes clearer when looking a the spectra of velocity and pressure at a location close to the burner exit. They are presented in Figure (7.7). The magnitude of the Fourier transform of pressure (on the right) shows for both simulations a distinct peak. For LES I it is close to 500 *hz*, for LES II 600 *hz*. Why this difference in frequency occurs is an open question.
The magnitude of the Fourier transform of axial velocity on the left of Figure (7.7) shows a distinct peak for LES I, also at 500 *hz*. This suggests that the PVC is responsible for the creation of an important part of turbulence. The spectrum for LES II does not show a single, dominant peak. This is easily explained: The incoming turbulence perturbs the PVC, and its impact on the velocity field will be reduced. When it breaks up, this weaker PVC will create less turbulence which will be masked by the already present turbulence.

### 7.3.3 Mixing

Only non-reactive LES with a staging ratio of $\alpha_{st} = 20\%$ are presented here. A typical snapshot of the mixing process in two cuts is shown in Figure (7.8). A logarithmic scale is used to visualise the fuel mass-fraction: the stage 1 jets are weaker than the stage 2 jets. The fuel coming from stage 1 sticks to the shell

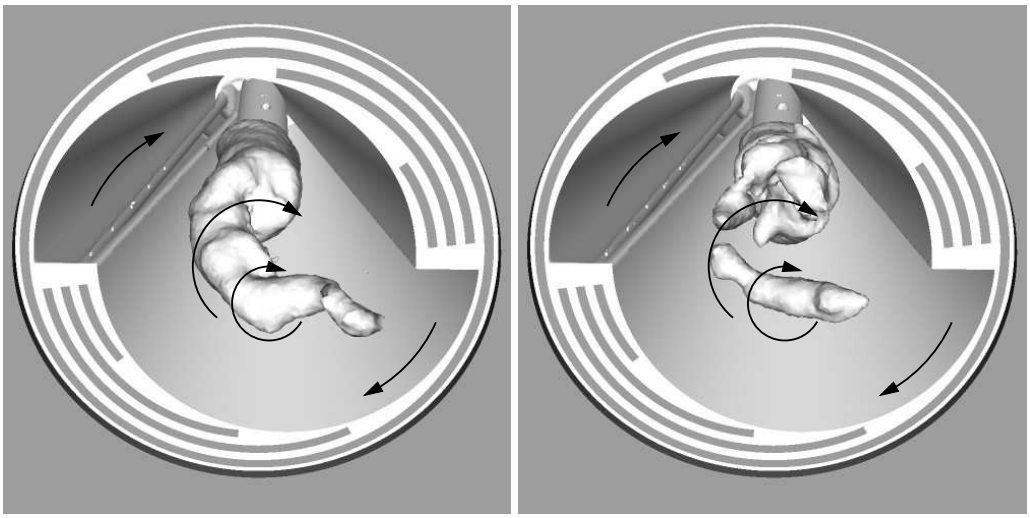

Figure 7.6: View from the combustion chamber on the burner. The PVC is visualised by pressure iso-surfaces. Left: LES I; right: LES II. Swirl and PVC rotation is illustrated by arrows. These pictures are found in colour in Appendix (A), Figure (A.1).

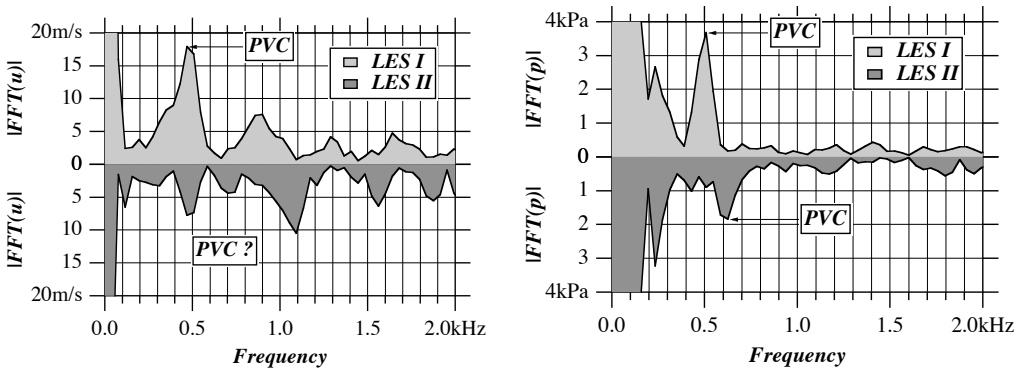


Figure 7.7: Spectra of velocity (left) and pressure (right) at a location close to the burner exit for LES I and II.

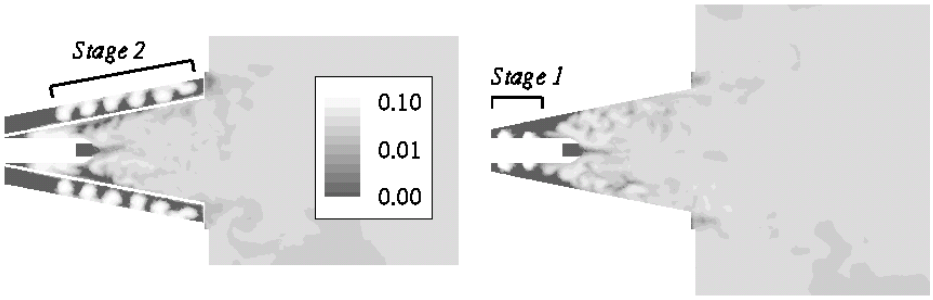


Figure 7.8: Snapshot of the mixing process (fuel mass fraction) in two cuts. Top: $x-z$ plane; bottom: $x-y$ plane.

of the lance whereas the stage 2 jets are clearly detached from the burner shell. The image suggests quite rapid mixing. Due to the rather low resolution near the injections, small scale structures are not seen near the injections.

### 7.3.4 LES Quality

As argued in Section (3.2.5), the evaluation of $Q_{LES}^{RANS}$ for a simulation provides at least an idea of the LES resolution. Computing this value for all nodes present in LES I, statistics will give information about its repartition. Therefore the domain is separated into plenum, chamber and burner. The result is shown in Figure (7.9). Well over 50% of the computational nodes have a $Q_{LES}^{RANS}$ of greater the 0.8. This value is mainly attained in the chamber and the centre region of the burner. Therefore, LES I corresponds to an LES-NWM (definition see Section (1.5.3)) in these regions. It is also seen that the burner has a considerable amount of nodes that correspond more to a RANS simulation then a LES. This comes from the strongly under-resolved fuel injections and the inflow, not containing any turbulence. This explains also why the plenum has $Q_{LES}^{RANS}$ values near $-1$.

## 7.4 Velocity Measurements

Time averaging is carried out with the previously determined times $T = 20\ ms$ and $\Delta t_r = 0.05\ ms$. An impression of the mean axial velocity obtained from LES I is given in Figure (7.10). Comparing with the snapshot of Figure (7.5) shows that the mean flow is symmetric but not completely smooth (as it would be in a RANS simulation). This confirms that the choice of averaging parameters is reasonable. An interesting observation is that the zone of negative axial velocity is not directly extending from the chamber into the burner, but is cut in two at the burner exit.

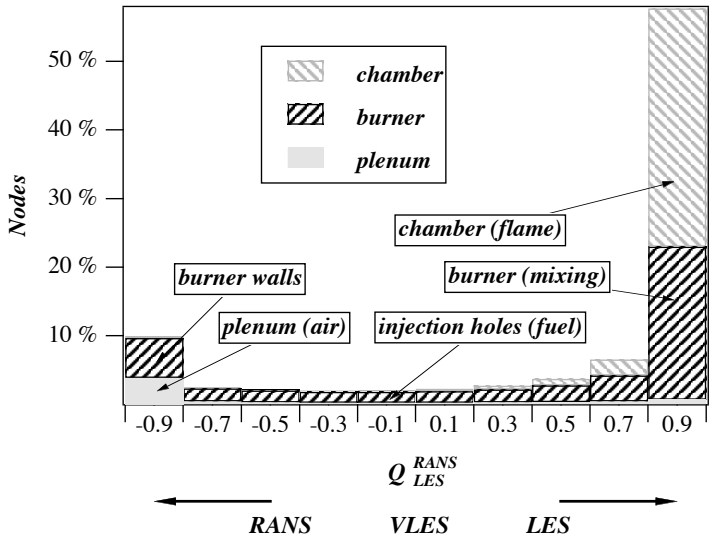


Figure 7.9: Quality assessment for LES I. In the important regions where mixing and combustion (will) take place, the simulation is a LES-NWM (definition see Section (1.5.3)).

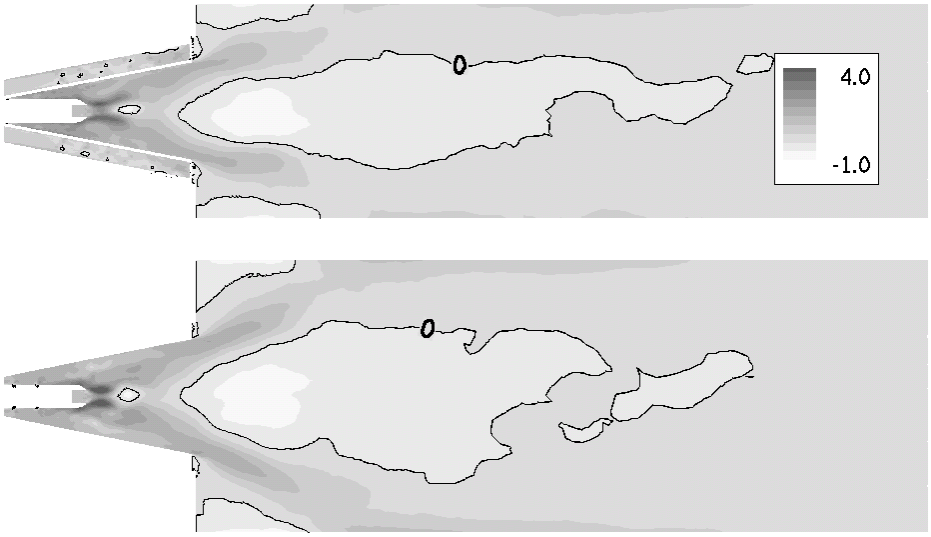


Figure 7.10: Mean axial velocity (normalised by $u_{ref}$) of LES I. Top: $x-z$ plane; bottom: $x-y$ plane.

This must be attributed to the PVC motion. Also the opening angle of the flow in the chamber differs in the two presented cuts, since the chamber is rectangular and not square.
In order to make quantitative comparisons between experiment and simulation, several cuts through the domain are defined. For the LDA measurements these cuts lie in the $y = z/\tan(109^o)$ plane at $x/D = -0.5$, 0.5, 0.75 and 1.0. The results are presented in Figure (7.11). Both axial mean and rms velocity (seen in the left half of the figure) are in excellent agreement with LES I. The opening angle in the chamber, the position of the CTRZ and even the fluctuation levels and locations are correctly predicted.
The radial mean and rms velocity are well predicted in the burner, but in the chamber (most pronounced at $x/D = 0.5$), the mean and rms profiles do not completely match. Close to this position, the flow passes through a phase, where radial velocity is nearly zero. This is seen by comparing the radial velocity at $x/D = 0.5$ and $x/D = 0.75$. Therefore, the results at this location are very sensible to the exact position of the zero radial velocity region.
To get a better understanding of the observed differences and an idea of the measurement technique's influence, the same simulation is compared to PIV data in the same cut-plane. Additionally, cuts at $x/D = -0.75$, $-0.25$ and 0.25 are available. This is presented in Figure (7.12). Again, the mean axial velocity cuts are in excellent agreement. The axial rms velocity in the chamber is very well predicted, but in the burner, the LES predicts less turbulence. This might be due to the lack of turbulent motions upstream of the burner for this simulation. It is also noticed that the prediction of the axial (and radial) rms velocity in the burner by PIV is different from the LDA predictions. There seems to be as much difference between one measurement technique and another and the LES results. This probably explains the discrepancies between LES and LDA.
The additional cuts allow a closer view on the differences in radial mean velocity distribution, observed for the LDA comparison. In the burner and at $x/D = 0.25$ the radial velocity is well predicted. Only at the cuts downstream in the chamber, the radial mean velocity does not match very well. The radial rms velocity is nicely predicted in the chamber, but in the burner, as for the axial rms velocity, the LDA data was better matched by the LES. Sufficient turbulence seems to miss upstream in the burner.
Therefore the PIV data is compared in Figure (7.13) to LES II, where less resolution is present in the chamber, but the plenum is sufficiently meshed to explicitly introduce turbulence via the plenum inlet. Axial and radial mean velocity are well predicted inside the burner, however in the chamber the opening angle of the jet is not big enough and the already known problems in radial velocity appear. The deterioration of the results in the chamber compared to LES I is attributed to the lower resolution there. Surprisingly, the radial and axial rms values are not too

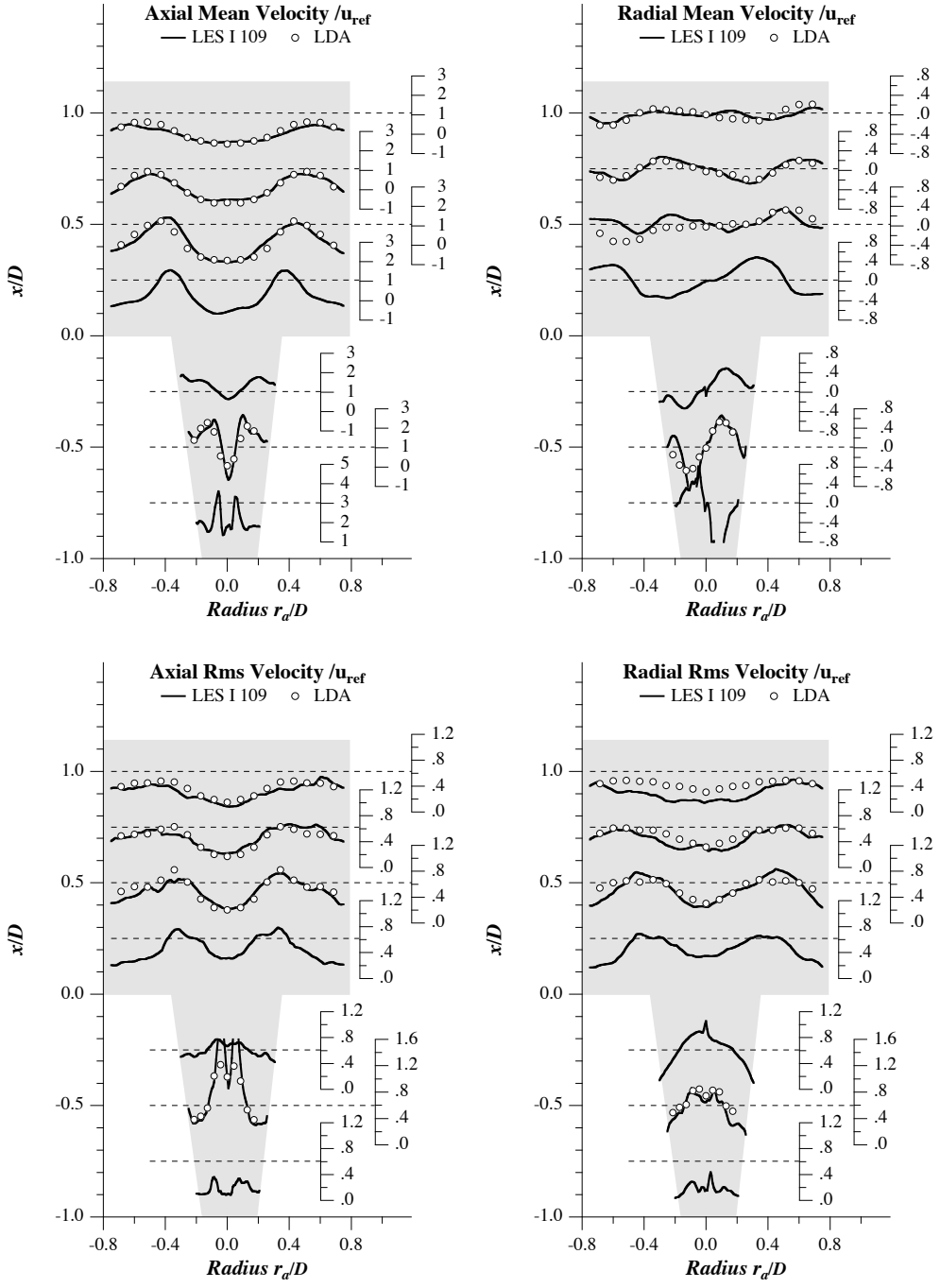


Figure 7.11: Comparison of the velocity fields provided by LES I and LDA (109°).

bad in the chamber. Apparently the coarse grid in the chamber manages to sustain the important large turbulence structures. In the burner, both axial and radial fluctuations are not really better predicted than without turbulence injection. This points to the conclusion, that the resolution in the burner is the limiting factor. The narrow upstream part of the burner is not very well discretized. A very detailed mesh in the burner would be much too expensive. Keeping in mind that these simulations are performed in order to validate the starting point for reactive simulations, this drawback has to be accepted.

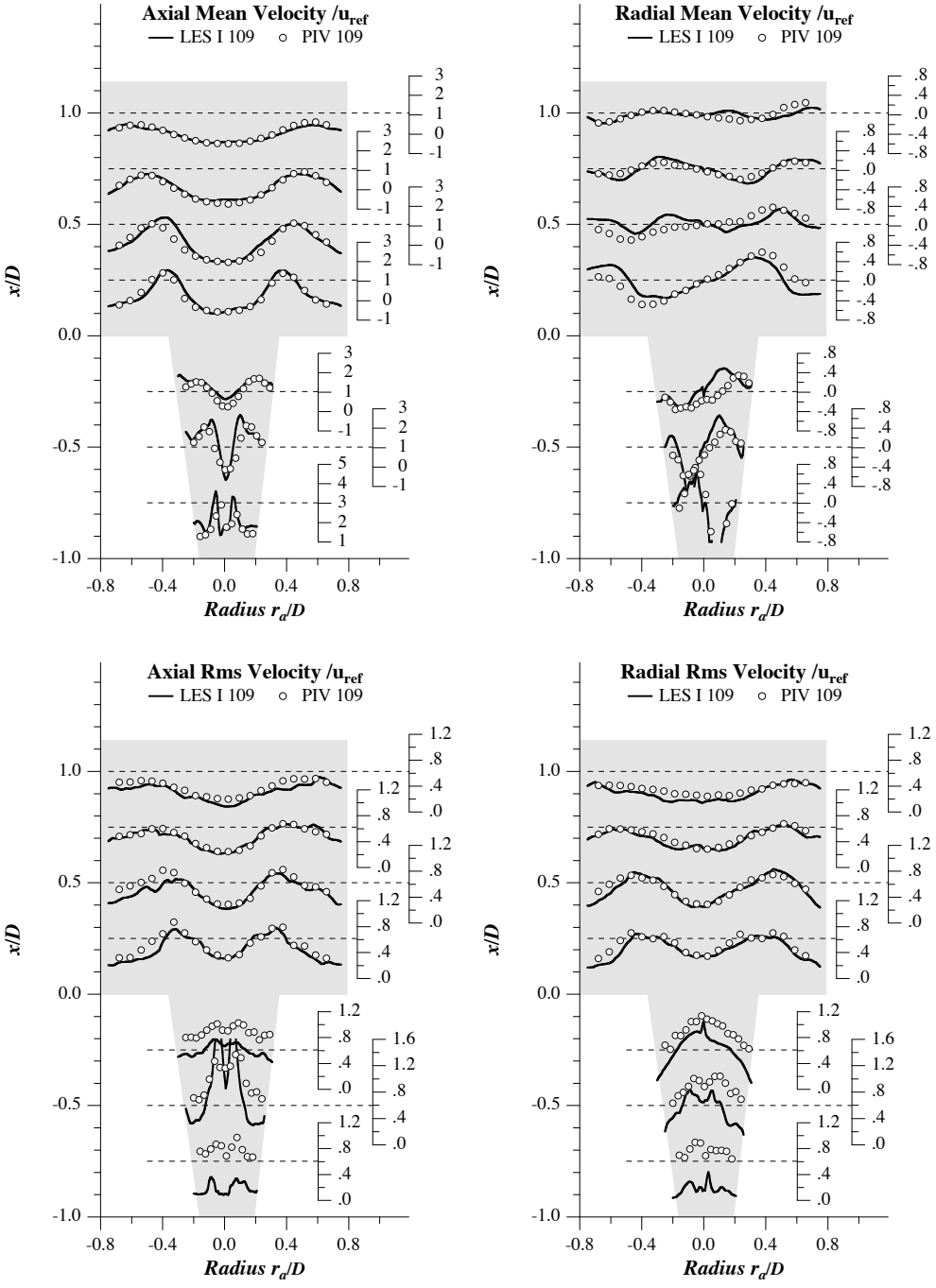


Figure 7.12: Comparison of the velocity fields provided by LES I and PIV (109$^o$).

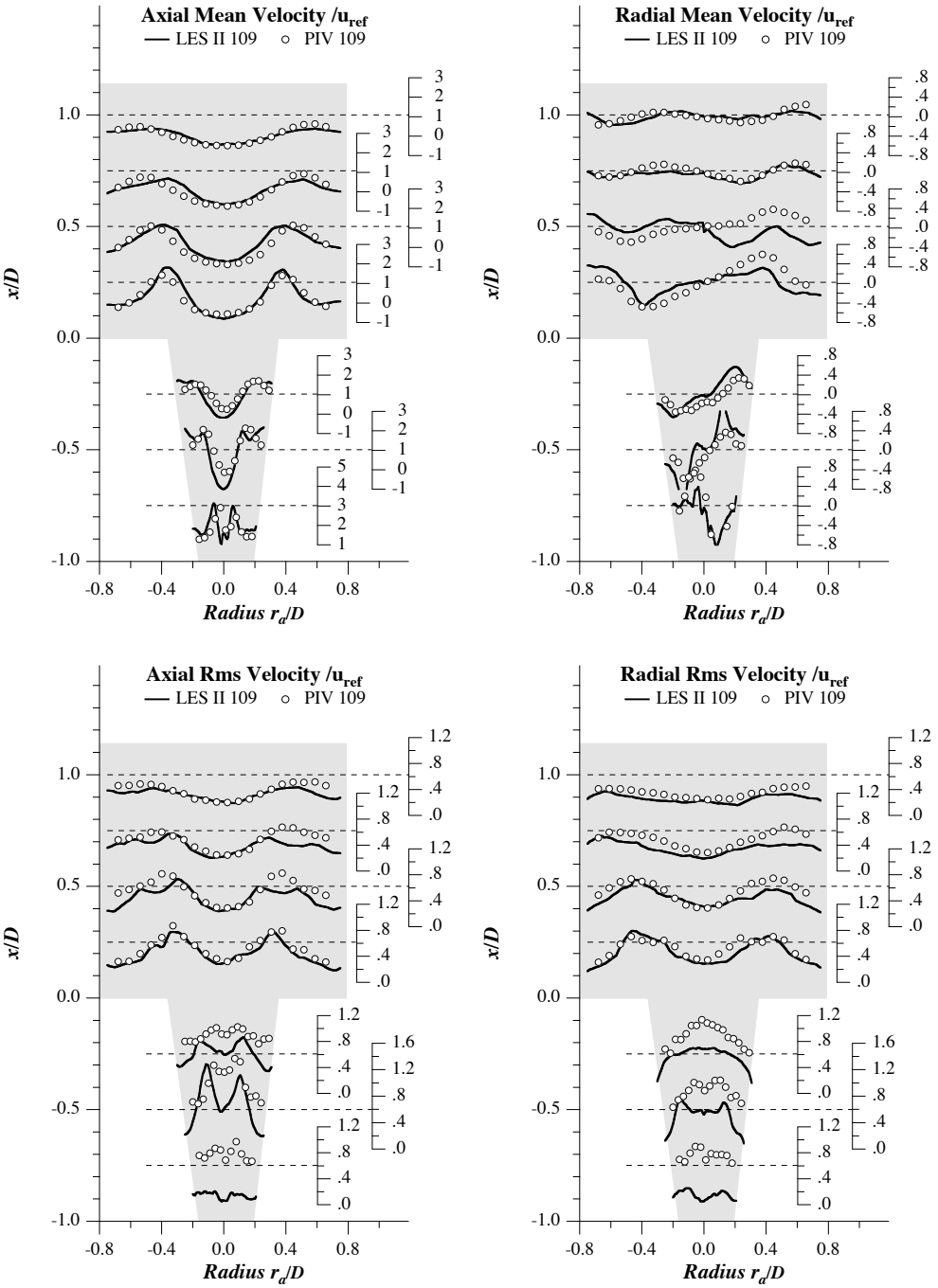


Figure 7.13: Comparison of the velocity fields provided by LES II (turbulence injection) and PIV (109$^o$).

# 7.5 Mixing

## 7.5.1 Global Mixing Indexes

The LIF measurements provide mean and rms fuel mass-fractions at 5 locations ($x/D$ =const.). Four of them are inside the burner and one is located just after the burner exit. Both the LES and the LIF fields were restricted to the area inside the burner shells, masking the region close to the fuel injections (to avoid any errors introduced by slight differences of the $x/D$ values).
To evaluate the mixing in a global manner, mixing indexes are calculated:

$$U_S = \frac{\left\{\overline{Y_{CH_4}}\right\}^2}{\left\langle\overline{Y_{CH_4}}\right\rangle \cdot \left(1 - \left\langle\overline{Y_{CH_4}}\right\rangle\right)} \qquad \text{spatial unmixedness} \qquad (7.5)$$

$$U_T = \frac{\left\langle Y_{CH_4,rms}\right\rangle^2}{\left\langle\overline{Y_{CH_4}}\right\rangle \cdot \left(1 - \left\langle\overline{Y_{CH_4}}\right\rangle\right)} \qquad \text{temporal unmixedness} \qquad (7.6)$$

where $\langle\cdot\rangle$ represents a spatial average and $\{\cdot\}$ a spatial standard deviation (or rms). For every $x/D$ location both indexes are calculated for LES I, LES II and for the

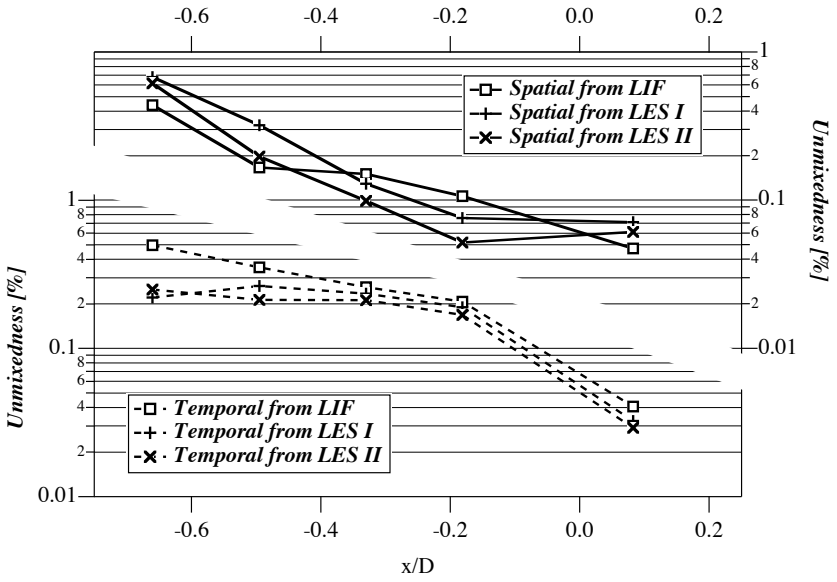


Figure 7.14: Spatial and temporal unmixedness from LIF and LES.

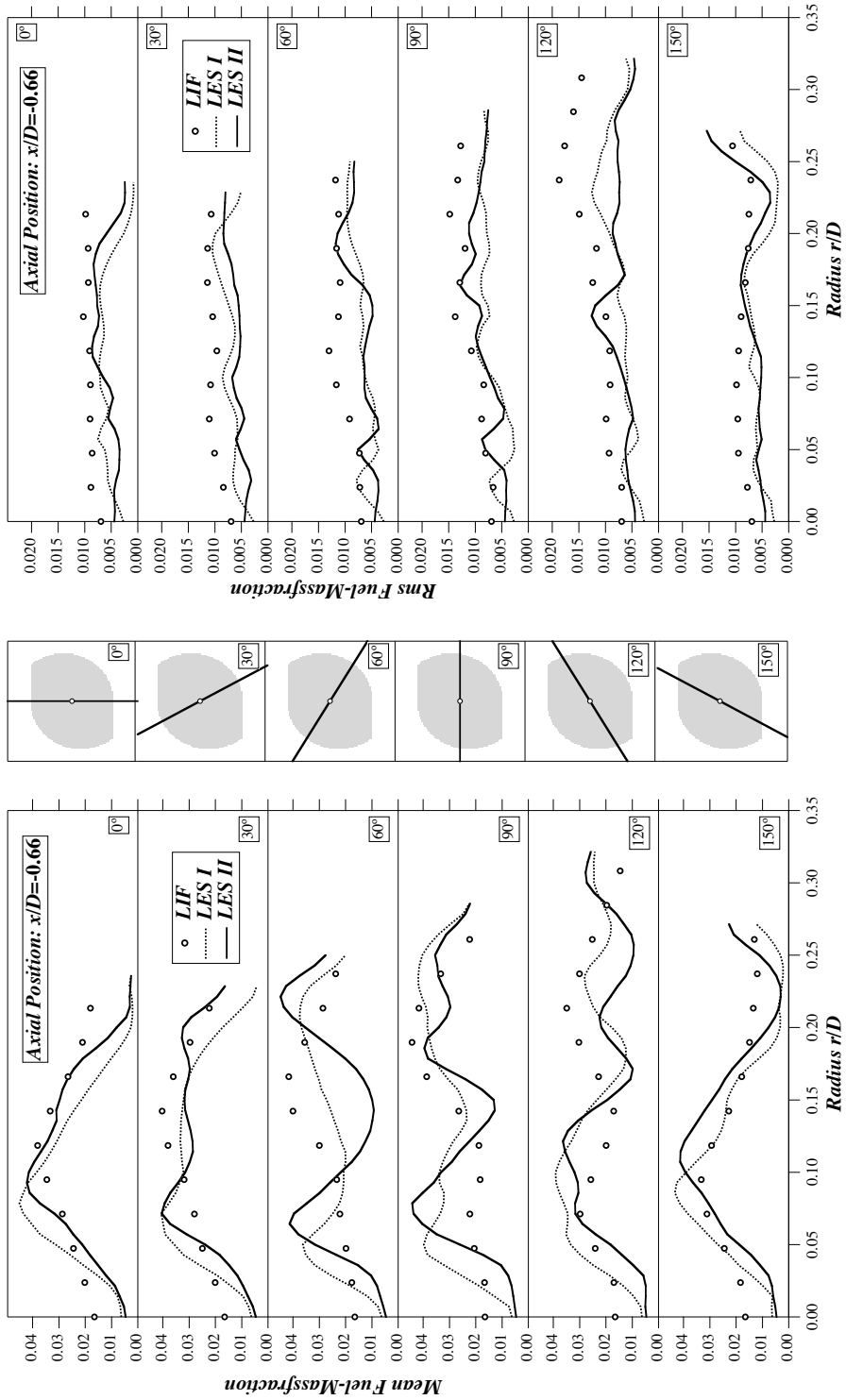


Figure 7.15: Comparison of LES and Experiment at $x/D = -0.66$.

LIF measurements. They are compared to each other in Figure (7.14), spatial unmixedness in the top half of the graph, temporal unmixedness in the bottom half.
Spatial unmixedness is lower for the case with incoming turbulence (LES II) than for the one without (LES I). Both LES under-predict mixing upstream in the burner and over-predict mixing near the burner exit. In the chamber, mixing is again under-predicted. Why this is so will be detailed by looking at cuts through the domain in the next section.
Temporal unmixedness is over-predicted by both LES. As expected, at the first measurement location this error is stronger for the case without incoming turbulence. Downstream, the case with incoming turbulence predicts better temporal mixing.
It is already possible to conclude that as for velocity measurements, the introduction of turbulence through the plenum does not influence the results strongly.

### 7.5.2 Mixing Fields

Figure (7.15) shows cuts in radial direction at $x/D = -0.66$. In order to reduce the data to compare, the flow was assumed to circumferentially repeat itself after $180^o$. Globally, both LES show roughly the same behaviour comparing to the LIF: The mean values show that the LES under-predicts mixing (clearly seen at $0^o$) and fluctuations. Both observations are in line with the statements made on spatial and temporal unmixedness.
Travelling downstream to $x/D = -0.33$, Figure (7.16) shows already a rather well mixed flow. The mean profiles of both LES compare well to the LIF, only at $150^o$ mixing seems completely wrong. The rms values are accurately predicted in magnitude, there is however some deviation in form at the same locations where the mean values show problems.
Figure (7.16) details the mixing outside the burner, just at the beginning of the chamber. The mean profiles at angles $0^o$ to $120^o$ show that more cooling air is injected in the LES than in the experiment. The cooling air mass-flux in the LES was fixed from the design objectives of the burner and it is not clear if this part of the burner is correctly predicted by the water channel experiments. At $150^o$, again an under-prediction of mixing from the last injection is observed. This and the cooling air explain why the spatial unmixedness has an error in the opposite direction outside the burner. The rms values are nicely predicted for all angles.
In Appendix (A), coloured contour plots at the locations discussed above are displayed (Figures (A.2) to (A.4)). There, it is seen that $180^o$-symmetry is not always satisfied. This is most pronounced for LES I at $x/D = -0.66$. With incoming turbulence (LES II), the flow becomes more symmetric. It does not become completely symmetric because of the fuel jets being deviated to some degree by the mesh. This is not surprising as the resolution near the jets is very low (taking as a

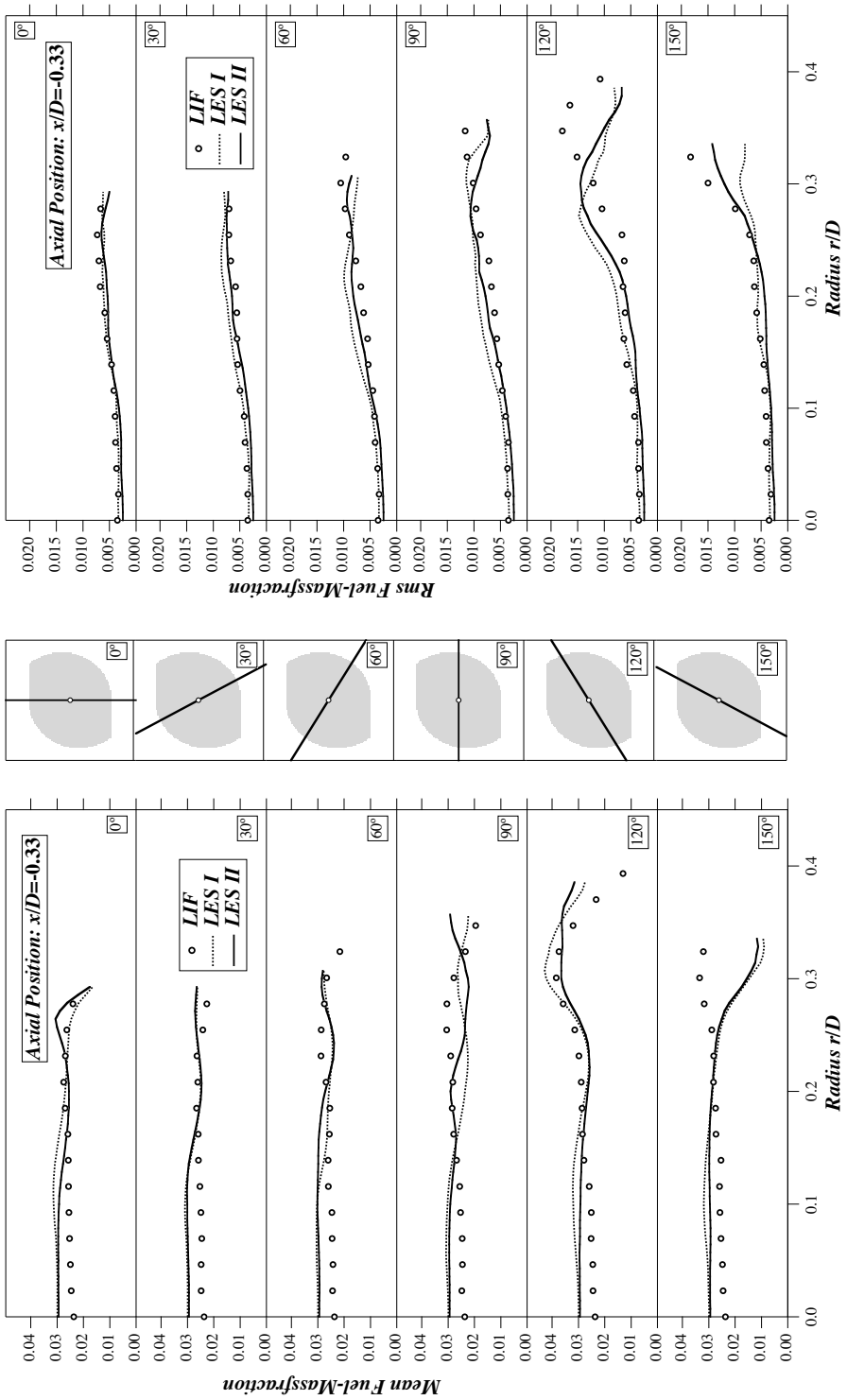


Figure 7.16: Comparison of LES and Experiment at$x/D = -0.33$.

reference the hole diameter). The contour plots also show that the line cuts may show strong errors if the trajectories of the jets are slightly wrong predicted.
As already seen when analysing the line cuts, downstream in the burner and in the chamber, mixing is correctly predicted by both LES. These results show that if combustion takes place far from the fuel jets, incoming turbulence and a higher resolution are not really necessary. As this is the case for the present burner, LES I will serve as a starting point for the reactive simulations in the next chapter.

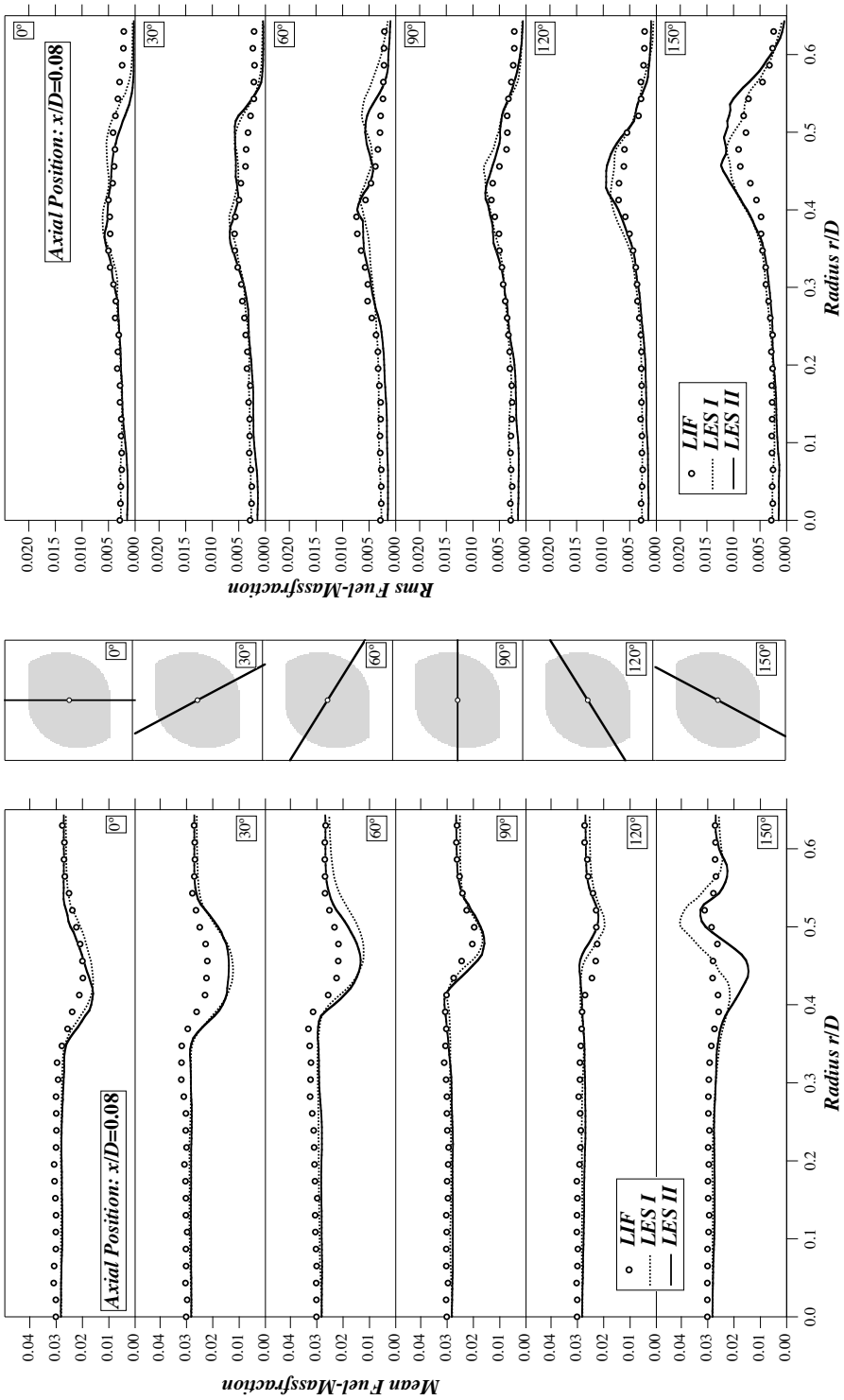


Figure 7.17: Comparison of LES and Experiment at $x/D = 0.08$.

# Chapter 8

# Reactive Simulations of the ev7is

## 8.1 Combustion Setup

### 8.1.1 Experimental Setup

DLR in Stuttgart tested the ev7is on a medium pressure test rig (Figure (8.1)). The chamber length is $l_x = 0.42\ m$. It terminates in a sudden contraction, which is leading into a chimney and then into a larger duct where the exhaust gases are cooled down. The chamber outlet geometry was empirically adjusted to give an instability frequency of the order of $250\ hz$.
The cold air is entering the pressurised vessel flowing around the combustion chamber, thereby cooling it. The so preheated air is entering the plenum and passes through the burner where the fuel is injected. Additionally, air is passing through the front of the burner ("impingement" cooling) and along the lateral chamber walls ("film" cooling). The latter is cooled down as it passes through the chamber front plate, which is water-cooled.
A wide range of pressures, adiabatic flame temperatures and staging ratios were tested. Here only the results at operating conditions as listed in Table (8.1) are of interest. The experimental chamber is equipped with quartz-glass windows, allowing optical access. Several different measurement techniques as described in the following were used.

#### $OH^*$ Chemiluminescence

To characterise heat release in the chamber, the radiation intensity of the $OH$ radical ($OH^*$) is measured. This radical appears exclusively in the reaction zone and its life span is short. Its concentration is small and self-absorption is negligible. It is supposed to be linked linearly to heat release when the equivalence ratio does not vary too much [78]. This is an assumption which is acceptable when the flame

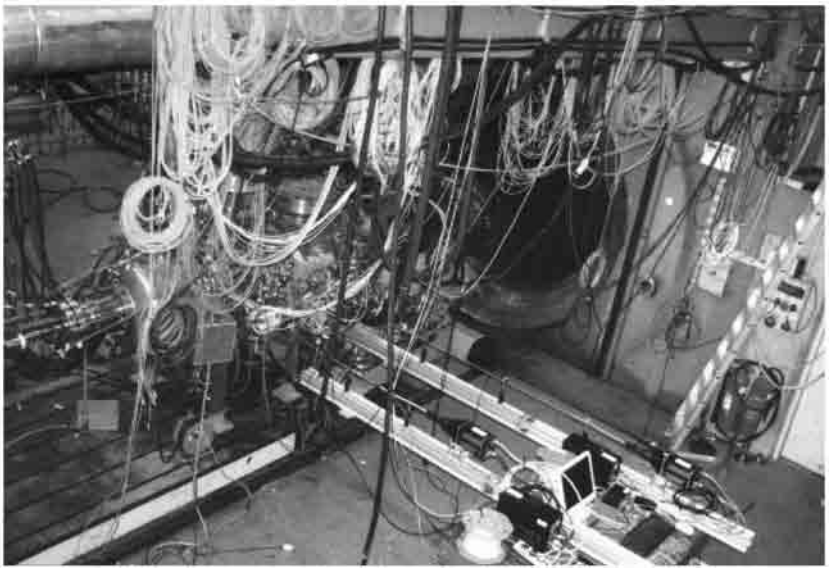

Figure 8.1: Medium pressure test rig equipped with ev7is (DLR, Stuttgart).

is burning outside the burner but may fail for regimes where the flame flashes back.
Through the quartz-glass windows of the combustion chamber, $OH^*$ is detected via a camera, which may be triggered by a pressure signal. This results in phase resolved average $OH^*$ images, which are integrated in the line of sight.

### Particle Image Velocimetry (PIV)

As described in Section (7.2.2).

### Gas and Temperature Analysis

Temperatures are measured at several locations on the chamber walls and at the entry of the chimney. For the considered adiabatic flame temperature of $T_{ad} = 1850\ K$, a chamber wall temperature of $T_{wall} \approx 1000\ K$ was measured. The gas temperature at the chimney entry was $T_{Chminey} \approx 1500\ K$.
In the chimney, $NO_X$ concentrations were measured and their values are given in Table (8.1). Note that these values are in $ppm - volume$ ($X^6_{NO}$) and corrected to 15% oxygen in the exhaust gases. A conversion formula is given by Lefebvre [49]:

$$X_{NO_X}@15\%X_{O_2} = \frac{5.9X_{NO_X}}{0.209 - X_{O_2}} \tag{8.1}$$

| Type | Location | Description | Staging | Pressure | $T_{ad}$ | $u_{ref}$ | Outlet |
|---|---|---|---|---|---|---|---|
| OH$^*$ | $z$-integrated | Phase-locked *OH* chemiluminescence measurements provided by DLR, Stuttgart. | $10\%, (30\%)$ | $506.5\ kPa$ | $1850\ K$ | $30\ m/s$ | Chimney<br>$T \approx 1500\ K$<br>$X_{NO_X} \approx$<br>$25\ ppmv@15\%O_2$<br>(for $\alpha_{st} = 10\%$) |
| PIV | $z = 0$ | Particle Image Velocimetry measurements provided by DLR, Stuttgart. | | | | | |
| RLN AD | any | Fully adiabatic, reactive LES, no effusion cooling. | 10% | | | | $\lvert R_r \rvert = 0$<br>$l_x = 0.5\ m$ |
| RLN | | Reactive LES including radiation, convective cooling and effusion cooling ("impingment" cooling and film cooling). | $10\%, (30\%)$ | | | | |
| RLR $0.xx$ | | Reactive LES based on RLN with a specified outlet reflection coefficient. | 10% | | | | $\lvert R_r \rvert = 0.xx$<br>$\arg(R_r) = -\pi$<br>$l_x = 0.8\ m$ |
| RLR relax | | LES based on RLN, with a partially reflecting outlet using the relax approach. | 10% | | | | $\alpha = 1500\ hz$<br>$l_x = 0.6\ m$ |

Table 8.1: Overview of all reacting cases.

#### Combustion Instability

In this study only the operating point $T_{ad} = 1850\ K$, $p = 506.5\ kPa$, $u_{ref} = 30\ m/s$ and $\alpha_{st} = 10\%$ will be presented. For these conditions, the experiment shows a pronounced combustion instability at **250 *hz***, which allows the acquisition of phase-triggered $OH^*$ images. These are presented in Figure (A.9). The major part of combustion takes place from $90^o$ to $270^o$ of the instability cycle. Close to $0^o$, the flame is nearly extinct. Unfortunately, the pressure signal is not available, so that the exact amplitude of the combustion instability cycle is unclear.

### 8.1.2 LES

The reactive simulations presented in this chapter are based on the non-reactive simulations of Chapter (7). To initiate combustion, a solution of a non-reacting case with the correct mass fluxes for the desired equivalence ratio is modified by changing the temperature in the chamber to match the corresponding adiabatic flame temperature. Then, the simulation is advanced in time until convergence of the mean quantities is reached.
The main differences between the reactive and non-reactive simulations are:

#### Combustion model

The same species and chemical reactions as used for the laminar flame simulations in Section (4.3) are included in the LES. Flame thickening is applied using the LOT approach presented in Section (5.3). The efficiency function, as outlined in Section (5.2.2) makes sure, that turbulence is properly accounted for in flame propagation. The inputs for the model are the laminar flame speed and flame thickness at the mean equivalence ratio. The model constant $\alpha_F$ is a function of the turbulence Reynolds number, which is determined by the $\text{TFLES}_2$ model [14]. Inputs are the integral turbulence length scale ($l_t = 2\ cm$), which is modified by a damping function when approaching the walls, and a constant ($\beta = 0.3$). The velocity fluctuation associated to the integral length scale is computed by the code using an appropriate operator.

#### Acoustics

The plenum inlet and chamber outlet are in reality quite complicated. Therefore, both are replaced by simpler geometries, which ensure a very similar flow and similar acoustics. The experimental chamber and the LES domain are compared in Figure (8.2).
The plenum inlet in the experiment is essentially non-reflecting and consists of a

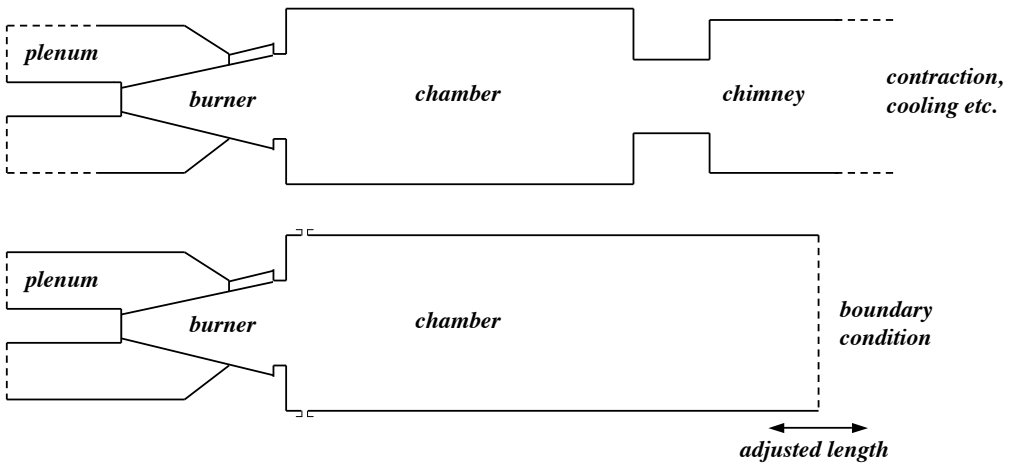


Figure 8.2: Schematic of the combustion geometries. Top: experimental setup; bottom: LES setup.

relatively large vessel with a sieve around the burner. For the LES it is replaced by a simple square duct, with a non-reflecting inlet (the relax boundary condition from Section (6.1.4)).
The lateral chamber walls are connected by a small periodic surface (left with right, top with bottom). This is done to make the walls acoustically slightly absorbing (as in reality) and avoids any un-physical, strong transverse combustion instability.
The whole experimental outlet geometry is replaced by a partially reflecting boundary condition as described in Section (6.1.4) in combination with an adjusted chamber length. This allows to impose various reflection coefficients for the chamber outlet, ranging from completely non-reflecting to partially and fully reflecting, in order to control the appearance of combustion instabilities as described in Section (6.2) and to match them in frequency and amplitude to the experimental observations.
In Table (8.1), the simulations with defined outlet reflection coefficient are referred to as RLR (for Reactive LES with Reflecting outlet boundary) and the ones with non-reflecting boundaries are referred to as RLN (for Reactive LES with Non-reflecting boundaries). Table (8.2) shows the acoustic properties of all boundaries for the RLN simulation. As for the non-reactive simulations, the length of the combustion chamber is not important in this situation. It is kept at $l_x = 0.5\ m$.

| Boundary | Mass flux | Pressure | Temperature | Species | Relax |
|---|---|---|---|---|---|
| Inlet plenum | 0.2622 $kg/s$ | - | 673 $K$ | air | 500 |
| Inlet lance | 0.0029 $kg/s$ | - | 673 $K$ | air | $10^4$ |
| Stage 1 | 0.0009 $kg/s$ | - | 293 $K$ | $CH_4$ | $10^4$ |
| Stage 2 | 0.0083 $kg/s$ | - | 293 $K$ | $CH_4$ | $10^4$ |
| Cooling front | 0.0164 $kg/s$ | - | 673 $K$ | air | $10^7$ |
| Cooling film | 0.0090 $kg/s$ | - | 453 $K$ | air | $10^7$ |
| Outlet | - | 506.5 $kPa$ | - | - | 150 |
| Walls plenum | No-slip isothermal at 673 $K$ | | | | |
| Walls burner | Wall-function isothermal at 673 $K$ | | | | |
| Wall frontplate | Wall-function isothermal at 700 $K$ | | | | |
| Other chamber walls | Wall-function isothermal at 1000 $K$ | | | | |

Table 8.2: Boundary conditions for the RLN case with $\alpha_{st} = 10\%$ and $\phi = 0.545$. The locations of the boundaries are shown in Figure (7.3).

### Operating condition

The adiabatic flame temperature for all simulations is $T_{ad} = 1850\ K$, corresponding to an equivalence ratio of $\phi = 0.545$. As in the experiment and the non-reactive simulations, the pressure is set to $p = 506.5\ kPa$ and the reference velocity is $u_{ref} = 30\ m/s$. The temperature of the inflowing air is 673 $K$ ($X_{O_2} = 0.21$, $X_{N_2} = 0.79$). The fuel is methane and injected at 293 $K$ ($X_{CH_4} = 1.00$). Only one staging ratio, $\alpha_{st} = 10\%$, will be presented here.

### Thermal properties

Table (8.2) summarises the thermodynamic properties for the RLN case. All walls are set to the appropriate temperatures to model convective cooling by wall-functions as described in Section (2.3). Radiation heat-losses are activated by using the model described in Section (4.3.3) and setting the temperature of the surroundings to $T_S = 1000\ K$. This model is considered as sufficient as the thermal thickness $\tau$ in this case is 0.5 [42].

### Timescales

The time-scales calculated in Section (7.2.1) for the non-reactive simulation have to be modified as the density and speed of sound change when passing from fresh to burnt gases. The speed of sound in the burnt gases is approximately 800 $m/s$ and the density is a third of the one in the fresh gases. Using a chamber of length

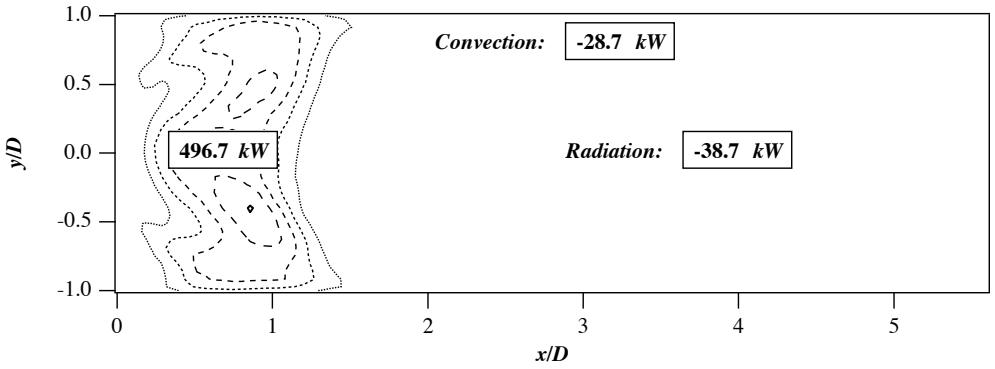


Figure 8.3: $z$-integrated view of the mean heat release for RLN (realistic cooling, anechoic outlet). Additionally, the combustion power and losses due radiation and convection are shown.

$l_x = 0.5\ m$, the acoustic time is then

$$\tau_{ac} \approx 1.5\ ms,$$

and the convective time

$$\tau_{cv} \approx 50\ ms.$$

This does not change anything for the total recording time ($T_{av} = 20\ ms$) and the recording frequency ($1/\Delta t_r = 1/0.05\ ms$).

## 8.2 Combustion in Anechoic Chamber

### 8.2.1 LES with Realistic Cooling (RLN)

The boundary conditions and models used for this simulation were described in the preceding section. The resulting simulation shows stable combustion without any dominant frequency in the pressure spectrum. This absence of combustion instability was expected, as the outlet boundary is acoustically non-reflecting. Nonetheless, this simulation is compared in the following to the experiment, which exhibits a combustion instability.
A snapshot of the simulation is shown in Figure (A.5). The geometry is cut open to allow the view on the flow. On the left, an iso-surface equivalence ratio ($\phi = 2.0$) is shown to visualise the fuel injections and on the right a heat release iso-surface is shown. It is coloured by the equivalence ratio. It is burning at various equivalence ratios and is basically stabilised by the CTRZ.

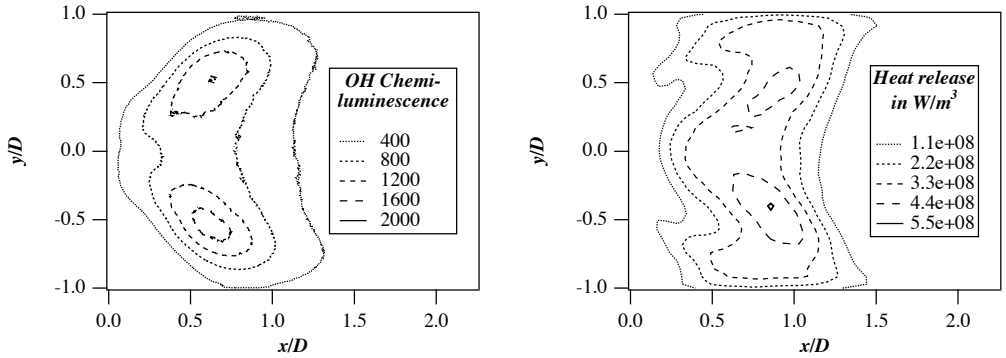


Figure 8.4: $z$-integrated views of the flame. Left: $OH^*$ from experiment; right: mean heat release from RLN.

Figure (8.3) shows an integrated view (in the $z$ direction) of the combustion chamber. The flame (on the left) is visualised via mean heat-release iso-contours. The flame has an overall power of 496.7 $kW$ and the gases in the chamber are loosing 67.3 $kW$ over a distance of 0.4 $m$, which corresponds to 13.6% of the total power. The losses are composed of 38.7 $kW$ due to radiation and 28.7 $kW$ due to convection at the cold walls. These losses are obtained by integrating Equation (4.36) over the whole domain and Equation (2.19) over all boundaries.
In Figure (8.4), the integrated view of mean heat-release from the LES is compared to $OH^*$ images from the experiment. Reasonable agreement is found, as both images show a flame that is principally anchored by the CTRZ. While the experiment suggests that no combustion at all takes place near the CRZ, the LES shows some activity at the entry ($x/D = 0.5$) of the CRZ.
Figure (8.5) shows cuts through the domain at $y = 0$. The field of mean temperature in the upper half shows the temperature rise due to the flame: the temperature in the CRZ is lower than in the centre of the chamber. Downstream, temperature is falling again due to radiation and convection heat losses. The thermal boundary layer can be seen close to the walls. At $x = 0.4m$, where the actual combustion chamber is connected to the chimney, the RLN case predicts a temperature of $\approx 1700\ K$. This is 200 $K$ above the temperature measured in the experiment (Table (8.1)). This difference is likely due to heat-transfer in the chimney and its connection to the chamber, which are not taken into account in the simulation.
In the lower half of Figure (8.5), a cut through the mean $NO$ mass fraction field at $y = 0$ is shown. $NO$ is mainly produced in the flame (prompt) and close to it (thermal). Thermal $NO$ production is quite rapidly stopped after combustion due to the heat losses. The value reached at $x = 0.4m$ ($Y_{NO} \approx 3.0 \cdot 10^{-6}$) corresponds to approximately 1.4 $ppmv$ corrected with Equation (8.1) to 15%$O_2$ in

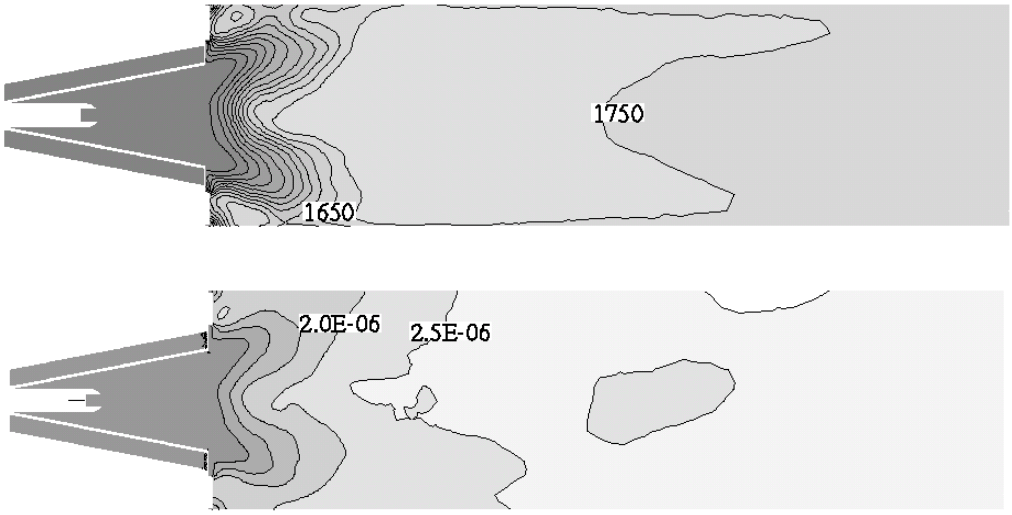


Figure 8.5: Cuts through the domain at $y = 0$ for RLN. Top: mean temperature; bottom: mean $NO$ mass fraction.

the burnt gases. Where the discrepancy with the measured value of Table (8.1) (25 $ppmv@15\%O_2$) comes from remains unclear.
Axial and radial mean velocities in the chamber as predicted by RLN match very well the measurements provided by DLR as seen in Figure (8.6). Axial velocity fluctuations are close as well, only the radial velocity fluctuations seem to be too strong in the regions of high radial shear. Discrepancies between simulation and experiment in this region were already noted in Figure (8.4) and probably point to a single problem, which was not yet identified[1].

### 8.2.2 Fully Adiabatic LES (RLN AD)

In order to understand the huge impact of the heat losses and air-cooling, a second simulation with anechoic outlet boundaries is carried out: RLN AD. In this simulation the radiation model is deactivated, the chamber walls are set to adiabatic and the air-cooling is diverted from the chamber to the plenum. All boundary conditions for this simulation are summarised in Table (8.3).
A snapshot of the resulting flow is presented in Figure (A.6). Comparing to the previous simulation (Figure (A.5)), the flame is now more compact and not only anchored by the CTRZ but also by the CRZ.
Figure (8.7) clearly shows for the mean flow what was already seen in the snap-

[1]The fluctuations obtained by Favre averages as presented in Section (1.5.2) were not any different from the ones obtained by the Reynolds averages used here.

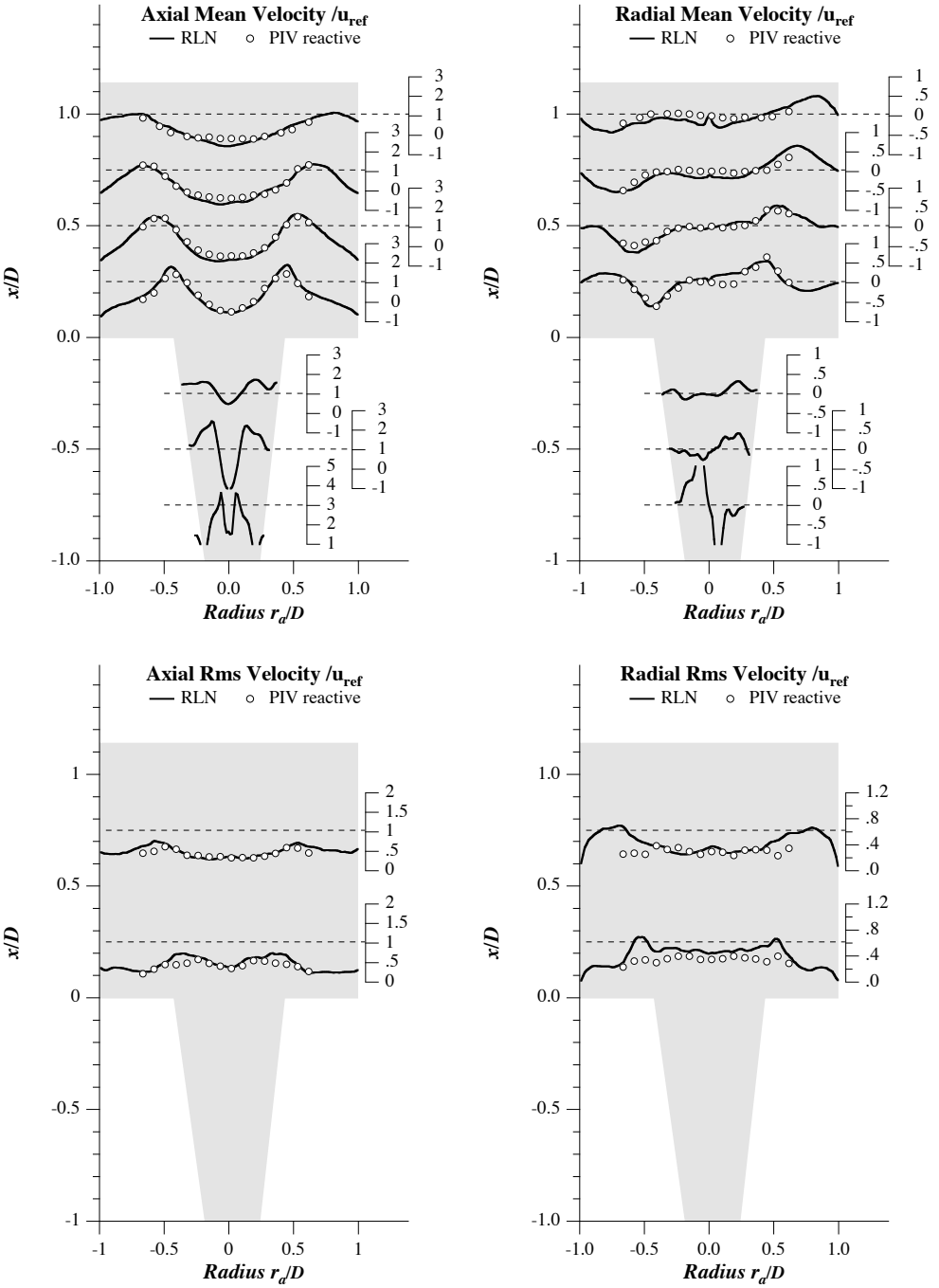


Figure 8.6: Comparison of the velocity fields provided by RLN and PIV ($z = 0$).

| Boundary | Mass flux | Pressure | Temperature | Species | Relax |
|---|---|---|---|---|---|
| Inlet plenum | 0.2876 $kg/s$ | - | 673 $K$ | air | 500 |
| Inlet lance | 0.0029 $kg/s$ | - | 673 $K$ | air | $10^4$ |
| Stage 1 | 0.0009 $kg/s$ | - | 293 $K$ | $CH_4$ | $10^4$ |
| Stage 2 | 0.0083 $kg/s$ | - | 293 $K$ | $CH_4$ | $10^4$ |
| Cooling front | 0.0000 $kg/s$ | - | 673 $K$ | air | $10^7$ |
| Cooling film | 0.0000 $kg/s$ | - | 453 $K$ | air | $10^7$ |
| Outlet | - | 506.5 $kPa$ | - | - | 150 |
| Walls plenum | No-slip isothermal at 673 $K$ | | | | |
| Walls burner | Wall-function isothermal at 673 $K$ | | | | |
| Other walls | Wall-function adiabatic | | | | |

Table 8.3: Boundary conditions for the RLN AD case with $\alpha_{st} = 10\%$ and $\phi = 0.545$.

shot: The flame is now stabilised not only by the CTRZ but also the CRZ and it is also more compact. Comparing to the $OH^*$ images from experiment show that this does not correspond to reality. The flame is normally not anchored by the CRZ. This error is mostly attributed to the lack of cooling air at the burner exit for RLN AD, but certainly the absence of radiative and convective cooling has its influence, too.

Cuts through the mean temperature and mean $NO$ mass fraction field are shown in Figure (8.8). In the combustion chamber, the adiabatic flame temperature ($T_{ad} = 1850K$) is reached and the products do not cool down before reaching the chamber exit. Also the CRZ is now filled with hot gases whose temperature is close to the adiabatic flame temperature. The predicted $NO$ mass fraction at the virtual chamber exit ($x = 0.4m$) is now $29.4 \cdot 10^{-6}$. This corresponds to 13.8 $ppmv@15\%O_2$. This high value is mainly due to the thermal $NO$ production which is not stopped by thermal losses. Close to the flame, a slight increase of prompt $NO$ is observed, too. The value at the chamber exit is still lower than the measured value in Table (8.1) despite the strong increase.

Figure (8.9) shows comparisons of the velocity fields obtained by simulation and experiment. The radial mean velocity matches well with experiment but its fluctuations exhibit the same over-prediction in the region of high radial shear as in the RLN case. The axial mean velocity matches not as well as in the RLN case and its fluctuations are also slightly over-predicted.

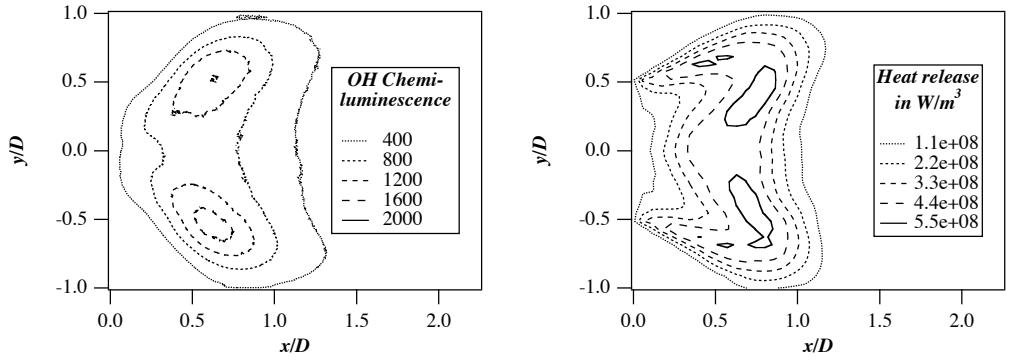


Figure 8.7: $z$-integrated views of the flame. Left: $OH^*$ from experiment; right: mean heat release from RLN AD.

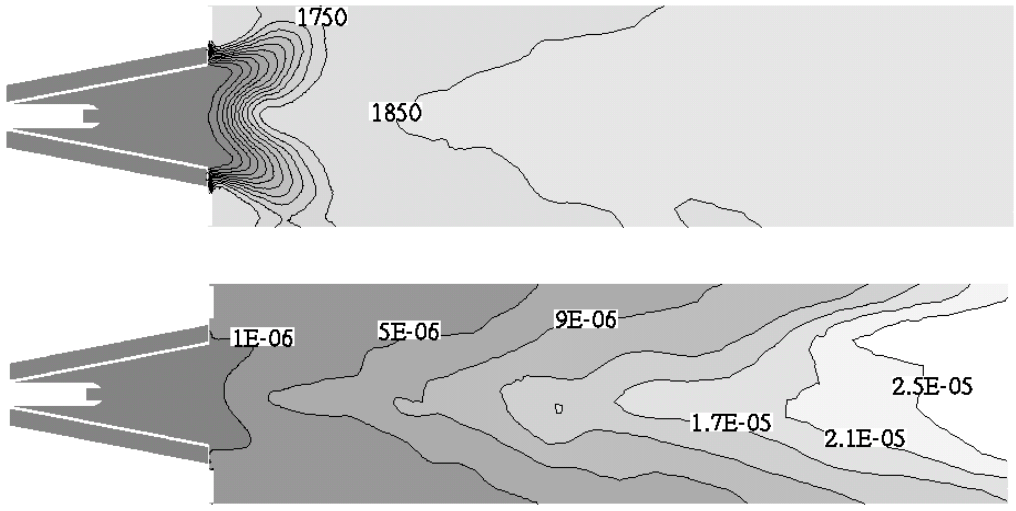


Figure 8.8: Cuts through the domain at $y = 0$ for RLN AD. Top: mean temperature; bottom: mean $NO$ mass fraction.

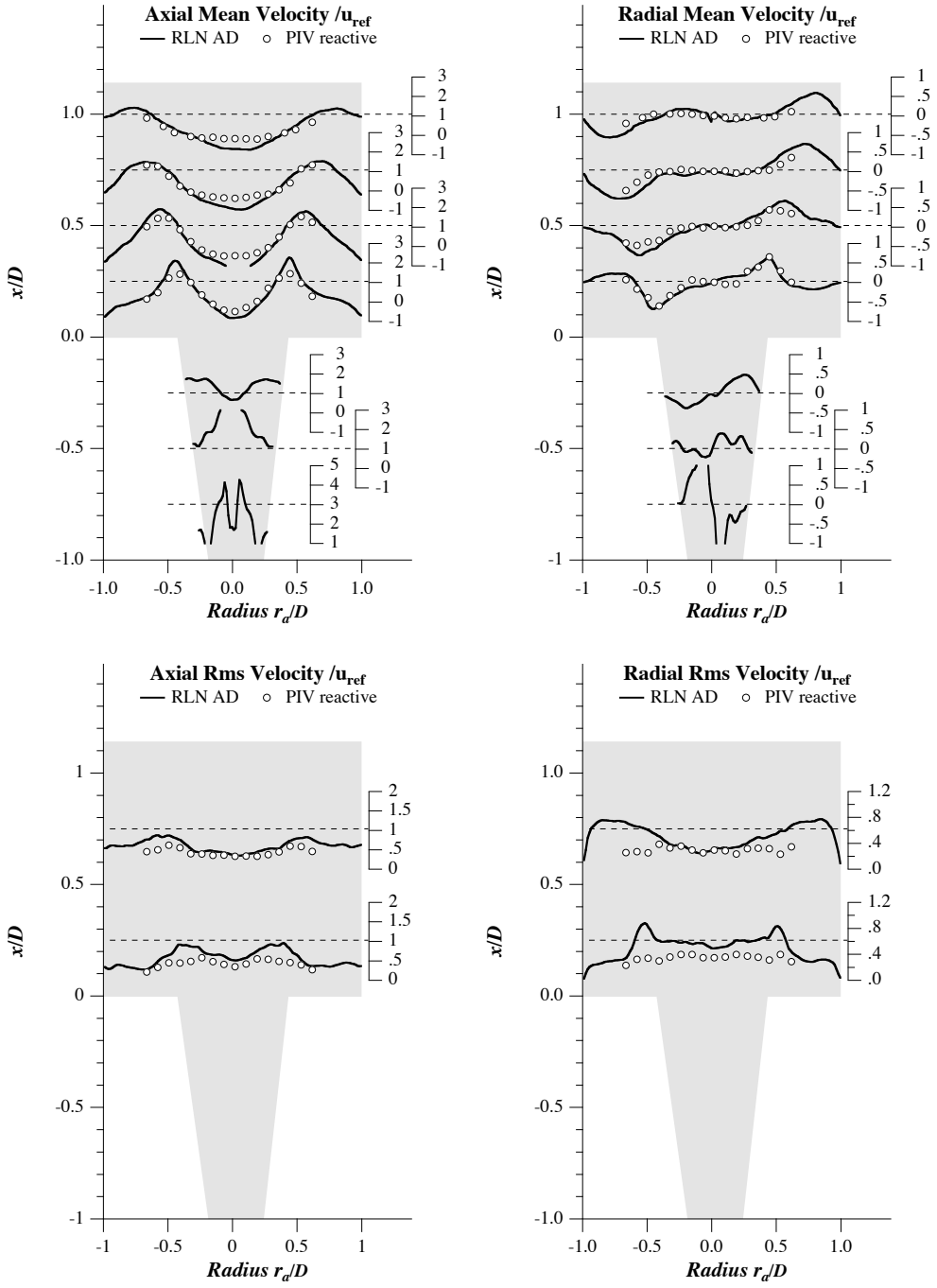


Figure 8.9: Comparison of the velocity fields provided by RLN AD and PIV ($z = 0$).

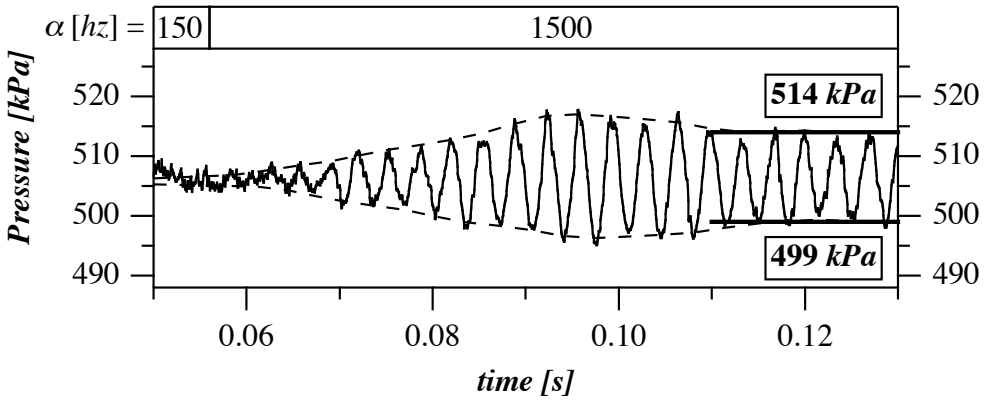


Figure 8.10: Pressure trace at $x = 0.07\ m$ ($y = z = 0$). The outlet boundary condition relax is changed from 150 *hz* to 1500 *hz*. A combustion instability develops and reaches a limit cycle (RLR relax).

## 8.3 Combustion with partially reflecting outlet

The level of combustion instability depends on the outlet condition and changes the mean flow field. Unfortunately, the amplitudes depend on the outlet reflection coefficient, which is unknown in the experiment. In this section it is shown how LES is used to circumvent this difficulty.

### 8.3.1 The Appropriate Boundary Condition

In order to match the oscillation level observed in the experiment, the outlet boundary condition must be adjusted in the LES. A first approach is to impose a higher relax ($\alpha$) at the outlet boundary. It is changed from 150 *hz* to 1500 *hz*. A pressure trace at $x = 0.07\ m$ ($y = z = 0$) from the resulting simulation is shown in Figure (8.10). It is seen how pressure oscillations grow at a frequency of $\boldsymbol{f = 288\ hz}$ and reach a limit cycle from $t = 0.11\ s$ on. The overshoot observed before the limit cycle is a known phenomenon also observed in experiments [67] and other LES [58]. This simulation is referred to as RLR relax.
The frequency (close to the 250 *hz* from experiment) was obtained by using an empirically adjusted chamber length of $l_x = 0.6\ m$. From Equation (6.18), the reflection coefficient at this frequency is determined as $R_r = 0.38\ \mathrm{e}^{-i\,0.63\pi}$ (for $f = 288\ hz$ and $\alpha = 1500\ hz$).
For frequencies, different from $f = 288\ hz$, the reflection coefficient imposed by Equation (6.18) is different. This dependency of frequency and the coupling

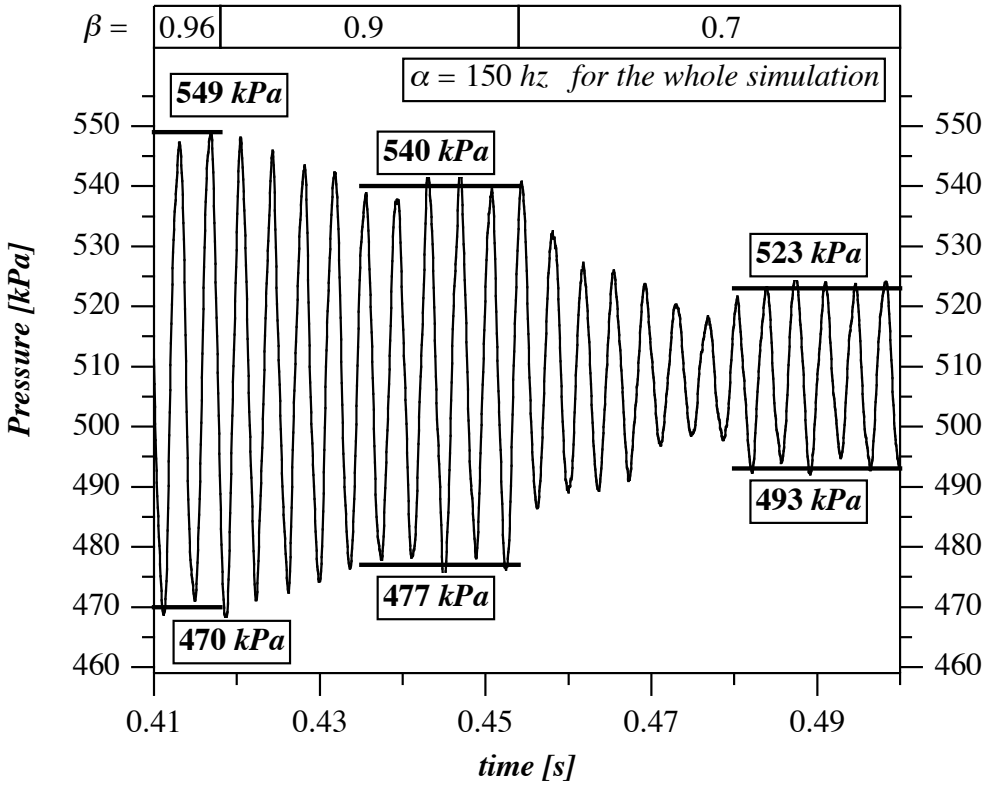


Figure 8.11: Pressure trace at $x = 0.07\ m$ ($y = z = 0$). The outlet boundary condition relax is $\alpha = 150\ hz$ and the reflection parameter $\beta$ is adjusted in order to adjust the amplitude of the limit cycle (RLR 0.*xx*).

of modulus and phase angle make it difficult to describe the acoustics with this boundary condition. Because of that, the following simulations are carried out with the boundary condition corresponding to Equation (6.19) which imposes a fixed reflection coefficient $|R_r| = \beta$ for a wide frequency range. The pressure relax ($\alpha$) is kept low and a fraction ($\beta$) of the outgoing wave is added to the incoming wave. The phase angle is fixed to $-\pi$ in the important frequency range, so the chamber length has to be adjusted only once for all simulations.
Figure (8.11) presents a pressure trace at $x = 0.07\ m$ ($y = z = 0$) from a simulation using the described boundary condition ($\alpha = 150\ hz$, $\beta$ variable). It shows a limit cycle with $\beta = 0.96$, a period where the simulation is adjusting to $\beta = 0.9$, a new limit cycle at $\beta = 0.9$ and finally the adjustment and limit cycle for $\beta = 0.7$. During the whole simulation the frequency of the instability is $\boldsymbol{f = 266\ hz}$. This frequency was obtained by setting the chamber length $l_x$ to $0.8\ m$. This simulation permits to compare different levels of pulsations to the experiment and determine approximately the appropriate reflection coefficient. These simulations are referred to as RLR $0.xx$ (the last two digits signal the modulus of the outlet reflection coefficient).

### 8.3.2 Instability with $p_{rms}/\overline{p} \approx 5.0\%$ (RLR 0.96)

The outlet boundary in this simulation is set to extremely reflecting and a very strong combustion instability develops. Looking at the integrated mean heat release in Figure (8.12) reveals, that the strong pressure fluctuations in this simulation produce a flame that is far less compact and it is pushed away from the centre, burning principally close to the walls. This does not very well match the experimental observations and is a first indication, that the outlet reflection coefficient of $|R_r| = 0.96$ is too high.
Figure (A.10) shows phase averaged images of the integrated heat release that are to be compared with Figure (A.9). Globally, the same instability cycle as in experiment is observed. But as in the mean image in Figure (8.12), compared to experiment, the flame is always stabilised closer to the wall and more downstream.

The comparison of the velocity measurements in Figure (8.13) shows that the instability produces very strong velocity fluctuations close to the burner exit. These make it difficult for the flame to stabilise in the same region as for stable combustion. This is not at all seen in the experiment and confirm that the outlet reflection coefficient is too high. Nonetheless, this simulation serves as a basis for explaining the combustion instability, because the high amplitudes make it easier to identify the main instability mechanism.
The mass fluxes through all boundaries are seen in Figure (8.14). The average mass fluxes match the specifications of Table (8.2). The outlet and inlet bound-

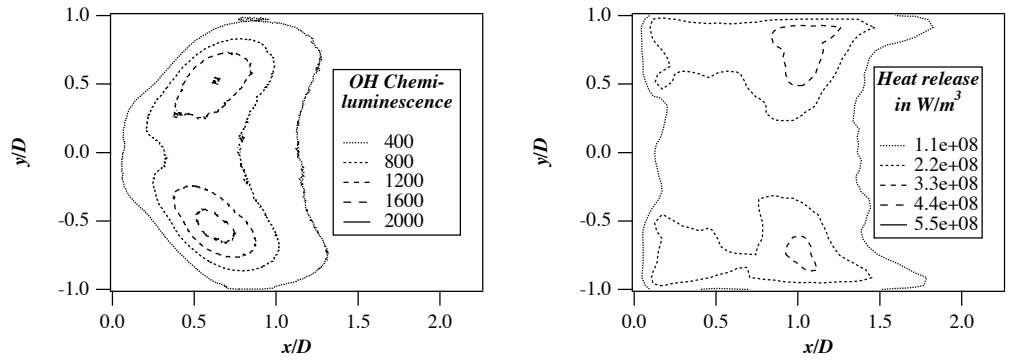


Figure 8.12: $z$-integrated views of the flame. Left: $OH^*$ from experiment; right: mean heat release from RLR 0.96.

aries are strongly influenced by the instability. The chamber outlet suffers reverse flow during a small amount of time every cycle and the inlet of the plenum passes every cycle through a state where no more air is entering the plenum. All other inlets are specified as acoustically reflecting and their mass fluxes are only slightly modulated by the instability. Consequently, the fluctuation of air mass flow combined with a constant inflow of fuel will produce periodic mixture fraction fluctuations, which are convected from the burner to the chamber. In the following, their impact on the instability is analysed by a closer look at the flow field.
Figures (8.15) to (8.18) present a one-dimensional view of the whole domain. They are a result of phase averaging the instability and integrating the flow in the $y-$ and $z-$directions. All four figures show the local pressure, heat release, fuel concentration and global mass flux. The mean values are always included and each figure shows the flow at two (opposite) phase angles. Following one cycle of the instability allows to understand the instability mechanism:

**Pressure - mass flux:** The mean pressure curve shows the pressure loss through the burner, the mean mass flux how mass is conserved. The pressure fluctuations show that the eigenmode is a $\lambda/4$-mode in the chamber. The mass flux is in accordance with the pressure field: a velocity node is found close to the burner exit and an anti-node is found at the chamber exit.

**Pressure - heat release:** Heat release is maximum for high pressures close to the flame, and minimum for low pressures (Figures (8.15) and (8.16)). As expected, the combustion is still driving the pressure fluctuations.

**Heat release - fuel:** The heat release fluctuations are explained by looking at the local fuel concentrations. From $45^o$ (Figure (8.16)) to $135^o$ (Figure (8.18)),

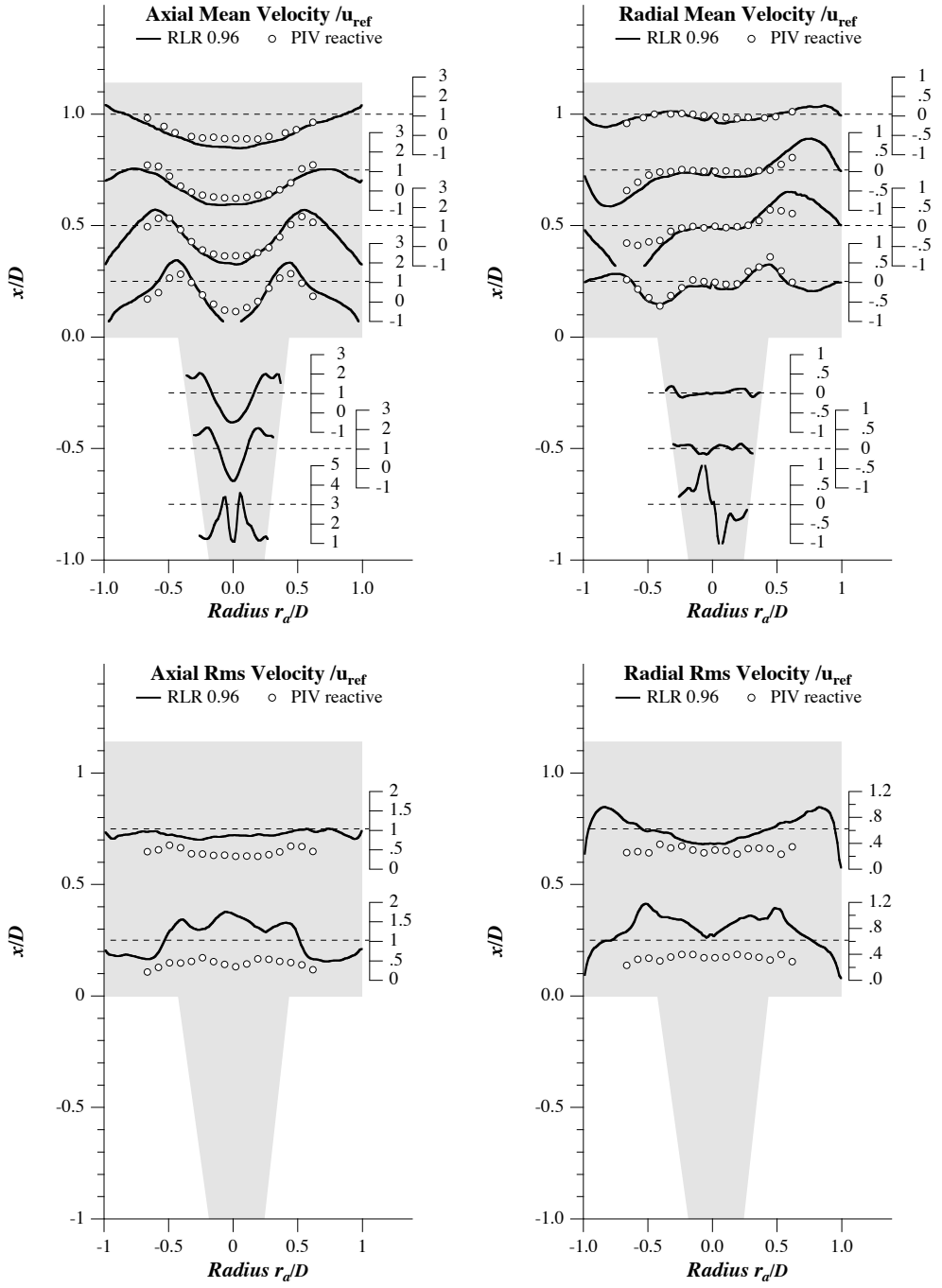


Figure 8.13: Comparison of the velocity fields provided by RLR 0.96 and PIV ($z = 0$).

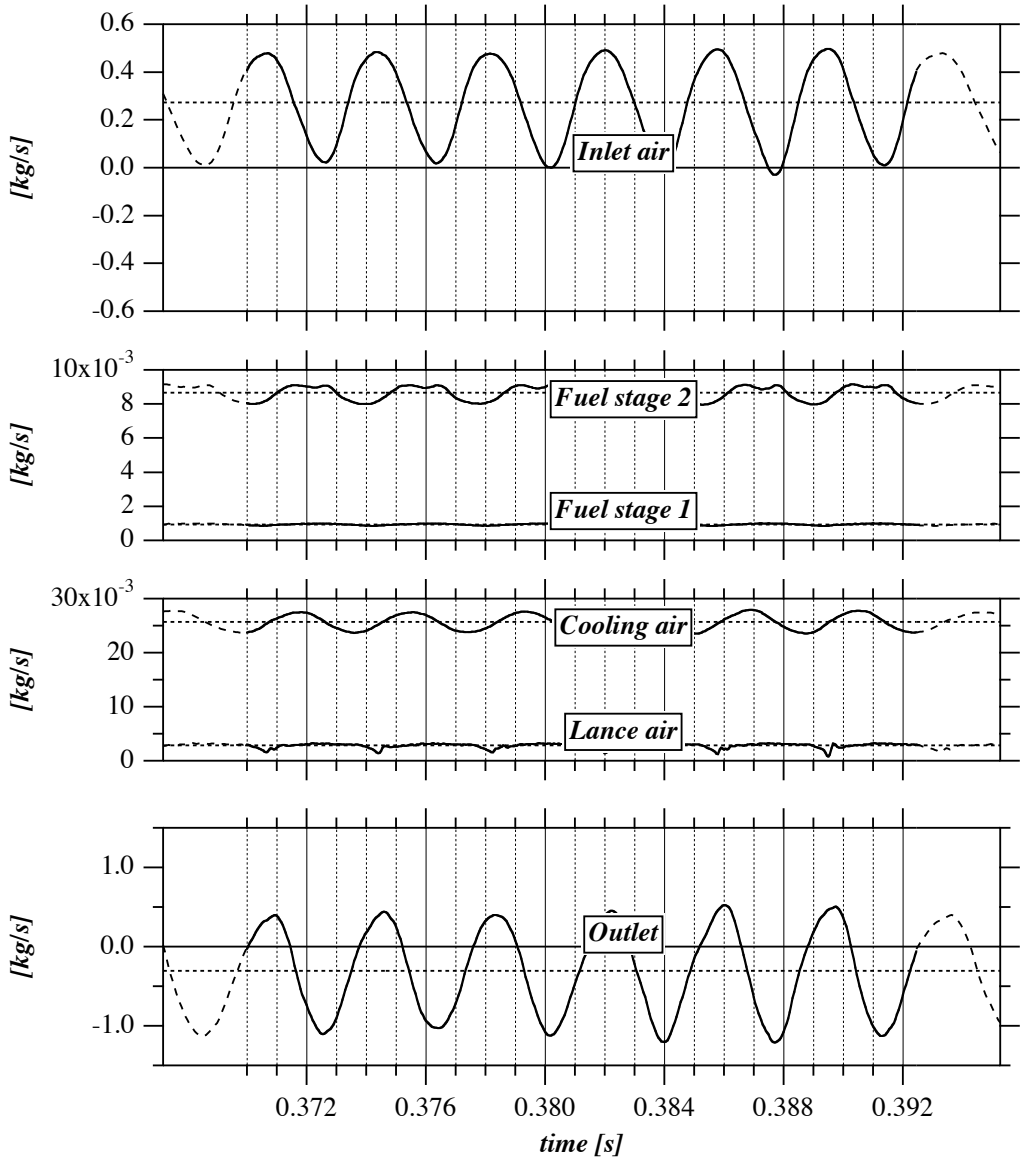


Figure 8.14: Instantaneous (solid lines) and mean (dashed lines) mass fluxes through all boundaries for the RLR 0.96 case.

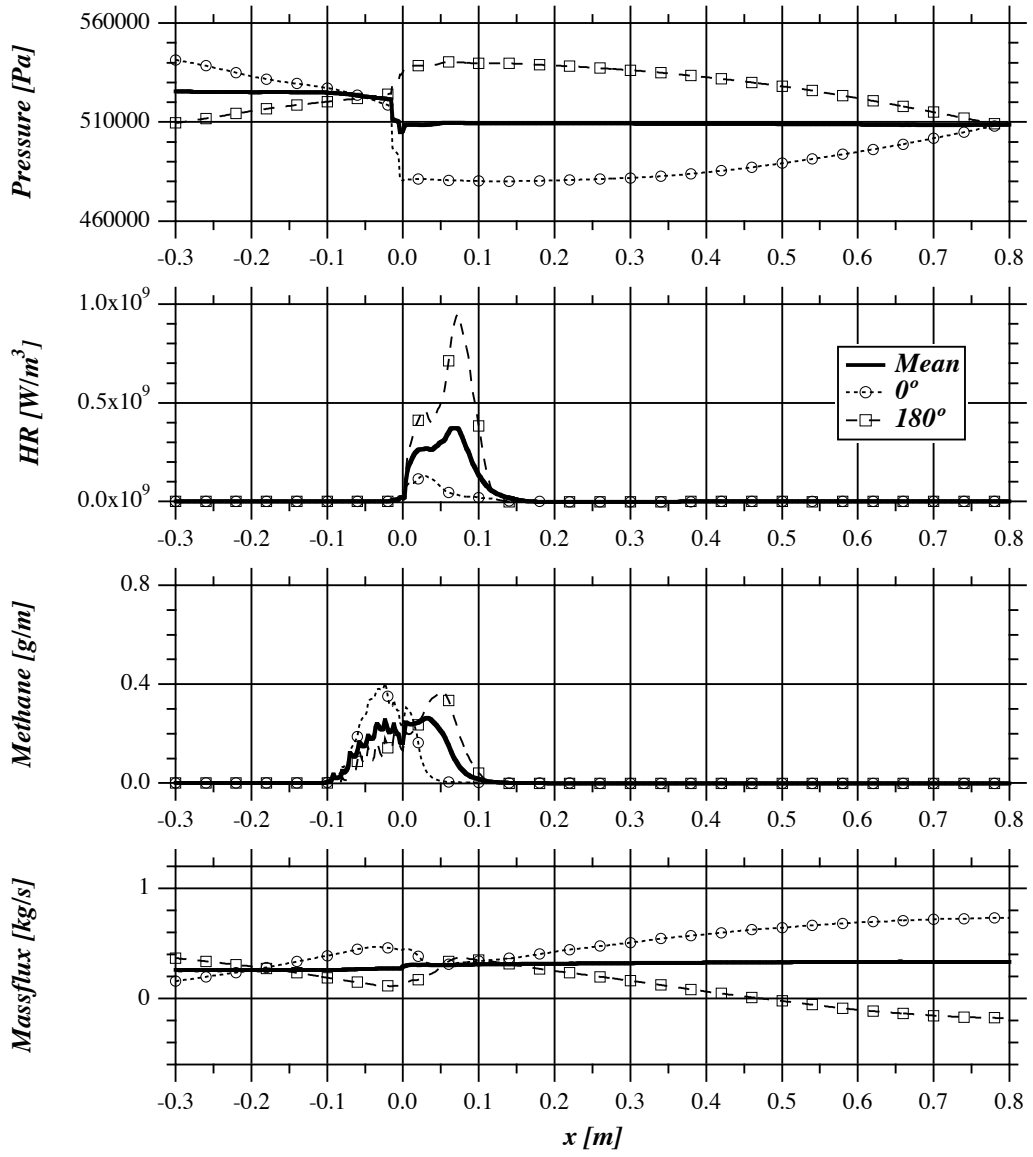


Figure 8.15: One-dimensional view of the whole domain during the RLR 0.96 limit cycle at phase angles of 0° and 180°.

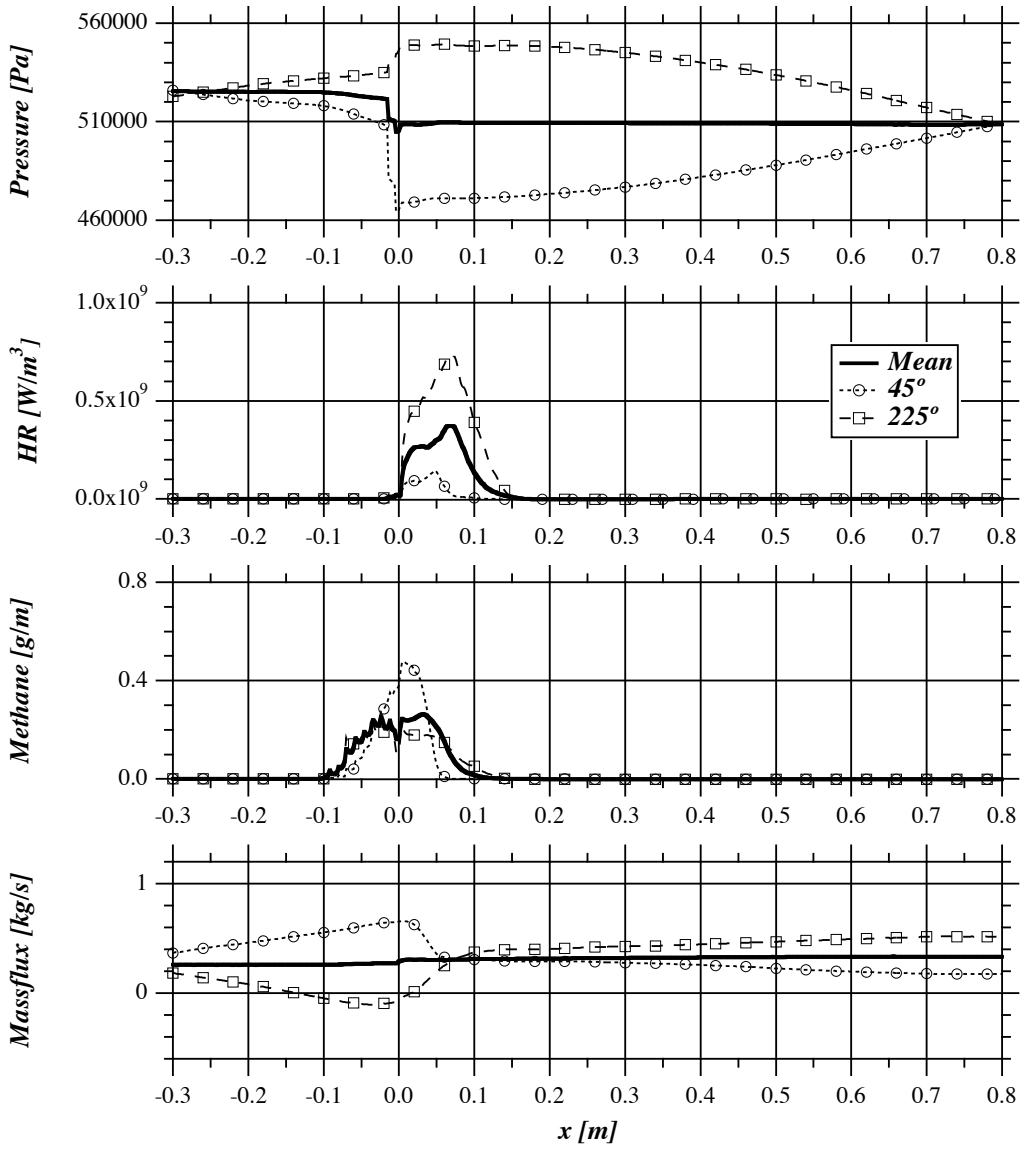


Figure 8.16: One-dimensional view of the whole domain during the RLR 0.96 limit cycle at phase angles of 45$^o$ and 225$^o$.

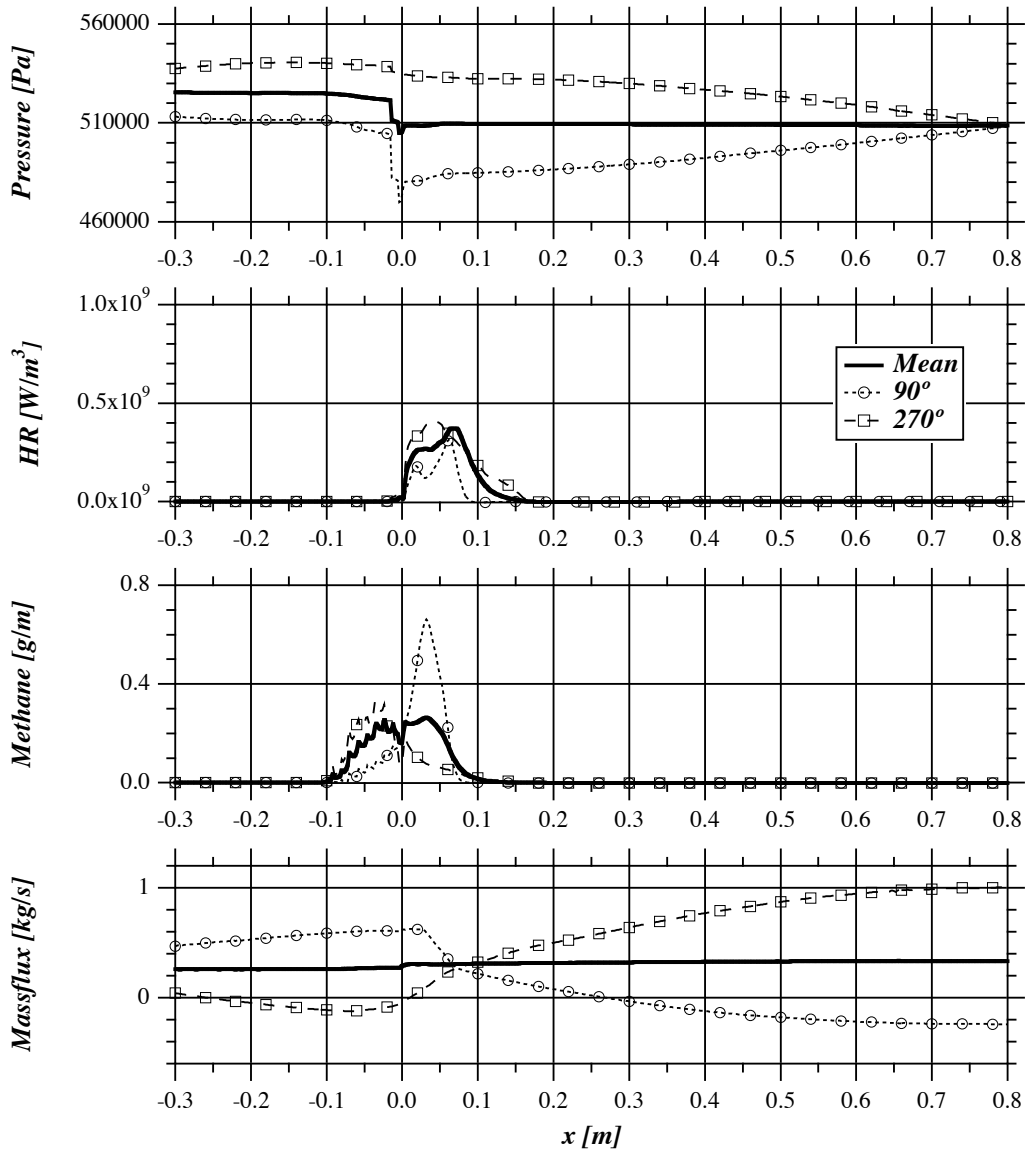


Figure 8.17: One-dimensional view of the whole domain during the RLR 0.96 limit cycle at phase angles of 90º and 270º.

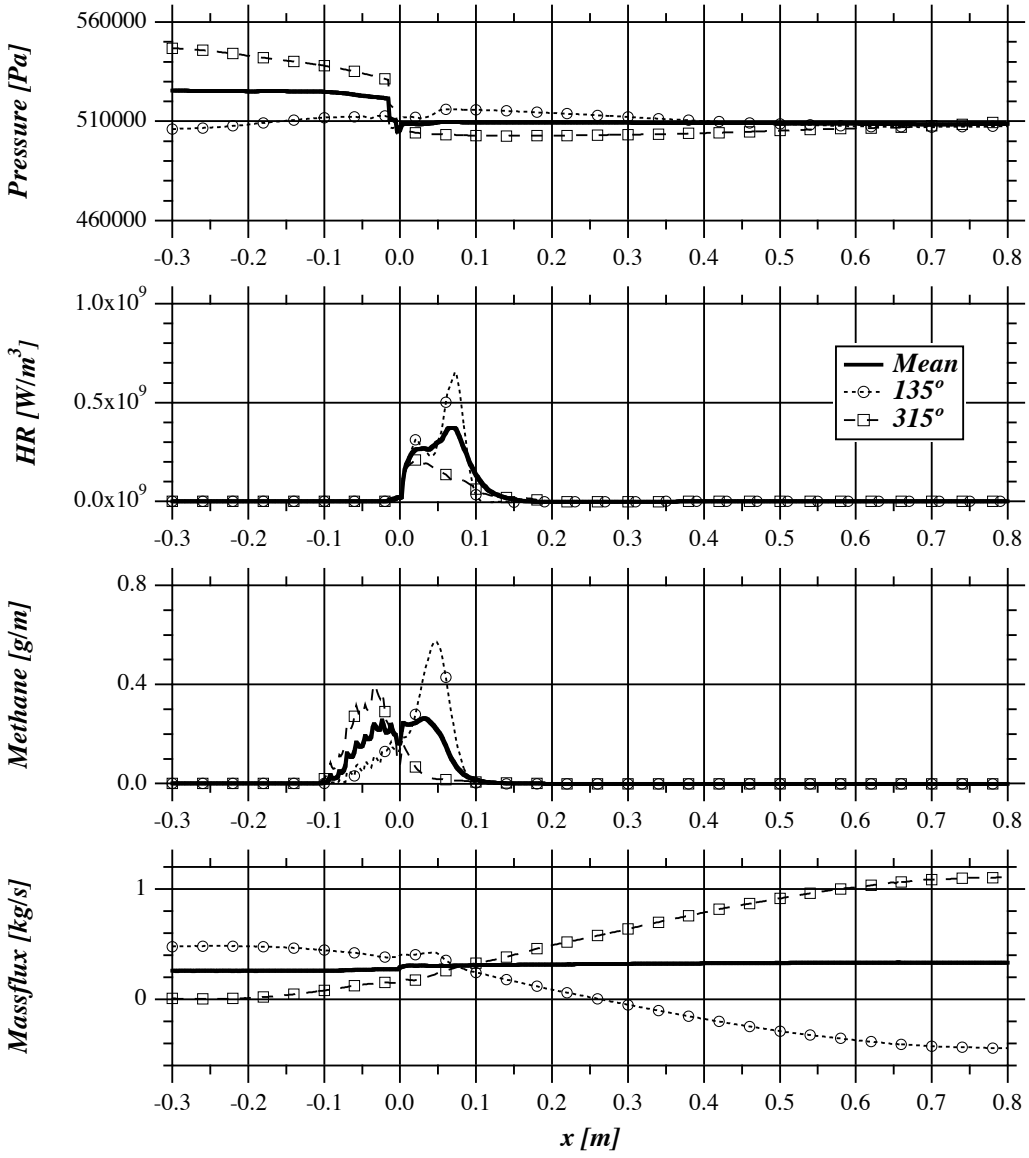


Figure 8.18: One-dimensional view of the whole domain during the RLR 0.96 limit cycle at phase angles of 135º and 315º.

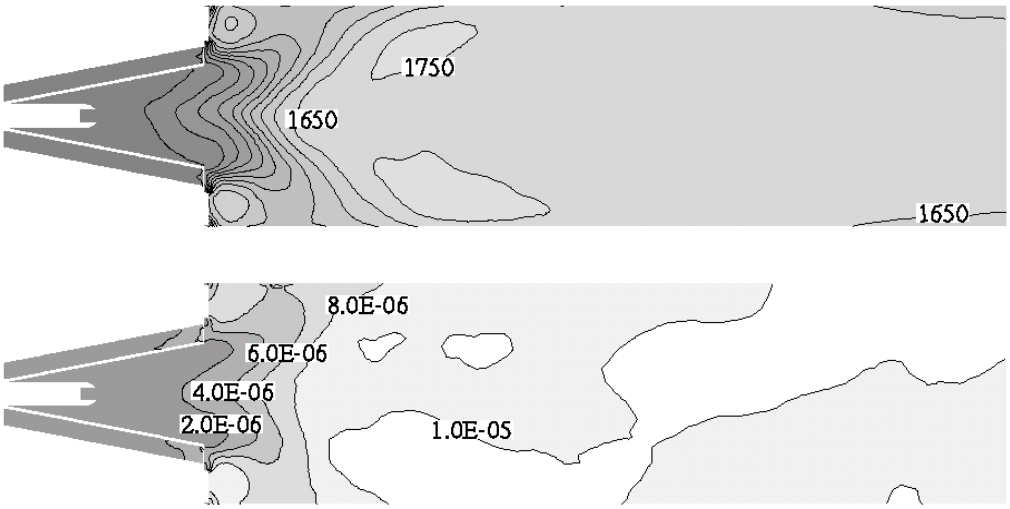


Figure 8.19: Cuts through the domain at $y = 0$ for RLR. Top: mean temperature; bottom: mean *NO* mass fraction.

a high fuel concentration is convected from the burner into the chamber. This pocket burns at $180^o$ (Figure (8.15)).

**Fuel - massflux:** This fuel pocket causing the strong heat release is formed close to the fuel injections ($x = -0.05\ m$), where the concentration is steadily rising from $225^o$ (Figure (8.16)) to $0^o$ (Figure (8.15)). This happens because of the low air flow during this period as verified by the mass flux graph.

This mechanism is very effective in closing the instability loop, since the time it takes for the fuel to be convected into the chamber corresponds approximately to half a period of the quarter wave mode. This process becomes even clearer when looking at snapshots of the simulation during one cycle. These are presented in Figures (A.7) and (A.8). At $0^o$, the fuel has accumulated close to the injections, is convected through the burner at $90^o$, reaches the chamber and burns at $180^o$ and finally starts to accumulate again at $270^o$.
Even though this instability is known to be too strong compared to reality, it is interesting to look at the temperature and *NO* fields in Figure (8.19). The temperature field reflects the change in flame position and also shows that the temperature change is now spread over a greater region compared to the stable case (Figure (8.5)). After combustion, approximately the same temperature levels are reached in the chamber. The *NO* field shows considerable differences compared to the stable case. The amount of *NO* produced is multiplied by a factor of 4 for the unstable case. This is due to the flame burning at higher equivalence ratios

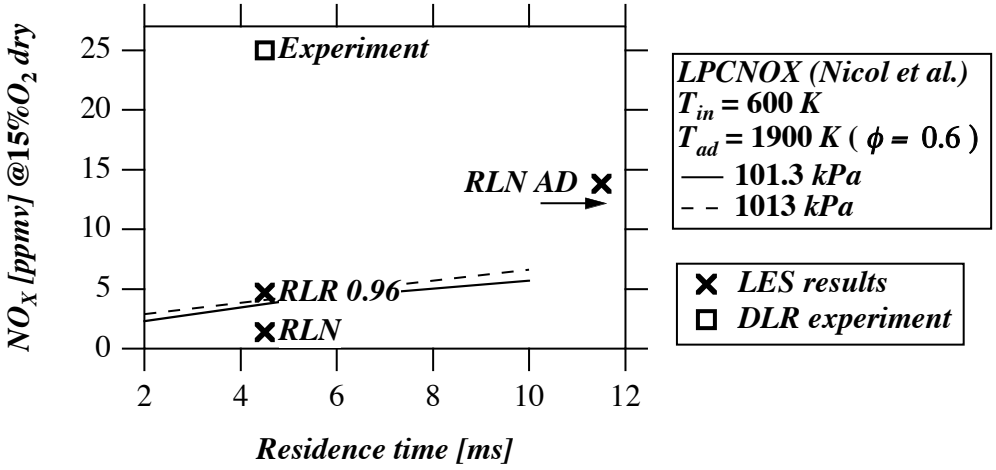


Figure 8.20: Nitrous oxide emissions from experiment, simulation and one-dimensional model [68].

during a certain time in the instability cycle. Because of the exponential relationship between $NO$ formation and equivalence ratio (and temperature), a perturbation of the equivalence ratio (while keeping the temporal mean value constant) will invariably augment $NO$ production [27]. At the virtual chamber exit, an $NO$ mass-fraction of $10.0 \cdot 10^{-6}$ is measured. This corresponds to 4.7 $ppmv@15\%O_2$, while the stable situation yields 1.4 $ppmv@15\%O_2$.
The $NO$ prediction for the instable simulation is still considerably lower than the experimental value. This is summarised in Figure (8.20), where also the RLN and RLN AD simulations are indicated. They are compared to the results of one-dimensional simulations of Nicol et al. [68], where similar thermodynamic conditions were used. These simulations, including the full nitrous oxide chemistry are dependent on the residence time in the high temperature zone close to the flame. Assuming that for the ev7is, this region is 0.1m long, the residence time is approximately 4.5 ms. Therefore, the data should be comparable. The two physically reasonable simulations (RLN and RLN 0.96) exhibit $NO$-levels that compare well to Nicol's results. The experimental data however differs up to a factor of 5 from Nicol's model. This suggests that the experimental data is erroneous but this has not been checked yet.

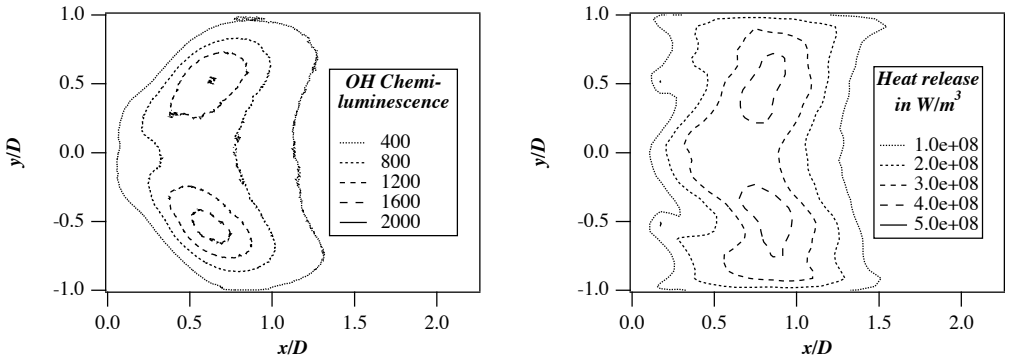


Figure 8.21: $z$-integrated views of the flame. Left: $OH^*$ from experiment; right: mean heat release from RLR 0.70.

### 8.3.3 Instability with $p_{rms}/\overline{p} \approx 2.0\%$ (RLR 0.70)

As seen in Figure (8.11), by setting the outlet reflection coefficient to 0.70, a limit cycle with a considerably lower pressure amplitude is obtained. Comparing the integrated mean heat release with experiment in Figure (8.21) reveals that the mean flame position and shape is now better predicted and relatively close to the stable simulation. The heat release is slightly more distributed and the maximum is slightly pushed to the walls. Still the presence of heat release in the CRZ is the main difference when comparing to the experiment.
The velocity measurements in Figure (8.22) compare better to the experiment now, but the axial velocity fluctuations are still slightly too high. This suggests that the outlet reflection coefficient in the experiment is even lower. These results, approaching the RLN case prove that the instability in the experiment expresses itself in a fluctuation of the heat release around the state of the corresponding stable situation (which would occur if the experimental chamber was anechoic).
Looking at snapshots of the simulation (not shown here), it is found that the mechanism of equivalence ratio fluctuations closing the loop for combustion instability is still present. $NO$ emissions[2] are in between RLN and RLR 0.96.

[2]The exact data is not available, since no full convective time-scale was simulated yet.

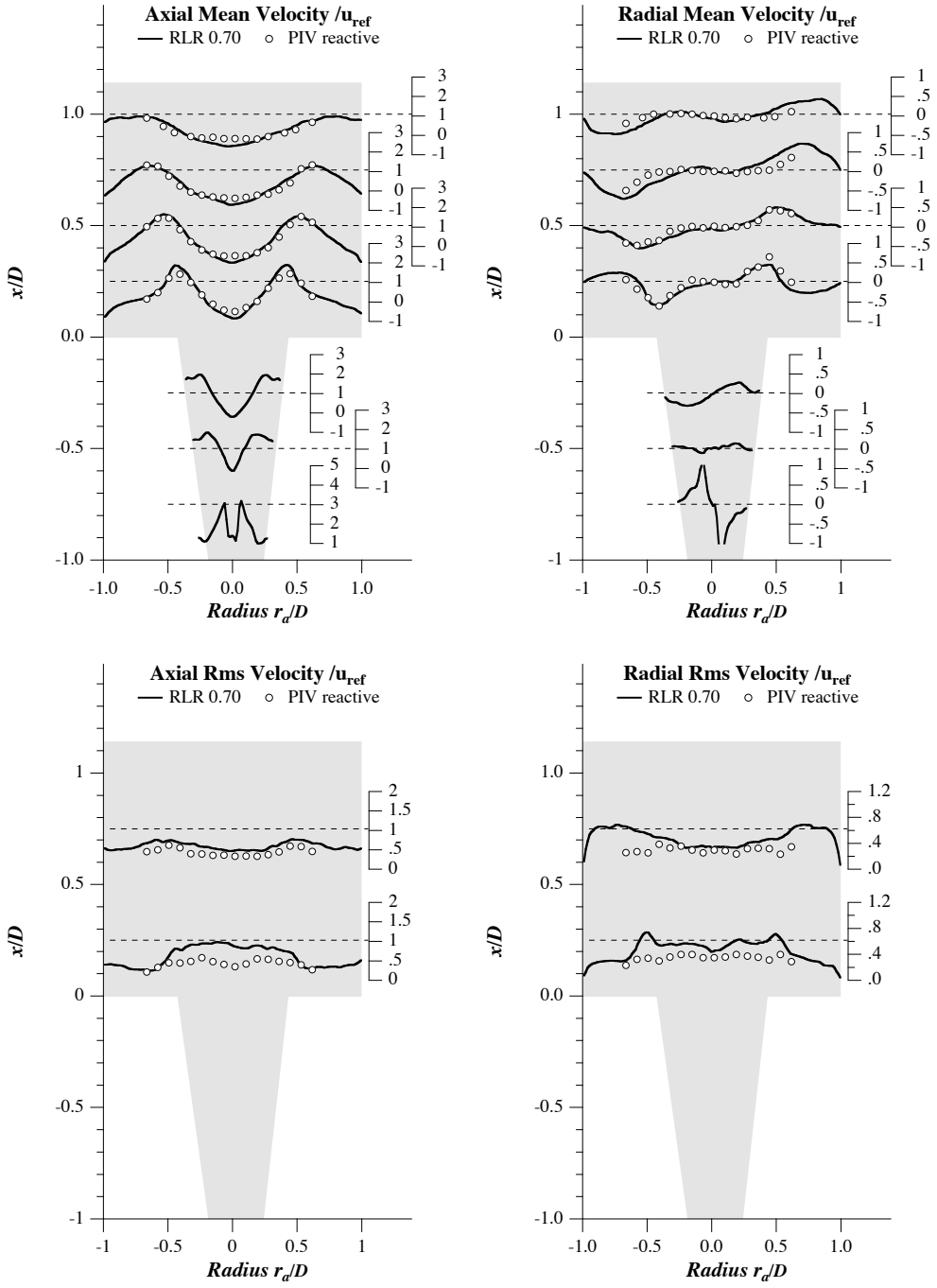


Figure 8.22: Comparison of the velocity fields provided by RLR 0.70 and PIV ($z = 0$).

# Conclusion

This work tackles several aspects influencing nitrous oxide formation in gas turbine combustion as laid out in Figure (2) in the introduction. Appropriate models for these are developed, implemented and verified:

**Wall functions:** The classical wall function approach, used in a similar way as in RANS simulations works well in LES of turbulent channel flow. It improves the predictive capabilities of LES with under resolved boundary layers. This is essential for the prediction of heat fluxes at the boundary. For flows that are not dominated by the dynamic behaviour of the boundary layer (like the ones treated in this work), this approach is completely sufficient.

**Radiation:** Radiation is as important as convective heat transfer and a simple "optically thin" model is used as a first step to include radiation in LES of gas turbine combustion. It is based on local gas composition, assuming homogeneous surroundings and no re-absorption. It is considered as sufficient for the present application. A possible extension would be the calculation of view factors while still neglecting re-absorption. Also a coupling with the wall temperatures might be a valuable extension.

**Reduced scheme for *NO*:** The prediction of $NO$ production is achieved by manually fitting the $NO$ reaction rates to the complete mechanism (GRI-Mech 3.0). $NO$ is well reproduced by laminar flames and if necessary, the reaction can easily be fitted to other mechanisms than the GRI-Mech 3.0.

The models, as discussed above are used for LES simulations of a lean partially premixed burner, where several aspects are studied:

**Velocity fields of the non-reactive simulations:** Comparison of experimental data with the LES shows the good predictive capabilities of non-reactive LES achieved today. It is also shown, that no turbulent inflow is necessary to obtain good results in such a configuration.

**Mixing:** Mixing of the fuel and air is explicitly included in this study by computing the flow in the $CH_4$ injection holes. At a certain distance from the

injections, good results are obtained. The limiting factor for the mixing prediction close to the injections proves to be the mesh resolution, which must be augmented if this region is of interest.

**Flame stabilisation:** The reactive simulations show a relatively good agreement in flame shape, if the air cooling at the burner exit is included. Generally, the flame seems less compact compared to the experimental data. Either this is due to the not perfect correspondence of $OH^*$ (experiment) to heat release (simulation) or because of the present combustion model not being perfectly suited for the case.

**Thermal losses:** Including thermal losses through radiation and convective cooling is essential to decrease chamber temperature and stop thermal $NO$ production. In the present case, these models cause a difference of one order of magnitude in $NO$ concentration at the chamber exit.

**Combustion instability:** By imposing the appropriate exit boundary condition, a combustion instability as observed in experiment was captured. It is shown that the main mechanism closing the instability loop stems from equivalence ratio fluctuations. For an instable simulation the $NO$ emissions are augmented by up to 75%.

In summary, this work shows the effect of numerical models and physical parameters on the process of $NO$ formation in LES of gas turbine combustion. The obtained emission levels are comparable to those found in literature. This adds new predictive capabilities to LES that were still out of reach several years ago and that will help to increase the use of unsteady CFD in industry.

# Appendix A

# Colour Plates

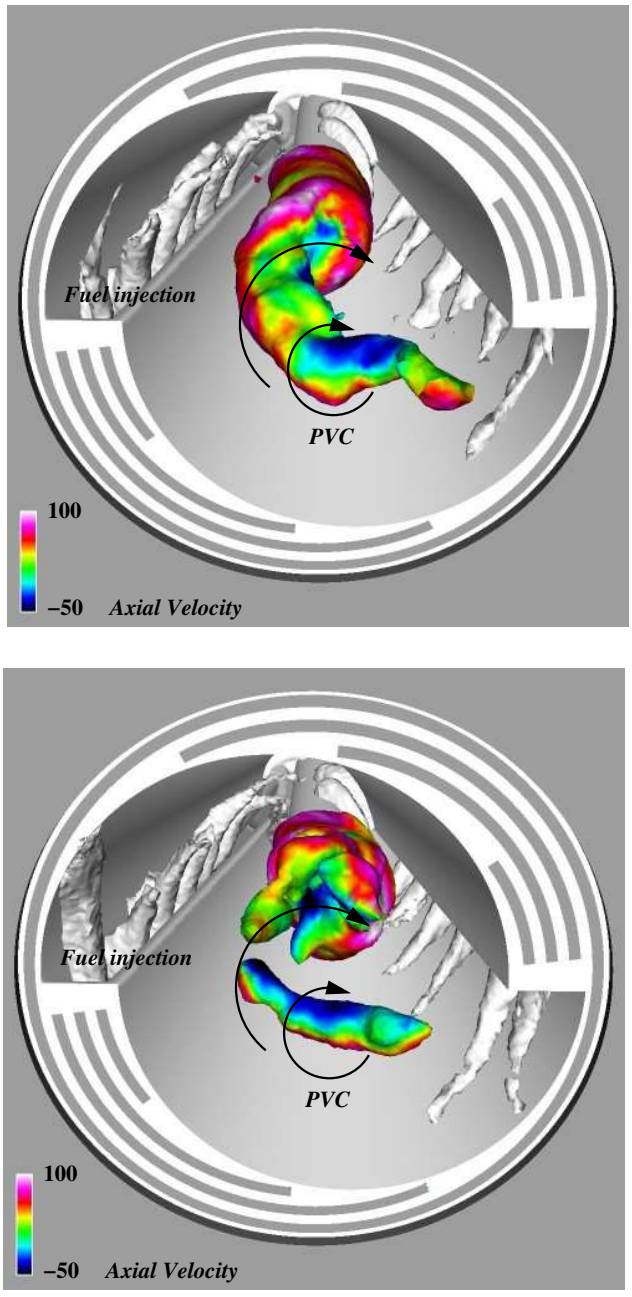


Figure A.1: View from the combustion chamber on the burner. The PVC is visualised by pressure iso-surfaces coloured by axial velocity. Top: LES I; bottom: LES II. Swirl and PVC rotation is illustrated by arrows. Additionally the fuel injections are visualised by mixture fraction iso-surfaces (Section (7.3)).

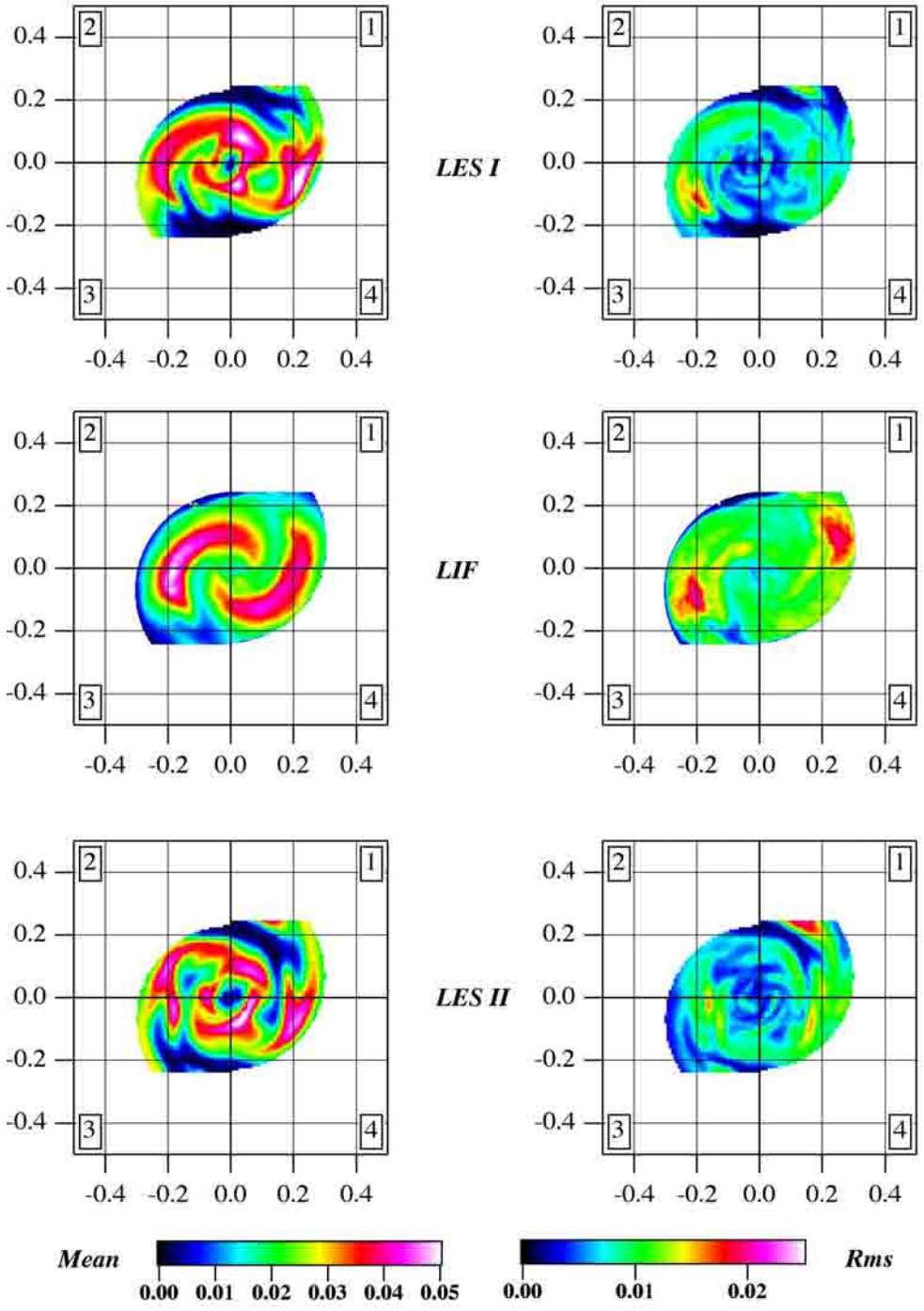


Figure A.2: Comparison of LES and Experiment at $x/D = -0.66$ (Section (7.5)).

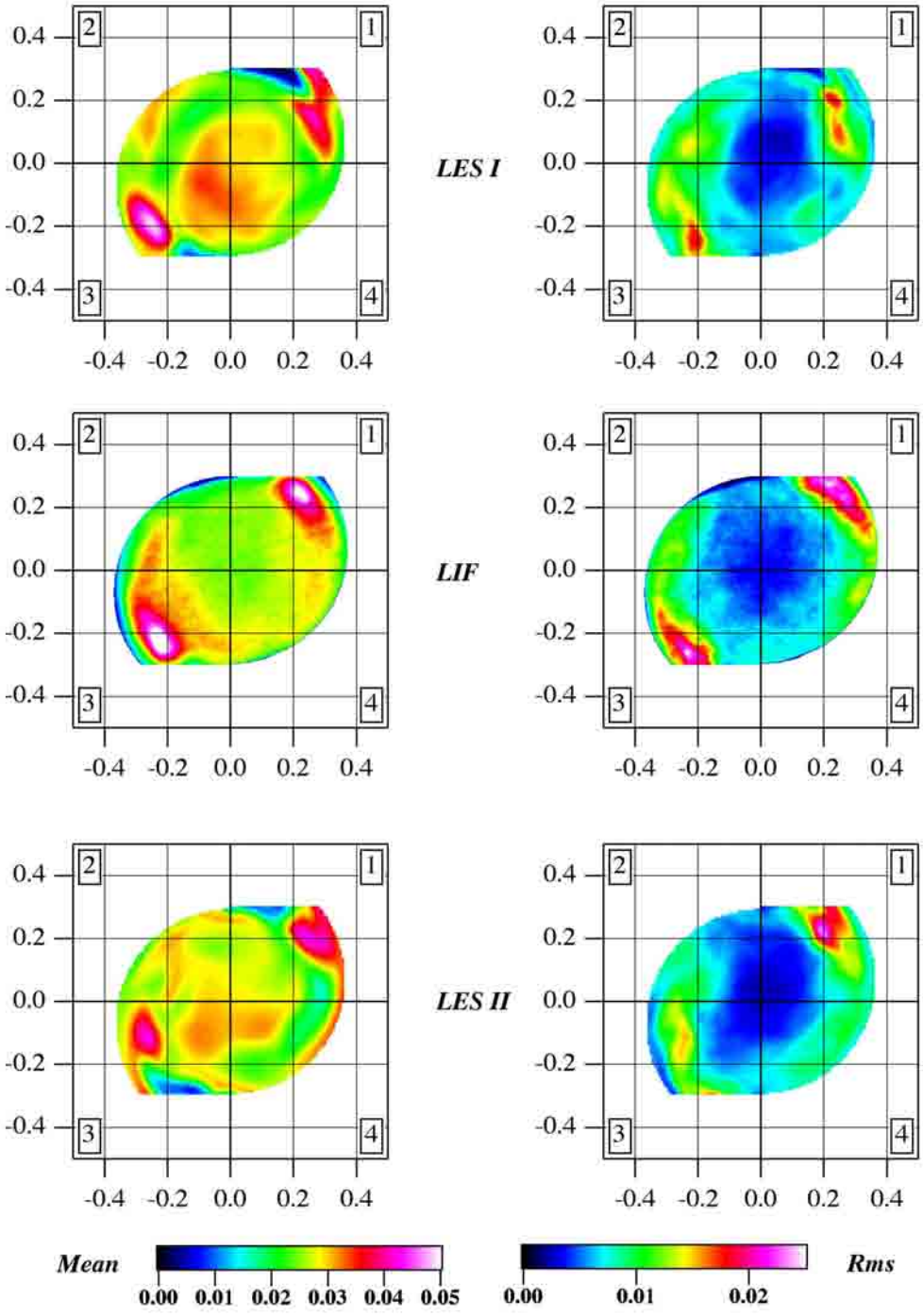


Figure A.3: Comparison of LES and Experiment at $x/D = -0.33$ (Section (7.5)).

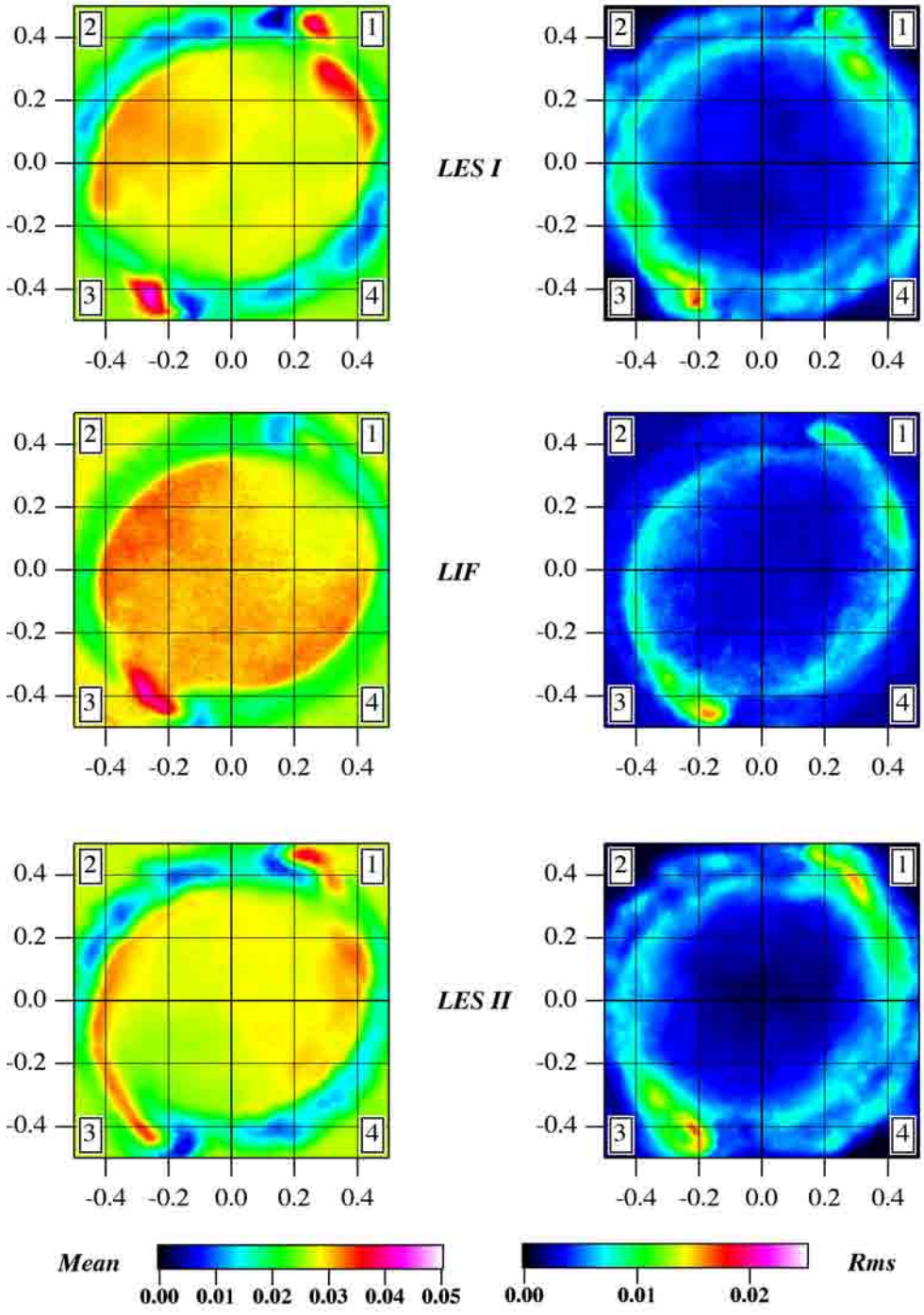


Figure A.4: Comparison of LES and Experiment at $x/D = 0.08$ (Section (7.5)).

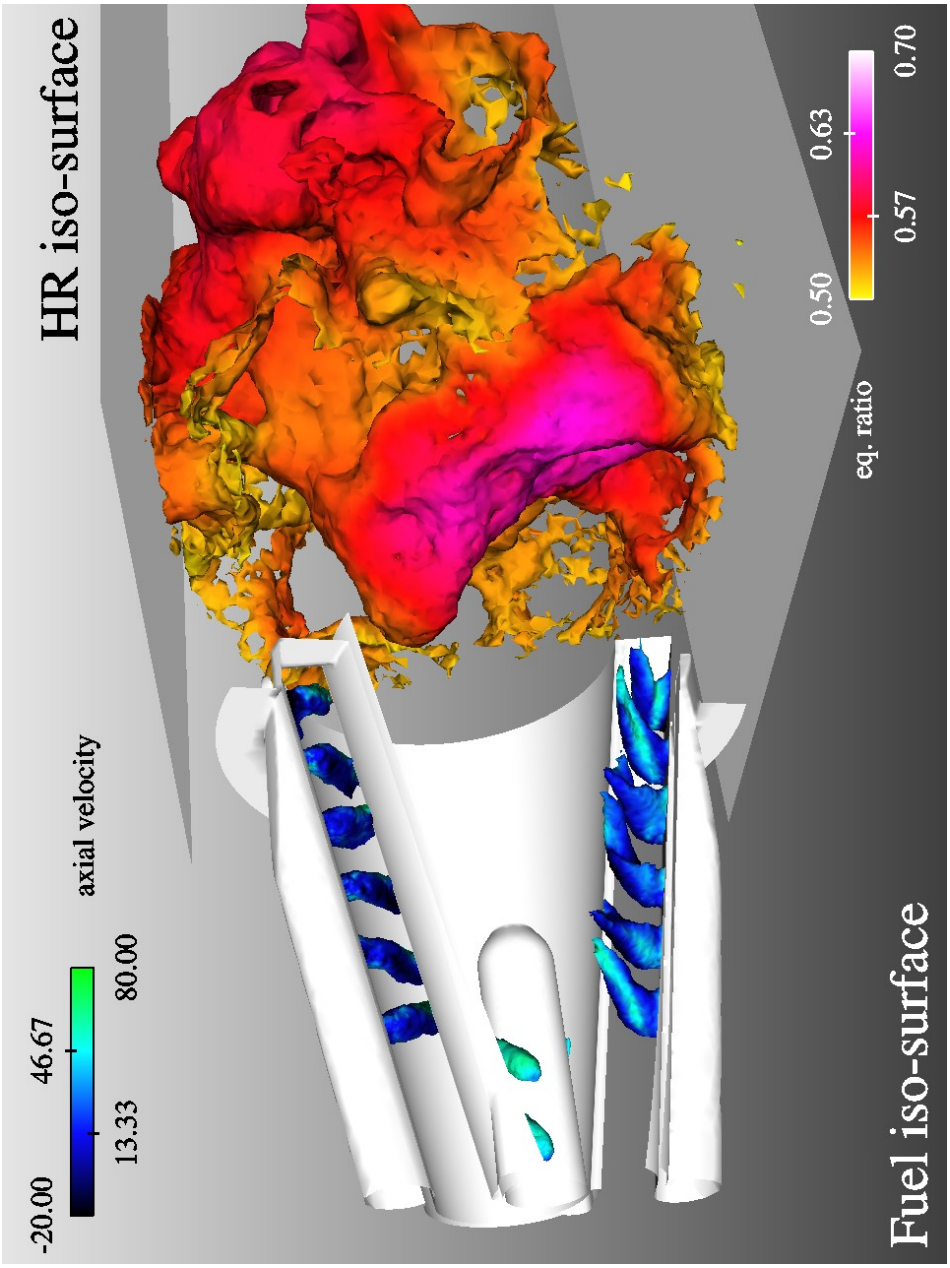


Figure A.5: Snapshot of the RLN simulation (Section (8.2)).

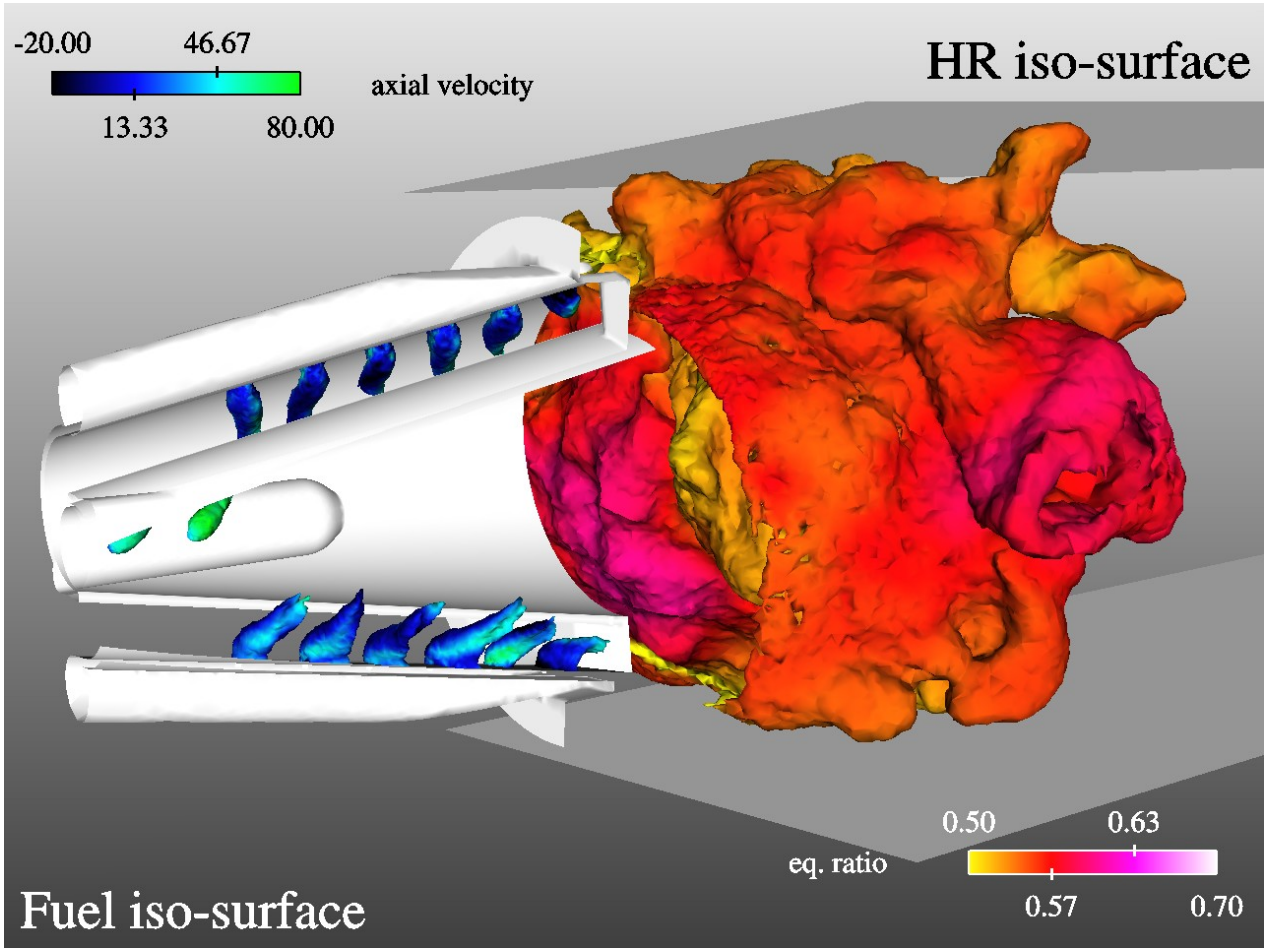


Figure A.6: Snapshot of the RLN AD simulation (Section (8.2)).

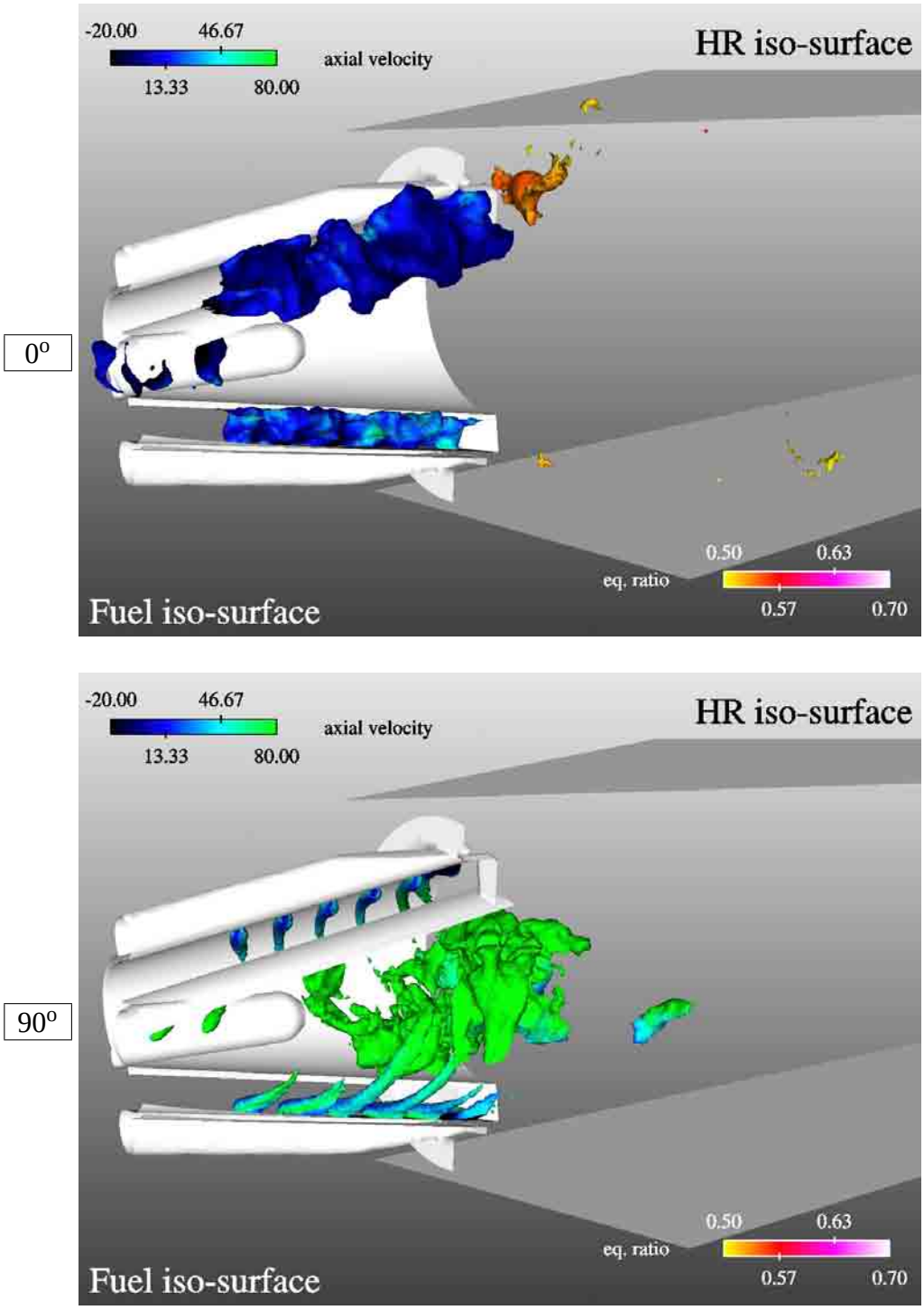


0°

90°

Figure A.7: Snapshot of the RLR 0.96 simulation (Section (8.3)); phase angles 0° and 90°.

180°

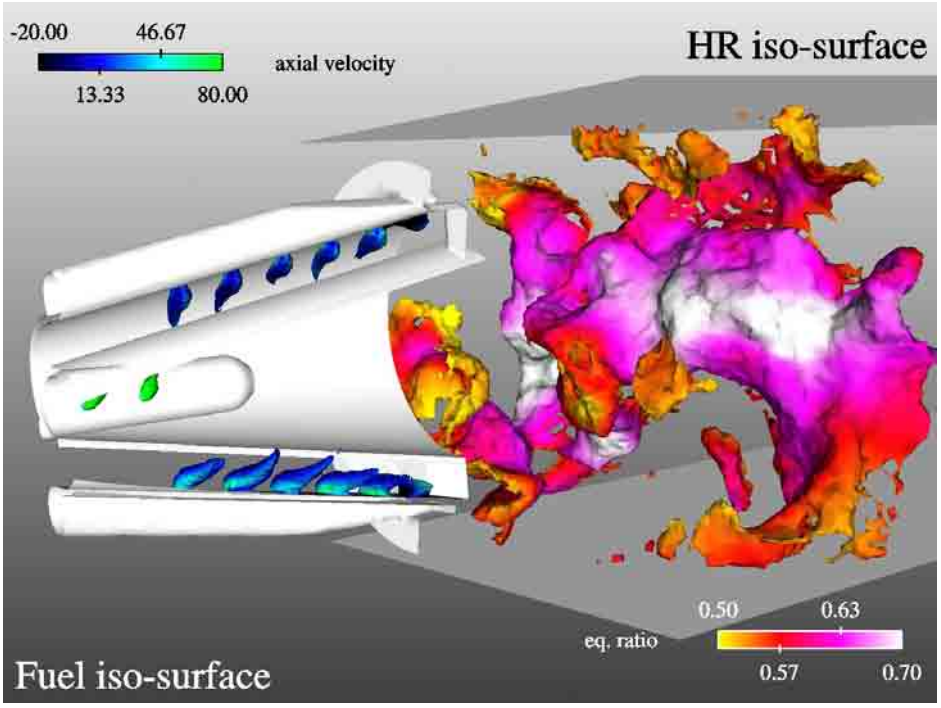


270°

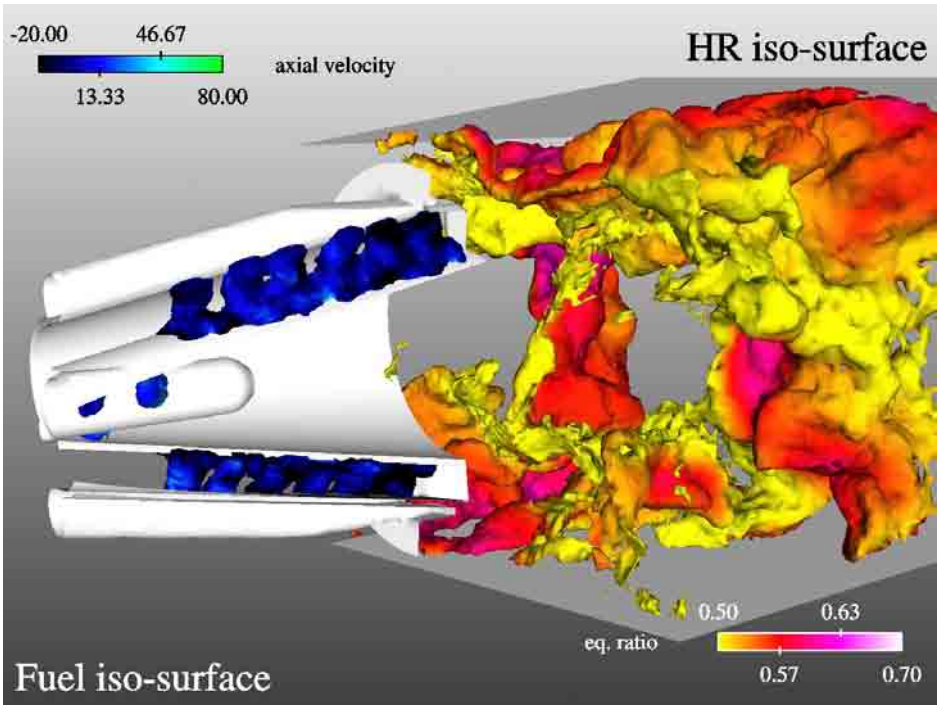


Figure A.8: Snapshot of the RLR 0.96 simulation (Section (8.3)); phase angles 180° and 270°.

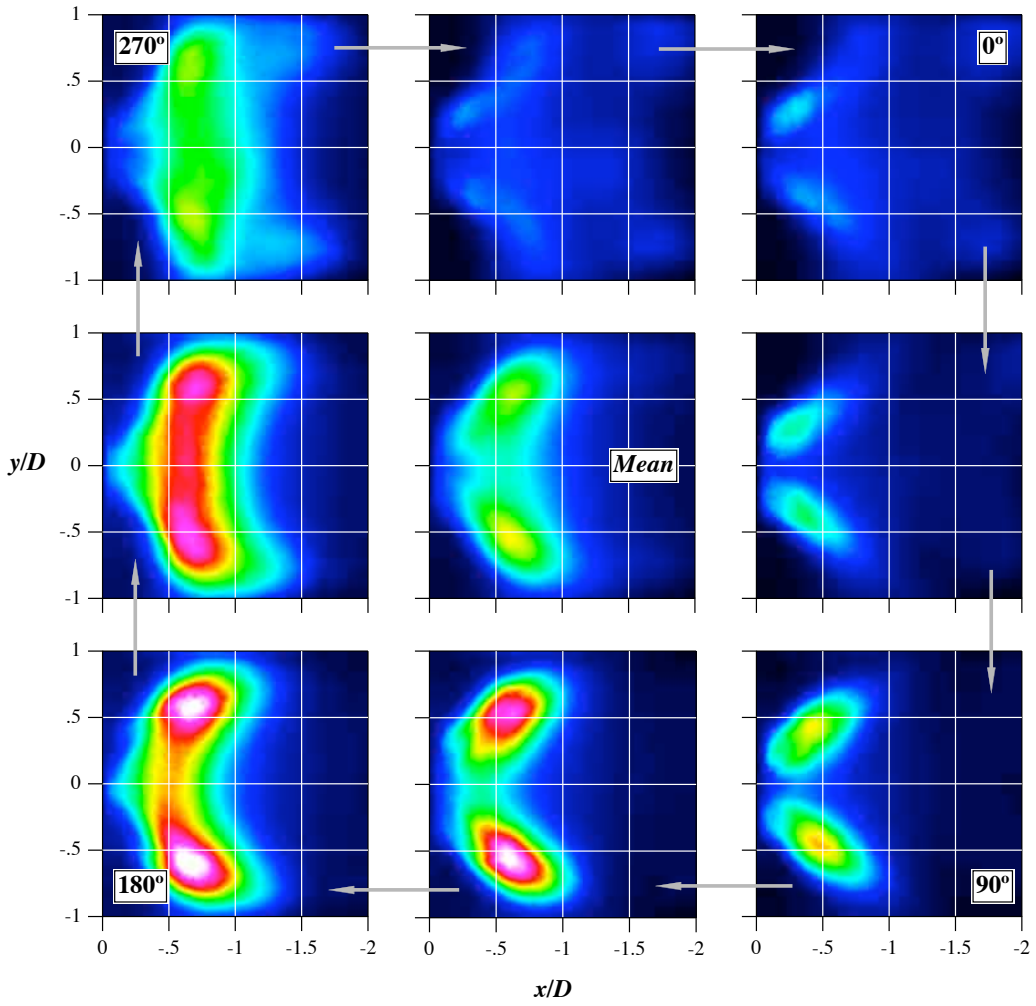


Figure A.9: Integrated views of $OH^*$ from experiment. The total mean is shown in the middle of the Figure, the phase average on the outside (Section (8.1)).

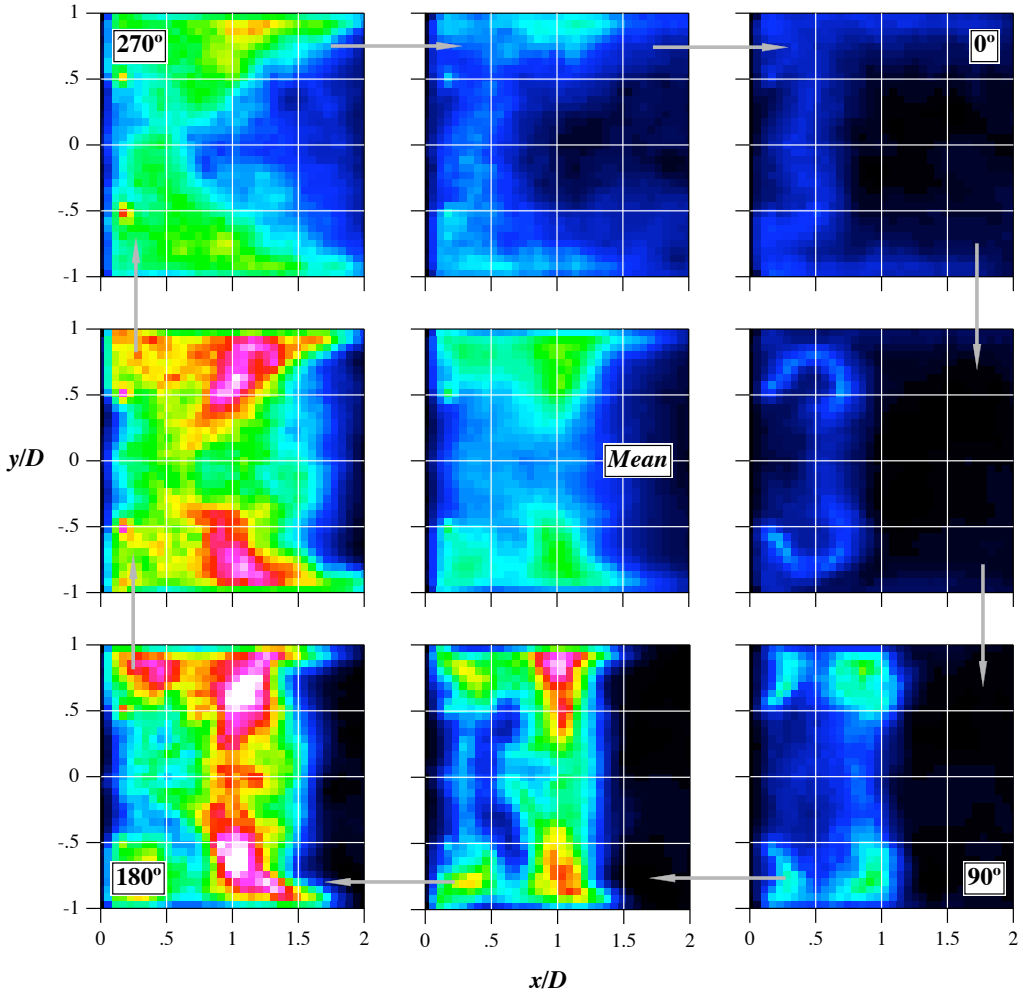


Figure A.10: Integrated views of heat release for the RLR 0.96 case. The total mean is shown in the middle of the Figure, the phase average on the outside (Section (8.3)).

# Appendix B

# Résumé en français

## Introduction

### La combustion des carburants fossiles

Bien que les ressources en carburant fossile ne soient pas infinies, leur épuisement n'est pas encore programmé. Utiliser les ressources de façon efficace et minimiser les dégâts environnementaux constituent les principales préoccupations du moment.
La combustion des hydrocarbures avec l'air conduit à la formation d'eau et de dioxydes de carbone. Ces derniers participant à l'effet de serre, il est indispensable de minimiser leur émission en utilisant des centrales électriques très efficaces. Aujourd'hui, les centrales les plus efficaces utilisant des carburants fossiles ont une efficacité électrique proche de 60%. Il s'agit de turbines à gaz combinées avec des turbines à vapeur (cycle combiné) qui brûlent du gaz naturel. En mettant à profit la chaleur excédentaire (co-génération), le taux d'utilisation du carburant peut atteindre 90% [3].
La production d'autres polluants tels que les oxydes d'azote ($NO_X$) conditionne la conception des turbines à gaz modernes. Ils sont non seulement dangereux pour la flore, mais en outre, ils créent du smog photochimique, et sont les principaux précurseurs de l'ozone qui est un problème majeur pour les villes d'aujourd'hui. Une analyse des mécanismes responsables de la formation des $NO_X$ permet de conclure que la combustion à forte température doit être évitée pour réduire la concentration de $NO_X$. Aujourd'hui, la combustion prémélangée en régime pauvre est la solution la plus populaire. L'objet de ce travail est l'étude d'un brûleur de turbine à gaz industrielle, qui fonctionne dans ce régime. Il s'agit de la plus petite version du brûleur ev [21] ("ev" pour environnemental) du groupe Alstom. En taille standard, il est utilisé dans des turbines à gaz comme le GT26, illustré sur la Figure (B.1). Cette turbine est composée d'un compresseur basse et haute

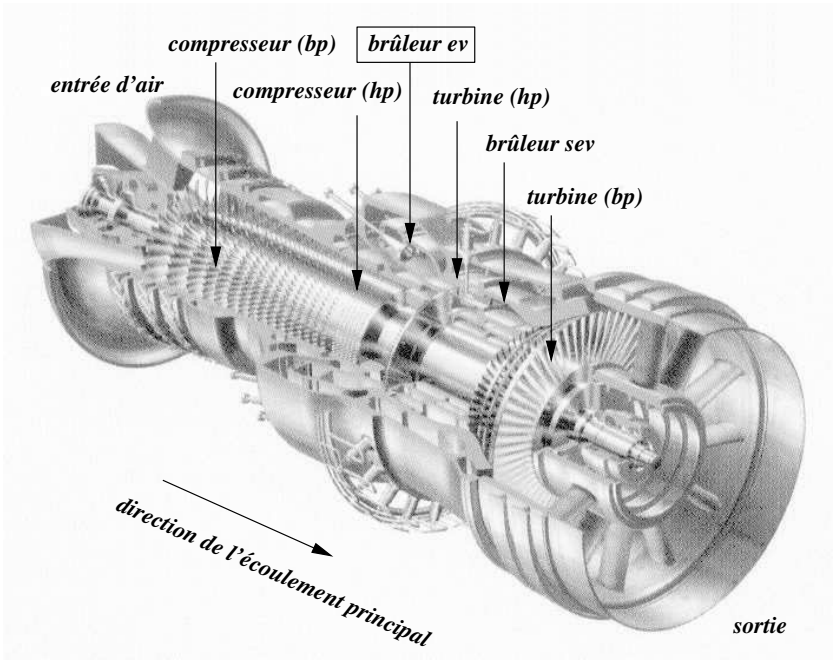


Figure B.1: Illustration schématique du GT26 d'Alstom.

pressions, du brûleur ev et de sa chambre de combustion, d'une turbine à haute pression, d'un brûleur sev ("s" pour séquentiel) et de sa chambre de combustion et enfin de la turbine basse pression.
Dans ce travail, le brûleur est étudié séparément, sans tenir compte du compresseur, de la turbine, de la combustion séquentielle ou même de la chambre de combustion originale. Leur influence est soit négligée, soit prise en compte au travers de conditions limites adaptées.

## La simulation aux grandes échelles

Comprendre tous les processus physiques impliqués dans la combustion turbulente prémélangée en régime pauvre est une tâche ardue. Parallèlement aux expériences qui nécessitent des équipements diagnostiques très sophistiqués, la simulation numérique est de plus en plus utilisée. Ce sont les progrès en terme de puissance de calcul mais aussi le développement de nouveaux modèles de combustion et de turbulence qui sont responsables de cet essor. Tant la structure des écoulements que le processus de combustion dans les brûleurs de turbines à gaz modernes sont de nature instationnaire et demandent donc des simulations résolues en temps. Pour ces applications, la simulation aux grandes échelles

(SGE) dans laquelle les grandes structures de l'écoulement sont résolues et les petites sont modélisées [79], constitue une approche théoriquement saine et accessible avec les ordinateurs d'aujourd'hui.
Le Cerfacs est à la pointe du développement et de l'application de la SGE à des écoulements réactifs dans des géométries complexes. La majeure partie des travaux de recherche menés au Cerfacs s'appuient sur le logiciel AVBP [66], outil de SGE développé en collaboration avec l'IFP. Cette thèse se concentre sur les développements nécessaires à effectuer dans AVBP pour calculer le brûleur ev et analyse les résultats de ces simulations. Elle est menée dans le cadre du projet européen FuelChief qui inclut le groupe Alstom Power, l'Ecole Centrale Paris, les DLR de Stuttgart et Cologne ainsi que le Cerfacs.

## Les facteurs qui influencent la formation des $NO_X$

La complexité de l'ensemble des phénomènes mis en jeu dans le brûleur ev ne permet pas d'étudier tous les aspects de la combustion dans une seule thèse. Par conséquent, ce travail se concentre sur les principaux facteurs qui influencent la formation des $NO_X$. La Figure (B.2) résume l'ensemble des processus impliqués. Les oxydes d'azote sont produits par des réactions chimiques différentes [30, 64, 68] et on peut les grouper en trois catégories : $NO_X$ thermiques, $NO_X$ de carburant et $NO_X$ prompts.

**Les $NO_X$ thermiques** (mécanisme de Zeldovich) sont produits dans les endroits où l'oxygène et de l'azote sont présents simultanément, à condition que les températures soient suffisamment élevées. Ils présentent une dépendance exponentielle en température.

**Les $NO_X$ de type carburant** sont issus de l'azote présent dans les molécules d'hydrocarbure. Dans la mesure où seule la combustion du méthane pur est considérée ici, ce mécanisme n'est pas prépondérant.

**Les $NO_X$ de type prompt** (mécanisme de Fennimore) sont produits dans la flamme par l'intermédiaire des radicaux des hydrocarbures. Il est pratique de grouper ce mécanisme avec celui appelé "oxyde d'azote" puisque tous deux sont actifs à proximité de la flamme et présentent une dépendance exponentielle en richesse.

Pour cette étude, il est donc nécessaire que la cinétique chimique utilisée prédise correctement les $NO_X$ thermiques et prompts. La formation de $NO_X$ dans cette configuration est influencée par la richesse globale, les fluctuations de richesse (à cause de la dépendance exponentielle [27])) et la température de la chambre. En considérant un cas à richesse fixée, on choisit de ne s'intéresser qu'à

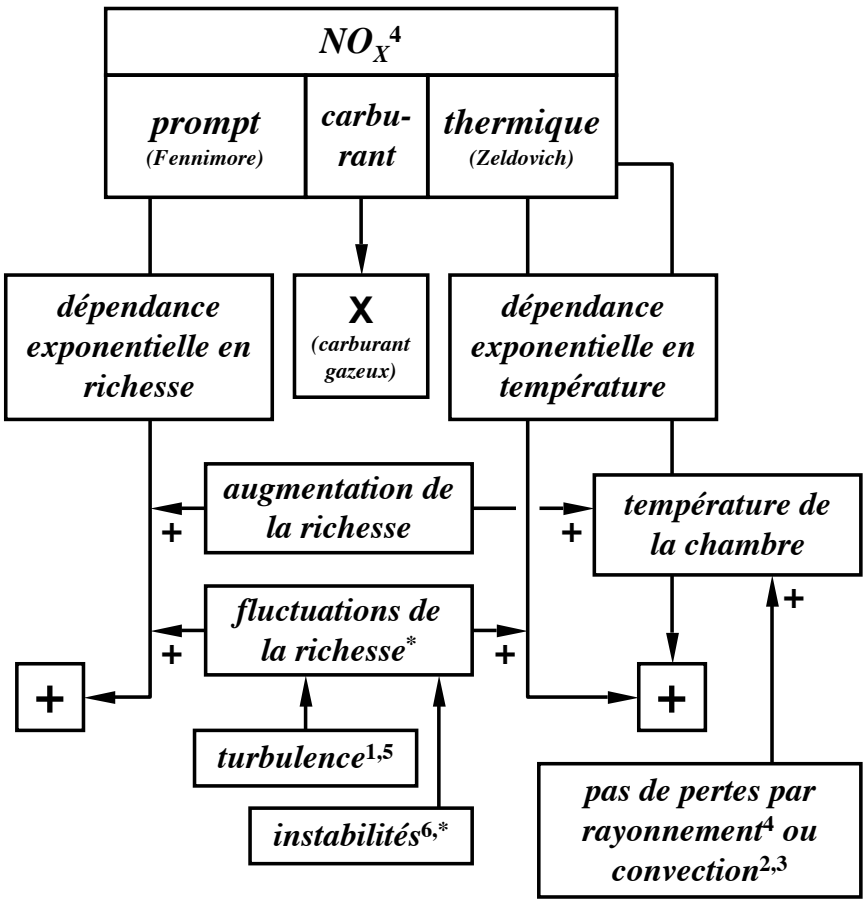


Figure B.2: Mécanismes influençant la production des $NO_X$ dans la combustion prémélangée, pauvre. Les numéros en exposant font référence aux chapitres de cette thèse. Les étoiles en exposant désignent les aspects influencés par l'étagement.

la modélisation thermique et à la simulation du mélange air - carburant. Les processus thermiques importants (flamme exclue) sont le rayonnement et les pertes convectives aux murs. Ils doivent être pris en compte par des modèles adaptés.
Le mélange air - carburant est influencé par plusieurs facteurs. Afin de pouvoir prédire correctement la qualité du mélange en espace et en temps, les injections du carburant et de l'air de refroidissement doivent être résolues directement. La turbulence influence évidemment la formation des $NO_X$ : en changeant le mélange, elle modifie la richesse locale et la température et donc les $NO_X$, comme indiqués dans la Figure (B.2). Il est nécessaire de prédire les grandes échelles de l'écoulement afin de pouvoir prédire les $NO_X$.

Mais la turbulence n'est pas le seul facteur qui influence la production de $NO_X$ à travers le mélange. Des études récentes [88] ont montré que des interactions acoustiques peuvent avoir une influence importante sur le mélange air - carburant. Un mode propre du système peut modifier le mélange à cause des propriétés acoustiques différentes des alimentations d'air et de carburant. Si une telle perturbation produit une variation du dégagement de chaleur après un délai de temps approprié, le mode propre va recevoir de l'énergie acoustique additionnelle. Ce processus ferme la boucle de résonance et mène à une instabilité de combustion [45]. Elle doit être prise en compte parce qu'elle peut augmenter les émissions des $NO_X$ à travers des perturbations importantes de la richesse.
Une des particularités du brûleur de cette étude est son concept d'étagement. Il permet la modification de la distribution du carburant dans le brûleur. L'expérience montre que la distribution du carburant n'a pas seulement une influence sur les émissions de $NO_X$, mais aussi sur les instabilités de combustion. Sa validation est le but du projet FuelChief, mais pas l'objectif de cette thèse. En résumé, on se concentre sur ce qui semble être le point central de la conception de beaucoup de turbines à gaz modernes : trouver un compromis entre les émissions de $NO_X$ et les instabilités de combustion.

## Plan

Cette thèse traite en détail les sujets abordés plus haut et est composée des chapitres suivants :

**Chapitre (1)** introduit à la turbulence et au concept de la SGE. Des aspects comme la modélisation de sous-maille et le post-traitement sont également décrits. De plus, le logiciel AVBP, qui permet la SGE réactive des écoulements compressibles afin de pouvoir prédire le couplage acoustique – combustion, est présenté.

**Chapitres (2) et (3)** traitent de la partie la plus faible de beaucoup des SGE : les murs. D'abord, une introduction à la modélisation des couches limites turbulentes est présentée et une nouvelle loi de paroi, développée dans cette thèse, est décrite. Ensuite, une simulation d'un canal turbulent est présentée et validée avec des données expérimentales et corrélations pour la vitesse et le transfert de chaleur.

**Chapitre (4)** concerne la modélisation des écoulements réactifs et présente un modèle pour la chimie des $NO_X$. Un modèle de rayonnement, basé sur la composition locale du gaz est présenté et son influence sur les émissions des $NO_X$ est montrée.

**Chapitre (5)** présente la combustion turbulente et sa modélisation. L'approche de la flamme épaissie, utilisée pour prendre en compte les interactions flamme – turbulence, est décrite et des exemples de son application en pratique sont donnés.

**Chapitre (6)** traite des aspects acoustiques. En particulier, les conditions limites acoustiques de sortie pour la SGE sont décrites et une description basique des instabilités de combustion est donnée.

**Chapitre (7)** détaille le brûleur ev et son principe d'étagement, qui est capable d'influencer les émissions et les pulsations dûes à la combustion par la modification du mélange air-carburant. Les résultats de plusieurs simulations non - réactives sont présentés. Non seulement les champs de vitesse, mais également les prévisions du mélange sont validées avec des données issues d'expériences.

**Chapitre (8)** montre les résultats de simulations réactives. La comparaison de deux simulations, une sans la modélisation de la thermique, l'autre avec tous les modèles thermiques montre l'influence du refroidissement sur les émissions de $NO_X$. Des simulations avec des coefficients de réflexion différents à la sortie montrent l'impact des instabilités thermo-acoustiques sur les émissions de $NO_X$.

# Conclusion

Ce travail traite plusieurs aspects qui influencent la formation des oxydes d'azote dans les turbines à gaz, comme évoqué sur la Figure (B.2) dans l'introduction. Des modèles appropriés sont développés, implémentés et vérifiés:

**Lois de paroi :** L'approche classique des lois de paroi développée pour une approche RANS donne des bons résultats dans la SGE de l'écoulement dans le canal turbulent. Elles améliorent les capacités prédictives de la SGE avec des couches limites sous - résolues. Ceci est essentiel pour la prévision des flux de chaleur aux parois. Pour des écoulements qui ne sont pas dominés par le comportement dynamique de la couche limite (comme ceux qui sont présentés dans ce travail), cette approche est complètement suffisante.

**Rayonnement :** Le rayonnement est aussi important que le transfert de chaleur convectif et un modèle simple, basé sur l'hypothèse du gaz optiquement mince, est utilisé comme une première étape pour inclure le rayonnement dans la SGE de la combustion dans les turbines à gaz. Ce modèle est basé sur la composition locale du gaz, faisant l'hypothèse de murs à température constante et négligeant la réabsorption. Il est considéré comme adapté à la configuration traitée dans ce travail. Une extension possible serait le calcul d'indices de vue, toujours en négligeant la réabsorption. Aussi, un couplage avec les températures du mur pourrait être utile.

**Cinétique réduite pour le *NO* :** La prévision de la production du $NO$ est atteinte par l'ajustement du taux de réaction du $NO$ au mécanisme complet (le GRI-Mech 3.0). Le $NO$ est bien reproduit avec cette approche dans les flammes laminaires. Si nécessaire, il est aussi possible d'utiliser un autre mécanisme que le GRI-Mech 3.0 comme mécanisme de base.

Les modèles ainsi décrits sont utilisés pour la SGE d'un brûleur partiellement prémélangé en régime pauvre. Plusieurs points sont étudiés :

**Champs de vitesse des simulations non - réactives :** Les comparaisons avec les données expérimentales montrent les fortes capacités de prédiction que possède actuellement la SGE pour les écoulements non - réactifs. On montre aussi qu'il n'est pas nécessaire d'inclure de la turbulence en entrée pour obtenir de bons résultats dans ce type de configuration.

**Mélange :** Le mélange du carburant avec l'air est inclus directement dans cette étude en calculant directement les trous d'injection du $CH_4$. À une certaine distance des injecteurs, de bons résultats sont atteints. Le facteur limitant pour la qualité des résultats en proche – injection est la résolution du maillage, qui devrait être augmenté dans cette région.

**Stabilisation de flamme :** La forme de la flamme déterminée par la SGE réactive est en adéquation avec les données expérimentales, malgré une plus faible compacité. Ceci est peut-être dû à la correspondance non-parfaite du radical $OH^*$ au dégagement de chaleur ou au modèle de combustion qui n'est peut-être pas parfaitement adapté.

**Pertes thermiques :** L'inclusion des pertes thermiques à travers le rayonnement et le refroidissement convectif est essentielle pour diminuer la température de la chambre et pour arrêter la production du $NO$ thermique. Dans le cas présenté, l'inclusion de ces modèles conduit à une division des émissions de $NO$ en sortie de chambre par dix.

**Instabilité de combustion :** En imposant une condition limite de sortie adaptée, une instabilité de combustion, comparable à celle qui est observée dans l'expérience, est reproduite. On montre que le mécanisme qui ferme la boucle résonante passe par les fluctuations de richesse. Pour une simulation instable, les émissions de $NO$ peuvent augmenter jusqu'à 75%.

En résumé, ce travail montre les effets des modèles numériques et de certains paramètres physiques sur le processus de formation de $NO$ dans la combustion des turbines à gaz. Les niveaux d'émissions sont comparables à ceux de la littérature. Ce travail ajoute des capacités prédictives à la SGE qui étaient hors de portée il y a encore quelques années. Ce travail de thèse va promouvoir l'utilisation de la simulation des écoulements instationnaires dans l'industrie.

# Bibliography


[1] R.J. Adrian. Particle-imaging technique for experimental fluid mechanics. *Annual Review of Fluid Mechanics*, 23:261–304, 1991.

[2] C. Angelberger. *Contributions à la modélisation de l'interaction Flamme-Paroi et des flux pariétaux dans les moteurs à allumage commandé*. PhD thesis, INP Toulouse, 1997.

[3] R. Bachmann, H. Nielsen, J. Warner, and R. Kehlhofer. *Combined - Cycle Gas and Steam Turbine Power Plants*. Pennwell Books, 1999.

[4] E. Balaras, Benocci C., and U. Piomelli. Two-layer approximate boundary conditions for large-eddy simulations. *AIAA Journal*, 34:1111–1119, 1996.

[5] R.S. Barlow, A.N. Karpetis, J.H. Frank, and J.-Y. Chen. Scalar profiles and no formation in laminar opposed-flow partially premixed methane/air flames. *Combustion and Flame*, 127:2102–2118, 2001.

[6] J.A. Bellerose and C.B. Rogers. Measuring mixing and local ph through laser-induced fluorescence. In *ASME Fluids Conference*, pages 217–220, 1994.

[7] P. Billant, J.-M. Chomaz, and P. Huerre. Experimental study of vortex breakdown in swirling jets. *Journal of Fluid Mechanics*, 376:183–219, 1998.

[8] J. Boussinesq. Essai sur la théorie des eaux courantes. *Mem. Acad. Sci. Inst. Nat. France*, 1877.

[9] T.D. Butler and P.J. O'Rourke. A numerical method for two-dimensional unsteady reacting flows. In *16th Symp. (Int.) on Combustion*, pages 1503–1515, 1977.

[10] W. Cabot and P. Moin. Approximate wall boundary conditions in the large-eddy simulation of high reynolds number flow. *Flow Turb. Combust*, 63:269–291, 2000.

[11] CERFACS. *The AVBP HandBook*.

[12] M.W. Chase, editor. *NIST-JANAF Thermochemical tables*. American Chemical Society, 1998.

[13] B.T. Chu. On the energy transfer to small disturbances in fluid flow. Part I. *Acta Mechanica*, 1:215–234, 1965.

[14] O. Colin. *Simulation aux Grandes Echelles de la Combustion Turbulente Prémélangée dans les Statoréacteurs*. PhD thesis, INP Toulouse, 2000.

[15] O. Colin, D. Ducros, F. Veynante, and T. Poinsot. A thickened flame model for large eddy simulations of turbulent premixed combustion. *Physics of Fluids*, 12:1843–1863, 2000.

[16] O. Colin and M. Rudgyard. Development of high-order Taylor-Galerkin schemes for unsteady calculations. *Journal of Computational Physics*, 162(2):338–371, 2000.

[17] J. Cousteix. *Turbulence et couche limite*. Cepadues, 1990.

[18] F. Dabireau. *Etudes des transferts de chaleur aux parois dans les moteurs-fusées*. PhD thesis, INP Touslouse, 2002.

[19] J. David. *Modélisation des Transferts radiatifs en combustion par methode aux ordonnées discretes sur des maillages non structurés tridimensionnels*. PhD thesis, INP Toulouse, 2004.

[20] J. Deardorff. A numerical study of three-dimensional turbulent channel flow at large Reynolds numbers. *Journal of Fluid Mechanics*, 41:453–480, 1970.

[21] K. Doebbeling, A. Eroglu, F. Joos, and J. Hellat. Novel technologies for natural gas combustion in turbine systems. In *Eurogas 99*, 1999.

[22] L. Duchamp de Lageneste and H. Pitsch. A level-set approach to large eddy simulation of premixed turbulent combustion. In *CTR Annual Research Briefs*, 2000.

[23] J.M. Duclos, D. Veynante, and T. Poinsot. A comparison of flamelet models for premixed turbulent combustion. *Combustion and Flame*, 95:101–117, 1993.

[24] F. Ducros. *Simulations numériques directes et des grandes échelles de couches limites compressibles*. PhD thesis, INP Grenoble, 1995.

[25] F. Durst, A. Melling, and J.H. Whitelaw. *Principles and practice of laser Doppler anemometry*. Academic Press, London, 1976.

[26] J.H. Ferziger and M. Perić. *Computational Methods for Fluid Dynamics*. Springer Verlag, 2002.

[27] P. Flohr, P. Schmitt, and C.O. Paschereit. Mixing field analysis of a gas turbine burner. In *Proceedings of IMECE'02*, pages 325–333, 2002.

[28] M. Germano, U. Piomelli, P. Moin, and W.H. Cabot. A dynamic subgrid-scale eddy viscosity model. *Phys. Fluids A*, 3(7):1760–1765, 1991.

[29] M. Giles. Non-reflecting boundary conditions for euler equation calculations. *AIAA Journal*, 28(12):2050–2058, 1990.

[30] P. Glarborg, J.A. Miller, and R.J. Kee. Kinetic modeling and sensitivity analysis of nitrogen oxide formation in well-stirred reactors. *Combustion and Flame*, 65:177–202, 1986.

[31] J.P. Gore, J. Lim, T. Takeno, and X.L. Zhu. A study of the effects of thermal radiation on the structure of methane/air counter-flow diffusion flames using detailed chemical kinetics. In *Book of Abstracts of the 5th ASME/JSME Joint Thermal Engeneering Conference*, page 50, 1999.

[32] W.L. Grosshandler. RADCAL: A narrow-band model for radiation calculations in a combustion environment. Technical Report 1402, NIST, 1993.

[33] G. Grötzbach. Direct numerical and larger eddy simulation of turbulent channel flows. In *Encyclopedia of Fluid Mechanics*, pages 1337–1391. West Orange, 1987.

[34] A.K. Gupta, D.G. Lilley, and N. Syred. *Swirl Flows*. Abacus Press, 1984.

[35] J.O. Hinze. *Turbulence*. McGraw-Hill, 1975.

[36] J.O. Hirschfelder, C.F. Curtiss, and R.B. Byrd. *Molecular theory of gases and liquids*. John Wiley & Sons, 1969.

[37] G. Hoffmann and C. Benocci. Approximate wall boundary conditions for large-eddy simulations. In *Advances in Turbulence V*, pages 222–228. Kluwer, 1995.

[38] http://www.me.berkeley.edu/gri-mech. Gri-Mech Website.

[39] F.P. Incropera and D.P DeWitt. *Introduction to Heat Transfer*. John Wiley & Sons, 1996.

[40] A. Jameson, W. Schmidt, and E. Turkel. Numerical solutions of the euler equations by finite volume methods using runge-kutta time-stepping schemes. *AIAA paper*, 81-1259, 1981.

[41] J. Jimenez and P. Moin. The minimal flow unit in near-wall turbulence. *Journal of Fluid Mechanics*, 225:213–240, 1991.

[42] Y. Ju, G. Masuya, and P.D. Ronney. Effects of radiative emission and absorption on the propagation and extinction of premixed gas flames. In *27th Symp. (Int.) on Combustion*, pages 2619–2626, 1998.

[43] W.M. Kays and M.E. Crawford. *Convective heat and mass transfer*. McGraw-Hill, 1980.

[44] R.J. Kee, J.F. Grcar, M.D. Smooke, J.A. Miller, and E. Meeks. Premix: a fortran program for modeling steady laminar one-dimensional premixed flames. Technical report, Sandia National Laboratories, 1998.

[45] J.J. Keller. Thermoacoustic oscillations in combustion chambers of gas turbines. *AIAA Journal*, 33(12):2280–2287, 1995.

[46] J. Kim, P. Moin, and R. Moser. Turbulence statistics in fully developed channel flow at low reynolds number. *Journal of Fluid Mechanics*, 177:133–166, 1987.

[47] L. Landau and E. Lifchitz. *Physique théorique*. éd. librairie du globe, 1989.

[48] B.E. Launder and D.B. Spalding. The numerical computation of turbulent flows. *Computer Methods in Applied Mechanics and Engineering*, 3:269–289, 1974.

[49] A.H. Lefebvre. *Gas Turbine Combustion*. Taylor & Francis, 1998.

[50] J.-P. Légier. *Simulations numériques des instabilités de combustion dans les foyers aéronautiques*. PhD thesis, INP Toulouse, 2001.

[51] A. Leonard. Energy cascade in large eddy simulations of turbulent fluid flows. *Adv. Geophys.*, 18A:237, 1974.

[52] A. Leonard. Direct numerical simlation. In *Turbulence and its Simulation*. Springer Verlag, 1995.

[53] M. Lesieur and O. Metais. New trends in large-eddy simulations of turbulence. *Annual Review of Fluid Mechanics*, 28:45–82, 1996.

[54] D.R. Lide, editor. *CRC Handbook of Chemistry and Physics, 75th edition*. CRC Press, 1994.

[55] D.K. Lilly. A proposed modification of the germano subgrid-scale closure method. *Physics of Fluids A*, 4(3):633–635, 1992.

[56] O. Lucca-Negro and T. O'Doherty. Vortex breakdown: a review. *Progress in Energy and Combustion Science*, 27(4):431–481, 2001.

[57] C. Martin. EPORCK user guide V1.8. Technical Report TR/CFD/04/84, CERFACS, 2004.

[58] C. Martin, L. Benoit, F. Nicoud, and T. Poinsot. Analysis of acoustic energy and modes in a turbulent swirled combustor. In *Proceeding of the Summer Program*, pages 377–394, Center for Turbulence Research, NASA AMES/Stanford University, USA, 2004.

[59] P.J. Mason and N.S. Callen. On the magnitude of the subgrid-scale eddy coefficient in large-eddy simulation of turbulent channel flow. *Journal of Fluid Mechanics*, 162:439–462, 1986.

[60] C. Meneveau and T. Poinsot. Stretching and quenching of flamelets in premixed turbulent combustion. *Combustion and Flame*, 86:311–332, 1991.

[61] S. Menon, P.-K. Yeung, and W.-W. Kim. Effect of subgrid models on the computed interscale energy transfer in isotropic turbulence. *Computers and Fluids*, 25(2):165–180, 1996.

[62] Z. Michalewicz. *Genetic Algorithm + Data structure = Evolution Programs*. Springer Verlag, 1996.

[63] H.P. Miller, R. Mitchell, M. Smooke, and R. Kee. Towards a comprehensive chemical kinetic mechanism for the oxidation of acetylene: comparison of model predictions with results from flame and shock tube experiments. In *19th Symp. (Int.) on Combustion*, pages 181–196, 1982.

[64] J.A. Miller and C.T. Bowman. Mechanism and modeling of nitrogen chemistry in combustion. *Progress in Energy and Combustion Science*, 15:287–338, 1989.

[65] R.J. Monaghan. The behaviour of boundary layers at supersonic speeds. *IAS Preprint 557*, 1955.

[66] V. Moureau, G. Lartigue, Y. Sommerer, C. Angelberger, O. Colin, and T. Poinsot. Numerical methods for unsteady compressible multi-component reacting flows on fixed and moving grids. *Journal of Computational Physics*, 202(2):710–736, 2005.

[67] W.B. Ng, E. Clough, K.J. Syed, and Y. Zhang. The combined investigation of the flame dynamics of an industrial gas turbine combustor using high-speed imaging and an optically integrated data collection method. *Measurement Science and Technology*, 15(11):2303–2309, 2004.

[68] D. Nicol, P.C. Malte, J. Lai, N.N. Marinov, and D.T. Pratt. NOx sensitivities for gas turbine engines operated on lean-premixed combustion and conventional diffusion flames. In *ASME International Gas Turbine and Aeroengine Congress and Exposition*, 1992.

[69] F. Nicoud and F. Ducros. Subgrid-scale stress modelling based on the square of the velocity gradient. *Flow, Turbulence and Combustion*, 62:183–200, 1999.

[70] F. Nicoud and T. Poinsot. Fluctuating energies and stability criteria for thermoacoustic instabilities: is the rayleigh criterion right? *Combustion and Flame*, to appear, 2005.

[71] C. Nottin. *Large Eddy Simulation of combustion instabilities*. PhD thesis, Ecole Centrale Paris, 2000.

[72] W. Nusselt. Das Grundgesetz des Wärmeüberganges. *Gesund. Ing*, 1915.

[73] N. Peters. The turbulent burning velocity for large-scale and small-scale turbulence. *Journal of Fluid Mechanics*, 384:107–132, 1999.

[74] N. Peters. *Turbulent Combustion*. Cambridge University Press, 2000.

[75] A.D. Pierce. *Acoustics: An Introduction to its Physical Principles and Applications*. Acoustical Society of America, 1989.

[76] U. Piomelli and E. Balaras. Wall-layer models for large-eddy simulations. *Annual Review of Fluid Mechanics*, 34:349–374, 2002.

[77] T. Poinsot and S. Lele. Boundary conditions for direct simulations of compressible viscous flows. *Journal of Computational Physics*, 101(1):104–129, 1992.

[78] T. Poinsot, A. Trouvé, D. Veynante, S. Candel, and E. Esposito. Vortex driven acoustically coupled combustion instabilities. *Journal of Fluid Mechanics*, 177:265–292, 1987.

[79] T. Poinsot and D. Veynante. *Theoretical and Numerical Combustion*. R.T. Edwards, 2001.

[80] T. Poinsot, D. Veynante, and S. Candel. Quenching processes and premixed turbulent combustion diagrams. *Journal of Fluid Mechanics*, 228:561–605, 1991.

[81] S.B. Pope. *Turbulent Flow*. Cambridge University Press, 2001.

[82] L. Prandtl. Über Flüssigkeitsbewegung bei sehr kleiner Reibung. *Internat. Math. Kongr. Heidelberg*, 1904.

[83] L. Prandtl. Über die ausgebildete Turbulenz. *ZAMM 5*, 136, 1926.

[84] L. Prandtl and O.G. Tietjens. *Applied Hydro- and Aeromechanics*. Dover, 1934.

[85] L. Rayleigh. The explanation of certain acoustical phenomena. *Nature, July 18*, pages 319–321, 1878.

[86] P. Sagaut. *Large Eddy Simulation for incompressible flows*. Springer Verlag, 2000.

[87] T. Schönfeld and M. Rudgyard. Steady and unsteady flows simulations using the hybrid flow solver AVBP. *AIAA Journal*, 37(11):1378–1385, 1999.

[88] B. Schuermans, V. Bellucci, C. Paschereit, and P. Flohr. Thermoacoustic flame transfer function of a gas turbine burner in premix and pre-premix combustion. In *42nd AIAA Aerospace Sciences Meeting and Exhibit*, 2004.

[89] U. Schumann. Subgrid scale model for finite difference simulations of turbulent flows in plane channels and annuli. *Journal of Computational Physics*, 18:376–404, 1975.

[90] L. Selle, G. Lartigue, T. Poinsot, A. Kaufmann, A. Krebs, and D. Veynante. Large Eddy Simulation of turbulent combustion for gas turbines with reduced chemistry. In *Proceedings of the Summer program*, pages 333–344, Center for Turbulence Research, NASA AMES/Stanford University, USA, 2002.

[91] L. Selle, F. Nicoud, and T. Poinsot. The actual impedance of non-reflecting boundary conditions: implications for the computation of resonators. *AIAA Journal*, 42(5):958–964, 2004.

[92] J. Smagorinsky, S. Manabe, and S. Holloway. General circulation experiments with the primitive equations. *Mon. Weather Rev*, 91(3):99–164, 1963.

[93] A. Smirnov, S. Shi, and I. Celik. Random flow simulations with a bubble dynamics model. In *ASME Fluids Engineering Division Summer Meeting*, 2000.

[94] P.R. Spalart, W.H. Jou, M. Strelets, and S.R. Allmaras. Comments on the feasibility of LES for wings and on a hybrid RANS/LES approach. In *Advances in DNS/LES*, pages 137–148. Greyden, 1997.

[95] W. Sutherland. The viscosity of gases and molecular force. *Phil. Mag.*, 5(36):507–531, 1893.

[96] J. Taine and J.-P. Petit. *Transferts thermiques*. Dunod, 1995.

[97] H. Tennekes and J.L. Lumley. *A First Course in Turbulence*. MIT Press, 1972.

[98] K.W. Thompson. Time dependent boudary conditions for hyperbolic systems. *Journal of Computational Physics*, 68:1–24, 1987.

[99] E.R. Van Driest. On turbulent flow near a wall. *J. Aero. Sci.*, 23:1007–1011, 1956.

[100] Th. Von Kármán. Mechanische Aehnlichkeit und Turbulenz. *Nach. Ges. Wiss. Göttingen, Math.Phys. Klasse*, 58, 1930.

[101] B. Vreman. *Direct and large-eddy simulation of the compressible turbulent mixing layer*. PhD thesis, Univerity of Twente, 1995.

[102] M. Wang and P. Moin. Computation of trailing-edge flow and noise using large-eddy simulation. *AIAA Journal*, 38:2201–2209, 2000.

[103] T. Wei and W.W. Willmarth. Reynolds-number effects on the structure of a turbulent channel flow. *Journal of Fluid Mechanics*, 204:57–95, 1989.

[104] H. Werner and H. Wengle. Large-eddy simulation of a turbulent flow around a cube in a plane channel. In *Selected Papers from the 8th Symposium on Turbulent Shear Flows*, pages 155–168. Springer Verlag, 1993.

[105] R.V. Wheeler. *J. Chem. Soc.*, 113:840, 1918.

[106] F.A. Williams. *Combustion Theory*. Benjamin Cummings, 1985.

[107] X. Wu and K.D. Squires. Prediction of the three-dimensional turbulent boundary layer over a swept bump. *AIAA Journal*, 36:505–514, 1998.

[108] A. Yoshizawa and K. Horiuti. A statistically-derived subgrid-scale kinetic energy model for the large-eddy simulation of turbulent flows. *Physical Society of Japan*, 54:2834–2839, 1985.

# Index